

Interaction of Pulsar Wind with Stellar Wind
Observed in the PSR B1259–63 /SS 2883 System

Masaharu Hirayama

Doctoral Thesis
submitted to
Faculty of Science
University of Tokyo

December 1995

Abstract

The binary system consisting of a radio pulsar PSR B1259–63 and a Be star SS 2883 has been observed with the *ASCA* satellite at six epochs, from the most recent periastron passage in January 1994 to the recent apastron approach in 1995. In this unique system, shock acceleration of the relativistic pulsar wind is expected to result in high-energy emission. Since the distance between the pulsar and the Be star varies by over one order of magnitude during its orbital period ~ 3.4 year, the high-energy emission from the system provides a unique chance to study the emission mechanism under predictably varying conditions imposed by the Keplerian orbit. In this thesis for the first time we challenge this exciting possibility and sort out contributions of properties of stellar winds.

The system is unambiguously detected in the X-ray band ranging from 1 keV to 10 keV at all six epochs, with moderate X-ray luminosity $L_X \sim (0.1\text{--}1) \times 10^{34}$ erg s $^{-1}$ and little absorption. We detect no X-ray pulsations at any of six observed epochs. The observed X-ray spectra are generally consistent with a single power law model but the luminosities in the band between 1 and 10 keV differ in all six observations. At periastron the spectrum shows some softening and the intensity drops to about a half of those observed two weeks before and after the periastron. The column density determined from absorption is $N_H \sim 6 \times 10^{21}$ cm $^{-2}$ for all six observations, consistent with that expected from the galactic contribution alone.

Based on the observations we examine contributions of possible mechanisms for X-ray emission in the system, namely, coronal emission from the Be star, rotation-powered emission from the pulsar, emission from accretion onto the neutron star surface, emission from accreted materials intercepted by the pulsar's magnetosphere, and emission from a shock front formed at the location where the ram pressures of the Be stellar wind and the pulsar wind balance. Among them, synchrotron X-rays emitted from relativistic electron/positron pairs accelerated non-thermally in the shock region accounts naturally for the observations. Within the framework of this model, we show that inverse Compton cooling by UV photons from the Be star is important at periastron, and the shock acceleration must create e^\pm pairs with energy index $s \sim 2$ up to the Lorentz factor $\gamma \sim 10^7$ within ~ 100 s or a shorter time just behind the shock front. In addition, we find evidence for a large inclination of the pulsar's orbit with respect to the equatorial plane of the Be star. From energetics in the shock-powered emission model, we find that the pulsar wind carries more than 4×10^{35} erg s $^{-1}$, a half of the spin-down luminosity of the pulsar. We also find, from the amount of the decrease in X-ray flux at the apastron approach, the momentum flux of the stellar wind lies between 0.05 and 0.28 in units of $(10^{-8} \text{ M}_\odot \text{ yr}^{-1})(1000 \text{ km s}^{-1})$ at apastron.

Contents

1	Introduction	1
1.1	Interacting Pulsar Wind	1
1.2	PSR B1259–63/SS 2883 System	4
1.3	Past Observations of the System	7
2	Instrumentation	9
2.1	ASCA Satellite	9
2.2	XRT	9
2.2.1	Wolter Type I Mirror	11
2.2.2	Design and Performance	11
2.3	SIS	15
2.3.1	System Description	15
2.3.2	Principle of X-ray Detection	17
2.3.3	On-Board Data Processing	19
2.3.4	Fundamental Reduction of SIS data	21
2.4	GIS	28
2.4.1	System Description	28
2.4.2	Principle of X-ray Detection	30
2.4.3	On-Board Data Processing	32
2.4.4	Fundamental Reduction of GIS data	34
2.5	Alignment of the Detectors	43
2.6	Data Transfer	43
2.7	Satellite Operation	45
3	Observation	47
3.1	ASCA Observations of the System	47
3.2	Satellite’s Attitude during Observations	49

4	Analysis and Results	53
4.1	Data Reduction	53
4.2	X-ray Image	56
4.3	Spectral Analysis	58
4.3.1	X-rays from Galactic Plane as Background	60
4.3.2	Spectral Model	63
4.3.3	Systematic Errors in Spectral Analysis	66
4.4	Temporal Analysis	69
4.4.1	X-ray Light Curve	71
4.4.2	Search for X-ray Pulsations	71
4.4.3	Upper Limit on X-ray Pulsation	77
5	Discussion	81
5.1	Summary of ASCA results	81
5.2	Mechanism of X-ray Emission	84
5.2.1	Coronal Emission from the Be Star	85
5.2.2	Emission from the Pulsar as a Spin-Powered Pulsar	85
5.2.3	Emission from Accretion onto the Neutron Star Surface	86
5.2.4	Emission from Accreted Materials Intercepted by Pulsar's Magne- tosphere	87
5.2.5	Shock Emission	88
5.3	Shock-Powered Emission Model	89
5.4	Emission from the Shocked Pulsar Wind	91
5.4.1	Thermal Bremsstrahlung	92
5.4.2	Inverse Comptonization of UV Photons from the Be Star	93
5.4.3	Synchrotron Emission	95
5.5	Interpretation of Observed Features	96
5.5.1	Spectral Softening at Periastron	96
5.5.2	Variability in Observed Luminosity	99
5.6	Constraint on the System Parameters	101
5.6.1	Structure of the Stellar Wind	101
5.6.2	Kinetic Energy of the Pulsar Wind	103
5.6.3	Momentum Flux of the Stellar Wind	105
5.7	Future Studies of the System	106
5.7.1	Shock Acceleration Mechanism	106
5.7.2	Possibility of the Detection of Annihilation Line Emission	107

5.7.3	Observations at Other Wavelengths	107
6	Conclusion	111
	References	113
	Acknowledgment	117

List of Figures

1.1	Pulsar's magnetosphere	2
1.2	Pulsar wind in the PSR B1957+20	3
1.3	Geometry of the Crab pulsar	4
1.4	Binary orbit of the PSR B1259–63/SS 2883 system	6
2.1	Schematic drawing of the <i>ASCA</i> satellite	10
2.2	Arrangement of instruments on the <i>ASCA</i> satellite	10
2.3	The Wolter type I mirror	11
2.4	Effective area of <i>ASCA</i> XRT compared with <i>ROSAT</i> and <i>Einstein</i>	13
2.5	Effective areas of <i>ASCA</i> XRT for various off-axis angles	13
2.6	Point Spread Function of <i>ASCA</i> XRT	14
2.7	Alignment of four CCD chips in SIS	15
2.8	Cross sectional view of SIS	17
2.9	Detection efficiency and energy resolution of SIS.	18
2.10	Definitions of grades of events	22
2.11	Echo phenomenon	24
2.12	Distribution of pixel levels of corner pixels	25
2.13	Structure of GIS	29
2.14	Cross sectional view of GIS housing	31
2.15	Detection efficiency and energy resolution of GIS	32
2.16	Time sequence of an X-ray detection by GIS	35
2.17	Relationship between T_{delay} and T_{arr} for $N_{FIFO} = 0$	36
2.18	Temperature dependence of gain number of GIS	37
2.19	Positional dependence of the gain number of GIS	38
2.20	Secular trend of gain number of GIS	39
2.21	Types of GIS background events	39
2.22	Background rejection with rise time discrimination	41
2.23	Background rejection with spread discrimination	42
2.24	Alignment of the detectors	44

2.25	Structure of a telemetry format	45
3.1	Fields of view of SIS0 and GIS2 at six observations	50
3.2	Actual attitudes of the satellite during six observations by <i>ASCA</i>	51
4.1	DFE values for the six observations	55
4.2	<i>ASCA</i> images of the PSR B1259–63/SS 2883 system for obs2	57
4.3	Determination of X-ray positions on detectors	58
4.4	SRC and BGD regions for SIS0 and GIS2	59
4.5	Comparison of source spectra with background spectra	61
4.6	The contribution of X-ray emission from the galactic plane	62
4.7	Comparison of blank sky spectra in different accumulation regions	62
4.8	Ratios of averaged effective areas of SIS0 and GIS2 for obs2	64
4.9	Comparison of differently estimated background spectra for obs2	64
4.10	Spectral fits to SIS and GIS spectra for obs2	65
4.11	X-ray spectra obtained with the <i>ASCA</i> satellite	67
4.12	X-ray luminosities of the PSR B1259–63/SS 2883 system	69
4.13	Confidence contours for a single power law model	69
4.14	Comparison of spectral parameters by three different backgrounds	70
4.15	X-ray light curves of the PSR B1259–63/SS 2883 system	72
4.16	Periodgrams for six observed epochs	74
4.17	Z_n^2 values versus trial periods for $n = 1$	75
4.18	Z_n^2 values versus trial periods for $n = 2, 3, 4$	76
4.19	Folded light curve at the expected pulse period	77
5.1	Variation of photon indices of the PSR B1259–63/SS 2883 system	82
5.2	Variation of X-ray luminosity of the PSR B1259–63/SS 2883 system	83
5.3	Shock in the PSR B1259–63/SS 2883 system	90
5.4	Kinetic energy input into the shock region	91
5.5	Cooling timescales and emitted photon energy	97
5.6	e^\pm pairs' energy distribution behind the shock	98
5.7	Viewing angle of the shock region from the pulsar	101
5.8	Constraint on the stellar wind parameters	103
5.9	Wide band spectrum of the PSR B1259–63/SS 2883 system	108
5.10	Wide band spectrum of the Crab pulsar and the Crab nebula	108

List of Tables

1.1	Parameters of the PSR B1259–63 determined by Manchester et al. (1995)	5
2.1	Design parameters and performance of <i>ASCA</i> XRT	12
2.2	Design parameters and performance of <i>ASCA</i> SIS	16
2.3	Summary of observation modes in SIS	20
2.4	Summary of grades of SIS.	21
2.5	Charge Transfer Inefficiency measured in August 1994 ^{a)}	27
2.6	Design parameters and performance of GIS	28
2.7	Clock speed relating to time assignment of GIS	33
2.8	Summary of bit assignment of GIS PH mode	34
2.9	Lengths of components of a super frame in a unit of time	43
3.1	Geometry of the PSR B1259–63/SS 2883 system near <i>ASCA</i> observations	47
3.2	Bit assignment of GIS for each observation	48
4.1	Selection criteria for SIS and GIS data	54
4.2	Echo fractions	54
4.3	Net exposures and counting rates of <i>ASCA</i> observations	56
4.4	Observed X-ray positions of the PSR B1259–63/SS 2883 system	58
4.5	Ratios of areas of the SRC and the BGD regions	63
4.6	Best-fit parameters by individual fit to SIS and GIS spectra ^{a)}	66
4.7	Model parameters for <i>ASCA</i> observations of the PSR B1259–63/SS 2883 system obtained by fitting SIS and GIS spectra simultaneously	68
4.8	Comparison of 1–10 keV SIS fluxes ^{a)}	70
4.9	Expected pulse period and parameters for the pulsation search	73
4.10	Apparent pulse periods and parameters for pulsation search in P - \dot{P} space .	77
4.11	Upper limits on X-ray pulsation ^{a)}	79
5.1	Upper limits on pulsed X-ray luminosity	82

Chapter 1

Introduction

1.1 Interacting Pulsar Wind

A spin-powered pulsar is known to be a rapidly rotating neutron star with a strong magnetic field. As a result of the rapid rotation of the strong magnetic field, it is known that the pulsar blows off a plasma of ultrarelativistic charged particles, called a pulsar wind. The charged particles, electron/positron pairs and heavy ions, are accelerated by extremely strong electric field, up to $\sim 10^{15}$ V in the case of the Crab pulsar, induced by the rapid rotation, and flows along the magnetic field lines (see Figure 1.1). Some of the magnetic field lines cannot co-rotate with the neutron star and extend outside the light cylinder, where the co-rotation velocity is equal to the speed of light. Charged particles accelerated along such field lines flow out from the pulsar's magnetosphere and form the pulsar wind.

The pulsar wind may interact with materials around the pulsar. The interaction is characterized by the formation of a shock at the distance where the pulsar wind pressure balances that of the surroundings (see Figure 1.2). At the shock front particles in the pulsar wind and the surroundings may be thermalized and accelerated. The accelerated electrons/positrons then release their kinetic energy as high-energy X-rays/ γ -rays through radiative processes such as synchrotron emission and inverse Compton emission. As a whole, in the system including the rapidly rotating pulsar, its rotational energy is carried by the pulsar wind and converted into high-energy X-rays/ γ -rays by the materials surrounding the pulsar. From this point of view, the surroundings of the pulsar act as a “calorimeter” for the pulsar wind, which carries information on the pulsar activity.

Characteristics of the pulsar wind are poorly understood, although over 500 spin-powered pulsars have ever been discovered. This is mainly because observational studies of the pulsar wind have been possible only in a few cases, such as the Crab pulsar (e.g.

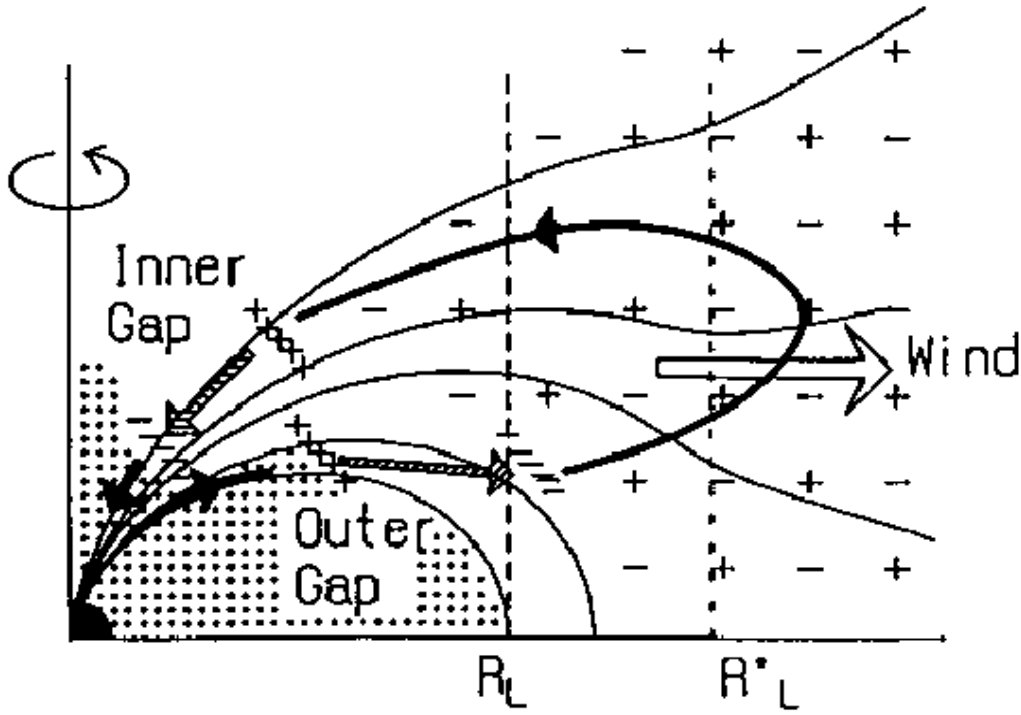


Figure 1.1: Schematic drawing of pulsar's magnetosphere (Shibata 1991).

Arons and Tavani 1994; Gallant and Arons 1994) and a milli-second pulsar PSR B1957+20 (e.g. Arons and Tavani 1993; Arons and Tavani 1994). In the case of the Crab pulsar the pulsar wind has been studied by observations of the Crab nebula, which converts over 90 % of the rotational energy loss rate (so called “spin-down luminosity”) into radiation. From the nebular spectrum and morphology, the Crab pulsar wind is likely composed of electrons, positrons and ions, with the ratio of Poynting flux to particle kinetic energy flux $\sigma \approx 0.005$, and with an estimated Lorentz factor $\gamma \approx 10^6$ (Gallant and Arons 1994; Hoshino et al. 1992; Kennel and Coroniti 1984a; Kennel and Coroniti 1984b). Clearly, there is no assurance that different, and in particular, more common older, pulsars have similar winds, or that there is no radial dependence of wind properties. In the case of the PSR B1957+20, the pulsar bow shock, in which the pulsar wind is interacting with the surrounding interstellar medium (ISM), is seen as H_α nebulae. Although the bow shock also gives clues to the nature of the pulsar wind (e.g. Bell et al. 1993; Cordes et al. 1993; Kulkarni and Hester 1988), detailed study of the pulsar wind is difficult.

In any cases studied so far, parameters of the system, such as the distance to the shock from the pulsar and timescales of radiative coolings, stay constant during history of the astronomical observations. On the other hand, the parameters of the pulsar wind, such as its total kinetic energy and the Lorentz factor, are different between different pulsars. Because of these constraints on “experimental condition”, there has been no way to inves-

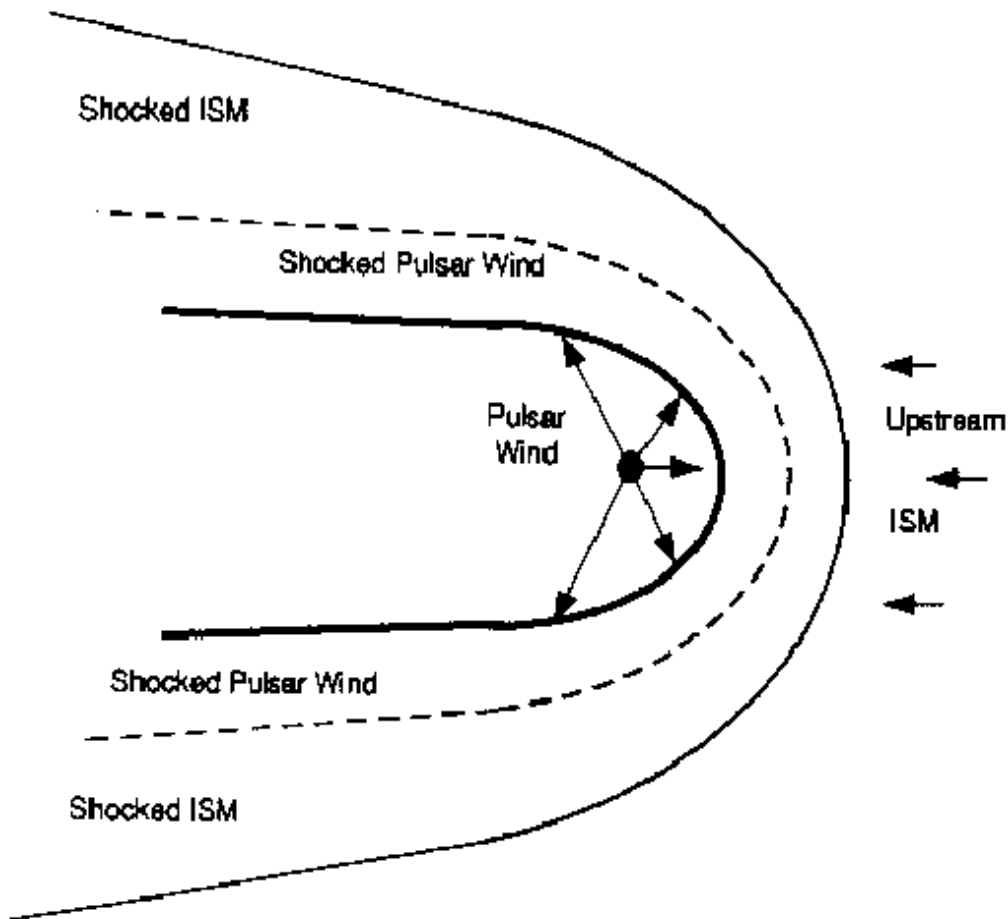


Figure 1.2: Schematic drawing of the pulsar wind interacting with the interstellar medium (“ISM” in the figure) in the case of the PSR B1957+20 (Arons and Tavani 1994).

investigate underlying physics in the system, such as the shock acceleration mechanisms and the role of radiative cooling processes, under well-known predictable (or “well-controlled”) conditions and it has been difficult to sort out the role of such physical processes from individuality of the pulsars.

Here we introduce a binary system PSR B1259–63/SS 2883. The characteristics of the system are ideal to study the interaction of the pulsar wind. In the system a strong stellar wind from the Be star SS 2883 acts as the calorimeter for the pulsar wind from the pulsar PSR B1259–63. Above all, as described in §1.2, the highly eccentric binary orbit of the system plays an important role in investigating the interaction between the pulsar wind and the stellar wind. In the Crab nebula the interaction is static, since neither the pulsar wind nor the surroundings change over astronomers’ lifetimes. In the case of the PSR B1259–63/SS 2883 system, because of the wide and highly eccentric orbit, the nature of the pulsar’s surroundings varies tremendously with its orbital phase during the ~ 3.4 year of its orbital period; for example, the distance between the pulsar and the Be

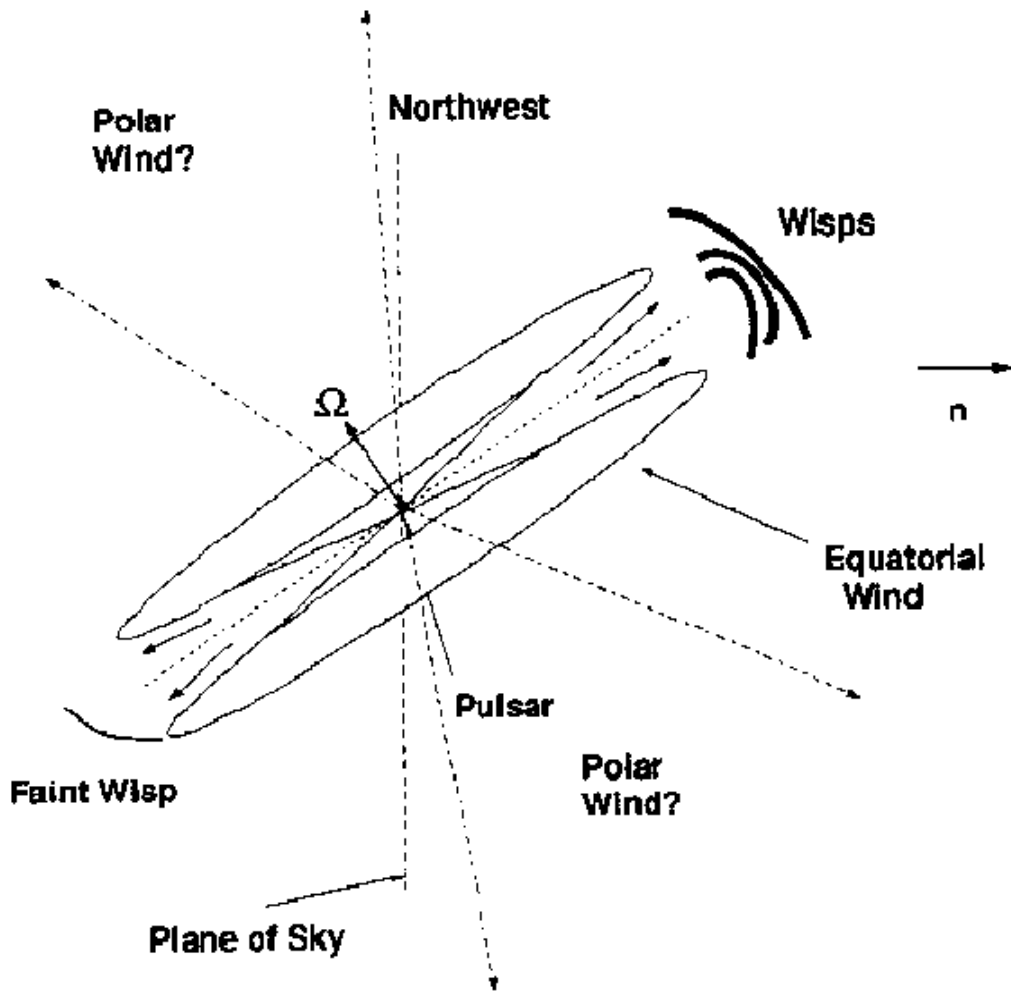


Figure 1.3: Schematic drawing of geometry of the Crab pulsar (Arons and Tavani 1994).

star at apastron is about fifteen times larger than that at periastron. In other words, the highly eccentric orbit provides an opportunity to study the pulsar wind and the shock acceleration mechanism under simply-predictable time-variable experimental conditions provided by the Keplerian orbit.

1.2 PSR B1259–63/SS 2883 System

The PSR B1259–63/SS 2883 system is a binary system consisting of a radio pulsar PSR B1259–63 and a Be star SS 2883. The PSR B1259–63 is a 47 ms radio pulsar, discovered by Johnston et al. (1992b) in a survey of the southern galactic plane for radio pulsars (Johnston et al. 1992a). The pulsar's parameters in Table 1.1 were determined by Manchester et al. (1995) using radio timing observations covering two recent periastron passages in 1990 and in 1994. The radio timing observations have also shown that the

pulsar is in a 3.4 yr, highly eccentric binary orbit with eccentricity $e = 0.86$. The observed Keplerian orbital parameters are also provided in Table 1.1 and a schematic drawing of the binary orbit is shown in Figure 1.4. As mentioned later in §1.3, the companion star was identified to a Be star SS 2883 from optical observations (Johnston et al. 1992b). The mass and radius of SS 2883 are estimated to be $\sim 10 M_{\odot}$ and $\sim 6 R_{\odot}$, respectively.

Table 1.1: Parameters of the PSR B1259–63 determined by Manchester et al. (1995)

Parameters of the PSR B1259–63	
Right Ascension, α (J2000)	$13^{\text{s}} 02^{\text{m}} 47^{\text{s}} .68$
Declination, δ (J2000)	$-63^{\circ} 50' 08'' .6$
Period, P	$47.762053542(8) \text{ ms}$
Spin-down Rate, \dot{P}	$2.27579(16) \times 10^{-15}$
Period Epoch	MJD 48053.440
Dispersion Measure, DM	$146.72(3) \text{ pc cm}^{-3}$
Spin-down Age, τ	$3 \times 10^5 \text{ yr}$
Magnetic Field, B	$3 \times 10^{11} \text{ G}$
Spin-down Luminosity, \dot{E}	$8 \times 10^{35} \text{ erg s}^{-1}$
Orbital Parameters	
Orbital Period, P_b	$1236.72359(5) \text{ days}$
Projected semi-major axis, $asini$	$1296.580(2) \text{ lt-s}$
Longitude of periastron, w	$138^{\circ} .6782(2)$
Eccentricity, e	$0.869931(1)$
Periastron Epoch, T_0	MJD 48124.3448(1)
$\Delta P/P$ at MJD 48124.3	$(+2.6 \pm 0.3) \times 10^{-9}$
$\Delta P/P$ at MJD 49361.2	$(+1.1 \pm 0.3) \times 10^{-9}$

Of nearly 700 known radio pulsars, this is the only Be star–pulsar binary system. The PSR J0045–7319 system in the Small Magellanic Cloud consists of a 926 ms pulsar also in a highly eccentric orbit with a B star. However, optical observations show neither evidence for the emission lines characteristic of Be stars, nor any form of eclipse of the radio signal near periastron (Kaspi et al. 1995a; Kaspi et al. 1994). In the Galaxy many Be/neutron star binaries are known as high-mass X-ray binaries (HMXB). The high-energy emission in these systems is due to accretion of Be stellar wind material onto the neutron star surface. Although HMXB show pulsed X-ray emission with periods in

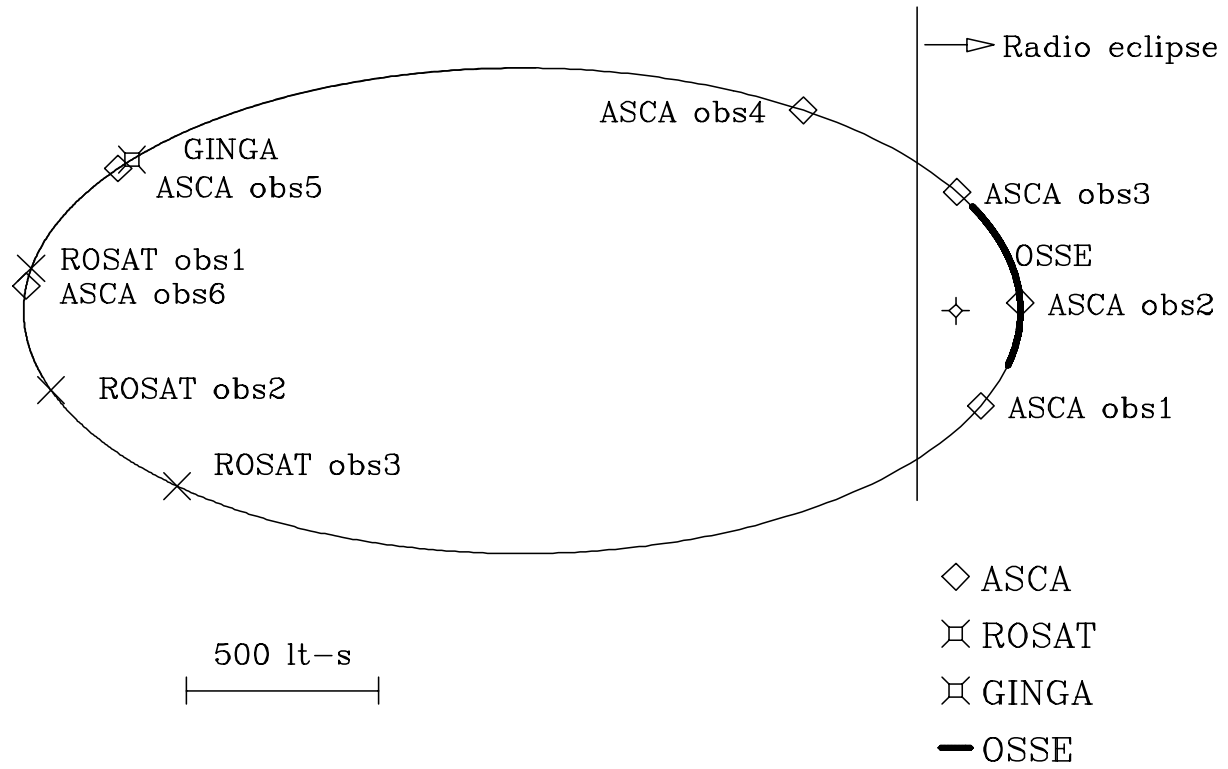


Figure 1.4: Binary orbit of the PSR B1259-63/SS 2883 system. An elliptical line shows an orbit of PSR B1259-63 and a diamond with a cross in the ellipse indicates the center of gravity of the system. The figure also shows the positions of PSR B1259-63 when observed with *ASCA* (this work), *ROSAT* (Cominsky et al. 1994; Greiner et al. 1995), and *Ginga* (Makino and Aoki, private communication) with various marks on the orbit. The *OSSE* instrument on the *CGRO* satellite observed PSR B1259-63 for three weeks during the periastron passage in 1994 as indicated with a thick line on the orbit. When the pulsar is at the right side of the vertical line in the figure, no radio pulsation was detected and the radio flux decreased significantly (radio eclipse) (Johnston et al. 1992b).

the range $0.069 \text{ s} \lesssim P \lesssim 10^3 \text{ s}$ (Bradt and McClintock 1983), radio pulsations have never been detected from any such system. The PSR B1259-63/SS 2883 system is, therefore, unique among these Be/neutron star binaries in the sense that the neutron star appears to be a normal radio pulsar when it is far from its companion. PSR B1259-63, together with PSR J0045-7319, define a new class of radio pulsar binaries: pulsars with massive, non-degenerate companions.

1.3 Past Observations of the System

The distance to the PSR B1259–63/SS 2883 system is relatively uncertain. From the dispersion measure (DM) of the pulsar and a model for the galactic electron distribution (Taylor and Cordes 1993), the estimated distance to the source is 4.6 kpc, although DM-derived distances are uncertain often to a factor of ~ 2 . Johnston et al. (1994) argue on the basis of photometric observations that the distance to SS 2883 cannot be greater than 1.5 kpc, in conflict with that deduced from the pulsar DM. Given the large uncertainties inherent in the DM-derived distance model, the smaller distance seems more likely. In this thesis we adopt a compromise distance of 2 kpc.

Optical observations in the direction of the pulsar have revealed a 10th magnitude B2e star, SS 2883, at a position coincident with the pulsar’s position obtained via radio timing observations within $\sim 2''$. From the positional coincidence of SS 2883 and PSR B1259–63, together with the evidence for a periastron radio eclipse of the pulsed signal in 1990, Johnston et al. (1992b) conclude SS 2883 is the companion star of the pulsar. The pulsar’s mass function implies its orbital companion has a mass greater than $3.2 M_{\odot}$, assuming a $1.4 M_{\odot}$ neutron star. From the spectral type, Johnston et al. (1994) deduce a mass for SS 2883 of $10 M_{\odot}$ and a radius of $6 R_{\odot}$.

Be stars are characterized by strong optical emission lines of ionized hydrogen and excess continuum radiation at near and far infrared and radio wavelengths. All of these characteristics suggest the presence of a dense, slowly expanding wind (Dougherty et al. 1994; Waters et al. 1991; Taylor et al. 1990; Cote and Waters 1987; Waters et al. 1988). However, UV observations of asymmetric blue-shifted absorption in resonance lines of C IV and Si IV suggest the presence of a fast, low-density wind (Snow 1982). These contradictory observations are reconciled in the so-called “disk” model (e.g. Waters 1986). In the disk model the $H\alpha$ emission and infrared excesses are produced in a slowly-expanding dense wind concentrated in the equatorial plane, while the fast wind of low density coexists in the polar region. The disk model is largely empirical and the origin of the equatorial concentration is poorly understood. However, it is commonly assumed that it is caused by the large angular velocities which have been observed in Be stars.

The first attempt to detect X-rays from the PSR B1259–63/SS 2883 system was done by the *Ginga* satellite. However, the *Ginga* failed to detect significant X-rays from the system (Makino and Aoki, private communication). The first report of a low-level X-ray detection was by Cominsky et al. (1994) who observed the system just after apastron using *ROSAT* in September 1992 (“*ROSAT* obs2” and “*ROSAT* obs3” in Figure 1.4). The observed X-ray luminosity in the *ROSAT* band was $(0.07 - 2) \times 10^{33} \text{ erg s}^{-1}$, depending on

the assumed spectral model. Also, a recent analysis of public archive *ROSAT* data taken just before apastron in February 1992 (“*ROSAT* obs1” in Figure 1.4), reveals significant X-ray emission at level consistent with the result by Cominsky et al. (1994) (Greiner et al. 1995). Statistics in both detections were poor and little spectral information is available.

The radio pulsations from the pulsar were detected at the same epochs as past X-ray observations were performed. A hint of a radio eclipse was observed by Johnston et al. (1992b) during the periastron passage in 1990. From the middle of December in 1993 to the beginning of February in 1994, *i.e.*, for three months centering around the recent periastron passage, radio pulsations were not detected. Based on radio timing observations covering two recent periastron passage, Manchester et al. (1995) reported very small sudden increase in pulse period with $\Delta P/P \approx 10^{-9}$ as listed in Table 1.1.

Chapter 2

Instrumentation

2.1 ASCA Satellite

ASCA (Advanced Satellite for Cosmology and Astrophysics) satellite (Tanaka et al. 1994), the fifteenth scientific satellite of Institute of Space and Astronautical Science (ISAS), is the fourth Japanese X-ray observatory succeeding *HAKUCHOU*, *TEMMA*, and *GINGA* satellites. It was launched by the M-3SII rocket No. 7 at 11 a.m. on February 20, 1993 (JST) from Kagoshima Space Center (KSC) in Uchinoura-cho, Kagoshima, Japan. It orbits on a nearly circular orbit with its height about 520km at its perigee and about 620km at its apogee. It weighs about 420kg and the length of an extensible optical bench (EOB) is about 4.7m, while it was 2.8m when launched. Figure 2.1 shows a schematic drawing of *ASCA* satellite in orbit. A “satellite coordinate” is defined with the Z-axis aligned with EOB and the Y-axis with the solar cell paddle. It is also shown in Figure 2.1 for reference.

ASCA features imaging and spectroscopic capabilities with a large effective area and the highest energy resolution ever achieved in a wide energy band, which ranges from 0.5 keV to 10 keV. It carries four X-ray telescope (XRT), two X-ray CCD cameras (Solid state Imaging Spectrometer; SIS) at two of their focal planes, and two gas scintillation imaging proportional counters (Gas Imaging Spectrometer; GIS) at the other two of them. The arrangement of these instruments is shown in Figure 2.2.

2.2 XRT

ASCA XRT consists of a large number of conical thin foil reflectors to fill its aperture nested with their surface seen almost edge-on. It was developed by Dr. P. J. Serlemitsos and features a large effective area and high throughput over a broad energy band up to

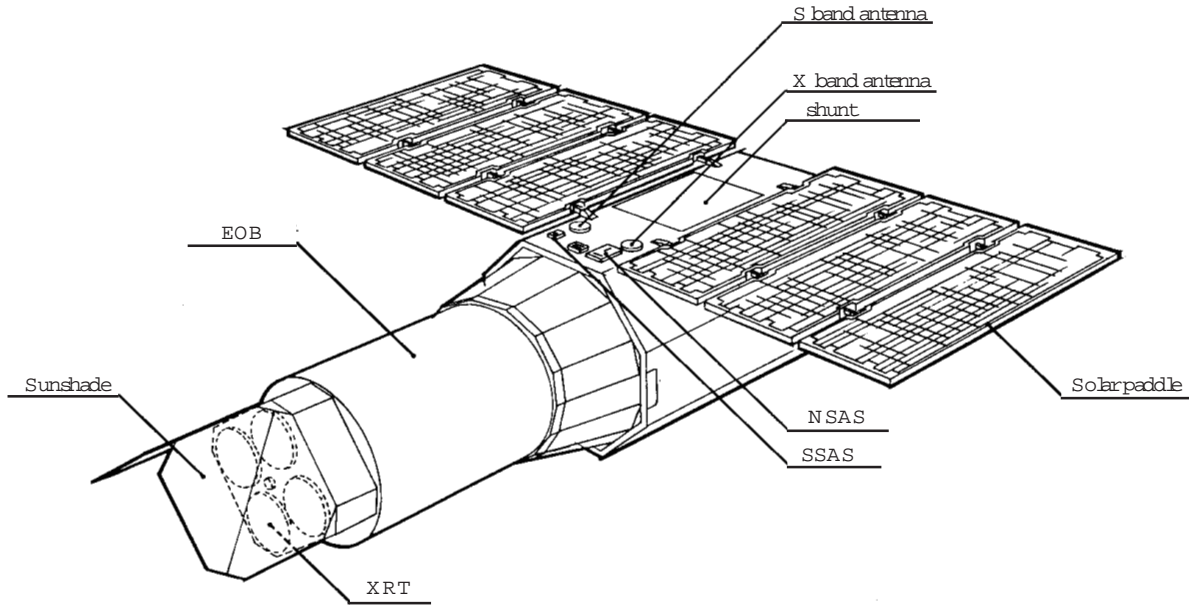


Figure 2.1: Schematic drawing of *ASCA* satellite. A “satellite coordinate” is defined with the Z-axis aligned with EOB and the Y-axis with the solar cell paddle.

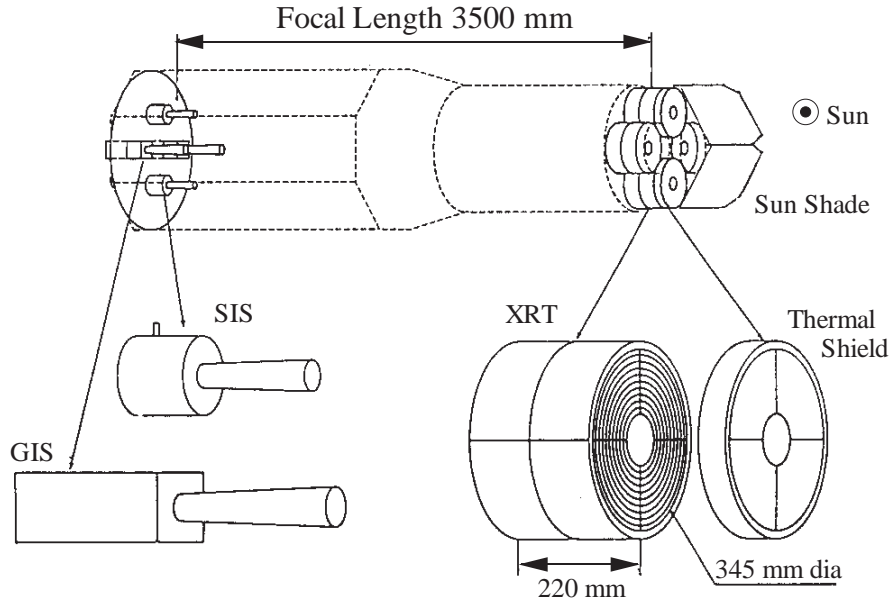


Figure 2.2: Arrangement of instruments on *ASCA* satellite.

10 keV (Serlemitsos et al. 1995). Four XRT’s are on-board *ASCA* satellite and placed at the top of EOB. They were produced cooperatively by Nagoya University, NASA Goddard Space Flight Center (NASA/GSFC), and Institute of Space and Astronautical Science (ISAS).

2.2.1 Wolter Type I Mirror

The Wolter type I mirror focuses incident rays with two reflectors of different shapes, a paraboloid and a hyperboloid. A schematic drawing of the Wolter type I mirror is shown in Figure 2.3. Since efficient reflection of X-rays occurs only at small grazing angles, the surface of the reflectors must be seen almost edge-on. Therefore, the effective area of the reflectors is much smaller than their geometrical area by a factor of 100. To achieve a large effective area, over a hundred nested thin foils are used for *ASCA* XRT. The ratio of an effective aperture against a geometrical aperture is also very large, over 60%, by this method. It is not realistic, however, to shape a thin foil into a paraboloid or a hyperboloid. Therefore, a conical surface is used as an approximation instead. This reduces the image quality, of course, but the roughness of the reflectors' surface dominates the broad point spread function with its half power diameter of 3 arc-minutes.

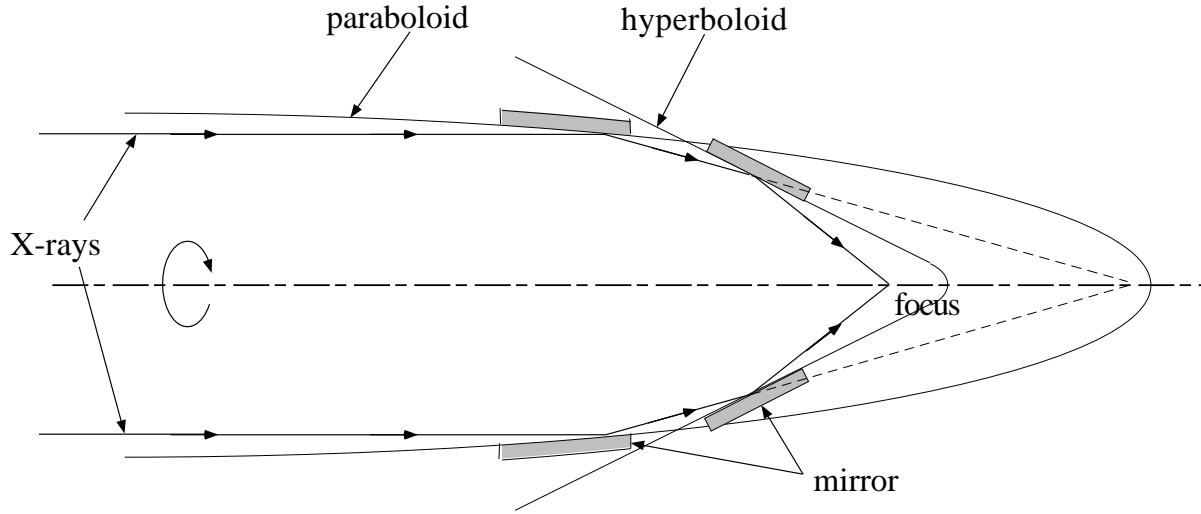


Figure 2.3: Schematic drawing of the Wolter type I mirror.

2.2.2 Design and Performance

The substrate of *ASCA* XRT is $127\ \mu\text{m}$ aluminum foil. After being shaped into a conical form, the foil was coated by $\sim 10\ \mu\text{m}$ acrylic lacquer to smooth its surface, and $500\ \text{\AA}$ of gold was vacuum deposited over the acrylic layer. 120 of these foils are filling XRT annulus aperture with inner and outer diameter of 120 and 345 mm, respectively. Two layers of these mirrors were installed to approximate the Wolter type I mirror. Also, in front of XRT, a thermal shield is placed to avoid distortions of reflectors caused by the thermal gradient of XRT. Design parameters and performance of XRT are shown in Table 2.1.

Table 2.1: Design parameters and performance of *ASCA* XRT

Mirror substrate	127 μ m
Mirror surface	Acrylic lacquer 10 μ m + Au (500 \AA)
Mirror length	100mm
Number of mirrors	120 foils
Inner (outer) diameter	120 (345) mm
Focal length	3500 mm
Incident angle	0.24° \sim 0.7°
Total weight ^{a)}	\sim 40 kg
Geometrical area	558 cm ² /telescope
Field of view	24 arcmin. (FWHM @ 1 keV) 16 arcmin. (FWHM @ 1 keV)
Energy range	\leq 10 keV
Effective area ^{a)}	\sim 1300cm ² (1 keV) \sim 600cm ² (7 keV)
Half power diameter	\sim 3 arcmin.

a) total of four XRT's.

The energy dependence of the effective area is shown in Figure 2.4. Effective areas of *ROSAT* and *Einstein* satellites are also shown in Figure 2.4 for comparison. We can see that the mirrors efficiently reflect X-rays up to 10 keV. The effective area is reduced for an X-ray source far from the optical axis of XRT, as shown in Figure 2.5.

An image by XRT is shown in Figure 2.6. The “four leaves shape” is due to the structure of XRT, which consists of four quadrant housings installing X-ray reflectors. Since the boundaries of the quadrants do not reflect X-rays, the reflection efficiency is significantly small at the directions corresponding to the boundaries. The point spread function (PSF) of XRT for a point source is also shown in Figure 2.6. The plots are shown for four cases for comparison: when XRT images 3C273 with SIS in the energy band below 2 keV, with SIS above 2 keV, with GIS below 2 keV, and with GIS above 2 keV. In Figure 2.6 the PSF measured with GIS is broadened by the point spread function of GIS.

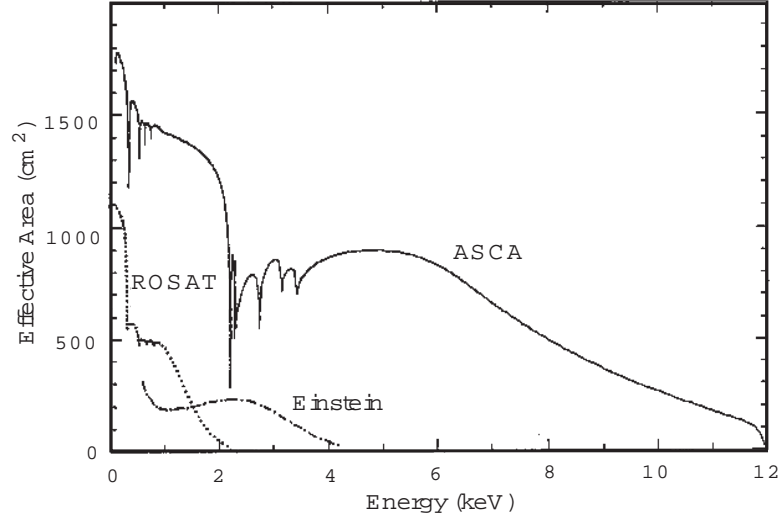


Figure 2.4: Effective area of *ASCA* XRT. Effective areas of *ROSAT* and *Einstein* satellite are also shown for comparison.

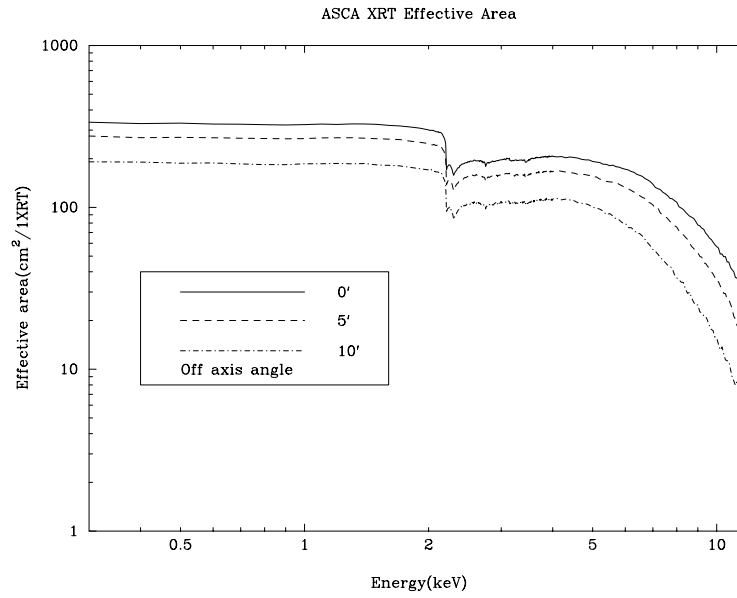


Figure 2.5: Effective areas of *ASCA* XRT when an X-ray source is at 0', 5', and 10' away from the optical axis.

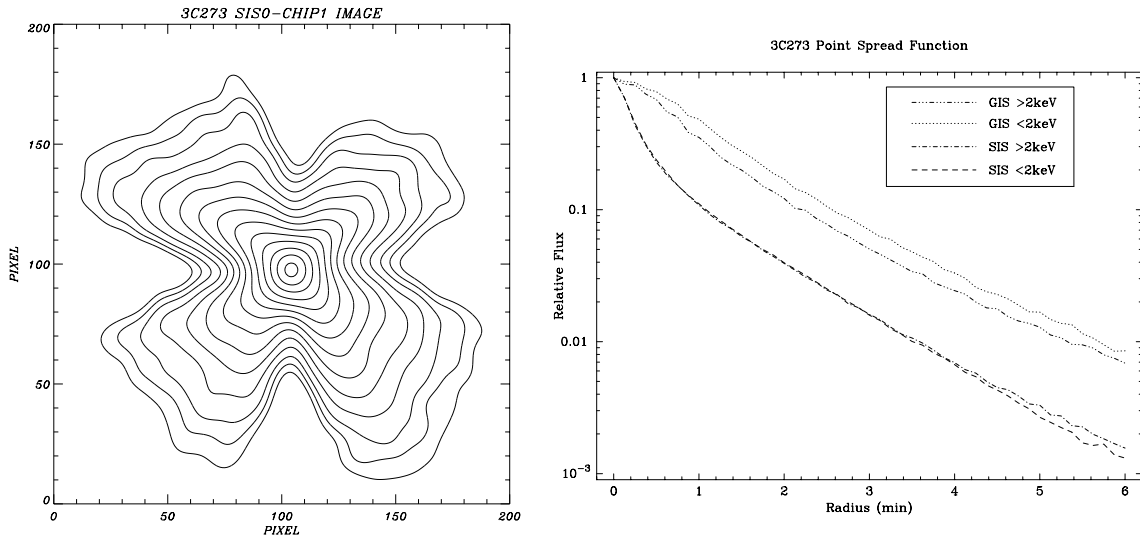


Figure 2.6: (left panel) Image of the point source, the quasar 3C273, by XRT. The “four leaves shape” is due to a structure of XRT, which consists of four quadrant housings installing X-ray reflectors.

(right panel) The point spread function of XRT for the point source, the quasar 3C273. Plots are shown for four cases for comparison: when XRT images 3C273 with SIS in the energy band below 2 keV, with SIS above 2 keV, with GIS below 2 keV, and with GIS above 2 keV. The PSF measured with GIS is broadened by the point spread function of GIS.

2.3 SIS

ASCA SIS is an X-ray sensitive CCD camera and features high energy resolution and fine positional resolution. Two SIS's (hereafter SIS0 and SIS1) are on-board the *ASCA* satellite and placed in the focal planes of two of the four XRT's. They were developed by the Massachusetts Institute of Technology (MIT), Osaka University, and Institute of Space and Astronautical Science (ISAS) in cooperation.

2.3.1 System Description

SIS consists of four X-ray CCD's, a housing, analog electronics (SIS-AE), and digital electronics (SIS-DE). Below are brief descriptions of these components.

The four CCD's align in a square with narrow gaps between the CCD's. Each CCD chip has 422 lines, each of which consists of 420 square pixels, each $27\mu\text{m}$ on its side. The dimensions of the CCD chip are $11\text{mm} \times 11\text{mm}$ which covers $11' \times 11'$ in the sky, so that the field of view of SIS is $23' \times 23'$ including the gaps. Figure 2.7 shows the alignment of the four chips with their dimensions. Design parameters and performance of SIS are summarized in Table 2.2.

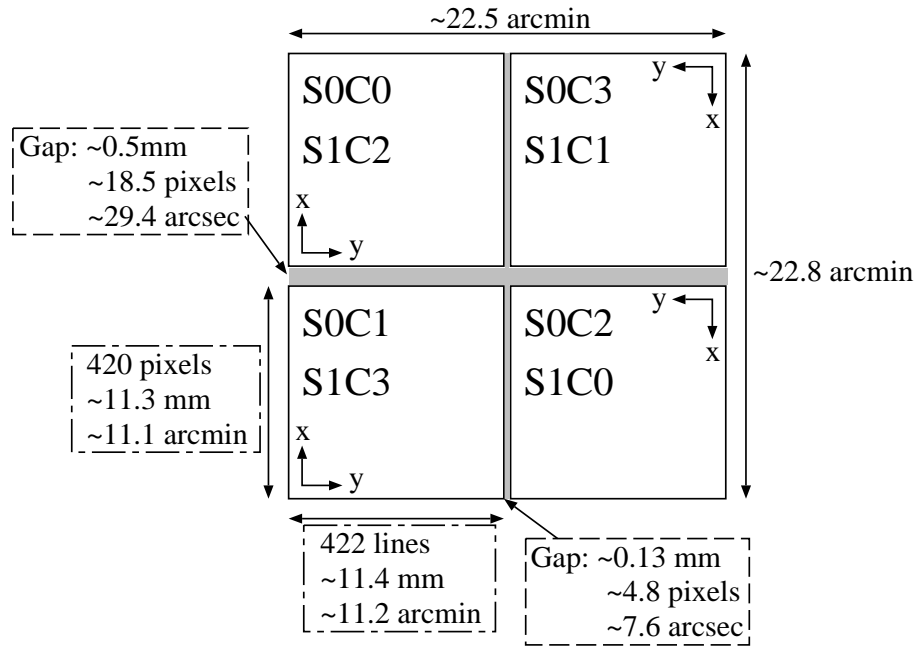


Figure 2.7: Alignment of the four CCD chips in SIS.

The X-ray CCD (Charge Coupled Device) for SIS is a frame transfer type CCD and has the same structure as an optical CCD of the same type. Its detection part is made of an Si semiconductor of p-type and n-type, connected to each other through p-n junction.

Table 2.2: Design parameters and performance of *ASCA* SIS

Irradiation Method	Front irradiation
Charge Transfer Method	Frame Transfer
Clock	3-phase drive
Number of pixels in Image Region	420 pixels \times 422 lines per chip
Pixel Size	27 μm
Area	11 \times 11 mm ² per chip
Field of View	11 \times 11 square arc minutes per chip
Thickness of Depletion Layer	$\sim 40\mu\text{m}$
Drive temperature	$\sim -62^\circ\text{C}$
Energy Band	0.4-12 keV
Quantum Efficiency	80% at 6 keV
Energy Resolution	2% at 5.9 keV (FWHM)

An insulator layer made of SiO_2 is attached on the front surface of the n-type Si, and electrodes are built on it. By supplying specific patterns of voltages on the electrodes, charges in a pixel are transferred from a pixel to the next pixel. An electrode is also attached on the back. A depletion layer is developed in the device by supplying a bias voltage between the electrodes on the front and on the back.

The CCD chips are mounted in a housing as shown in Figure 2.8. They are cooled down to -62°C with a thermo-electric cooler (TEC) from the back to reduce the thermal noise. They can also be heated by a film-type heater on the back in order to evaporate adsorbed molecules. They are surrounded by a Multi Layer Insulator (MLI) with a window in the direction of their aperture to block heat input from the environment. The aperture is covered by an optical blocking filter, or 1000 \AA Lexan film coated with 400 \AA aluminum, in front of the CCD chips. The whole CCD's are supported by Lexan supports and shielded from charged particles by poly-ethylene of 4 cm thickness and aluminum of 1.9 cm thickness on a side, aluminum plate of 3.5 cm thickness at the bottom, and aluminum of 2.1 cm thickness at the top except for the aperture. A baffle is attached to shield stray light and high energy X-rays as a background.

Two SIS-AE's are on-board corresponding to SIS0 and SIS1 respectively. Electric signals from SIS are fed into SIS-AE and their pulse heights are converted into digital signals with analog-to-digital converters (ADC). SIS-AE also generates driving clocks for the CCD chips and monitors and controls the temperature of the CCD chips. There are

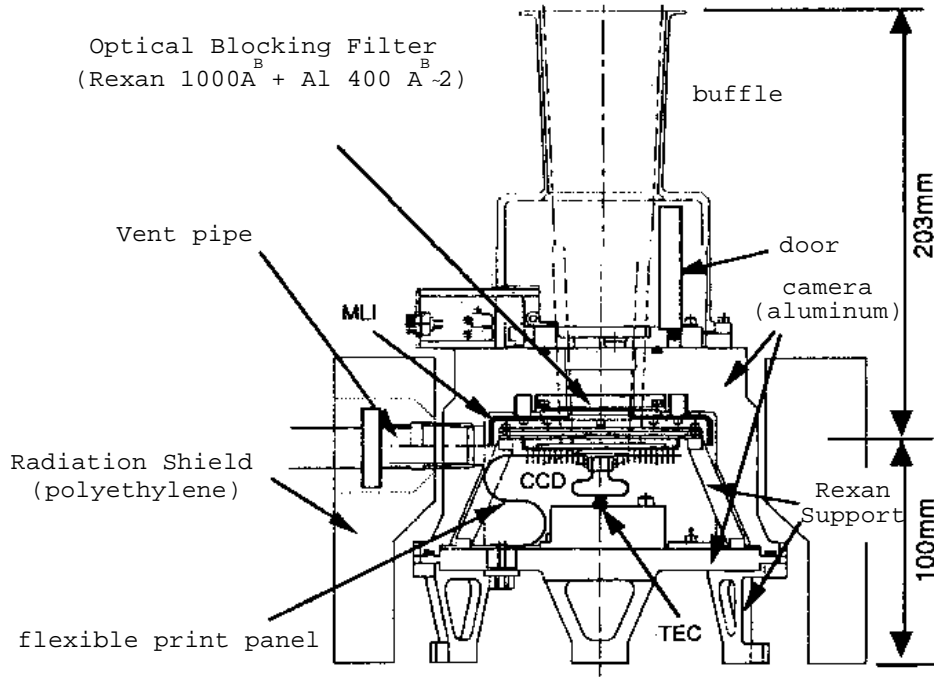


Figure 2.8: Cross sectional view of SIS.

two SIS-DE's corresponding to two SIS-AE's. SIS-DE picks up X-ray events in the digital signals from SIS-AE with two digital signal processors (DSP) and sends them to a data processor (DP), which commonly processes data from SIS and GIS and edits them into a telemetry format (see §2.6 for details). A more detailed description of on-board data processing of SIS data is given in §2.3.3.

2.3.2 Principle of X-ray Detection

X-rays are absorbed in a depletion layer through photoelectric absorption. The photoelectron travels, losing its energy through ionization and excitation processes, and generates electron-hole pairs in the device. Since the number of pairs is proportional to the energy of an incident X-ray, one can measure the energy by measuring the number of pairs. The electrons and holes drift in opposite directions due to an electric field in the device; the electrons move to the front of the CCD chip and are held in a region under the electrodes; the holes go to the back and drain into electrodes on the back. The detection efficiency for X-rays is determined in this structure. Since low energy X-rays are significantly absorbed by the electrodes on the front surface, the efficiency is determined by the thickness and the structure of the electrodes. For high energy X-rays the thickness of

the depletion layer limits the efficiency since X-rays with higher energy pass more easily through the depletion layer. The energy dependence of the detection efficiency is shown in Figure 2.9.

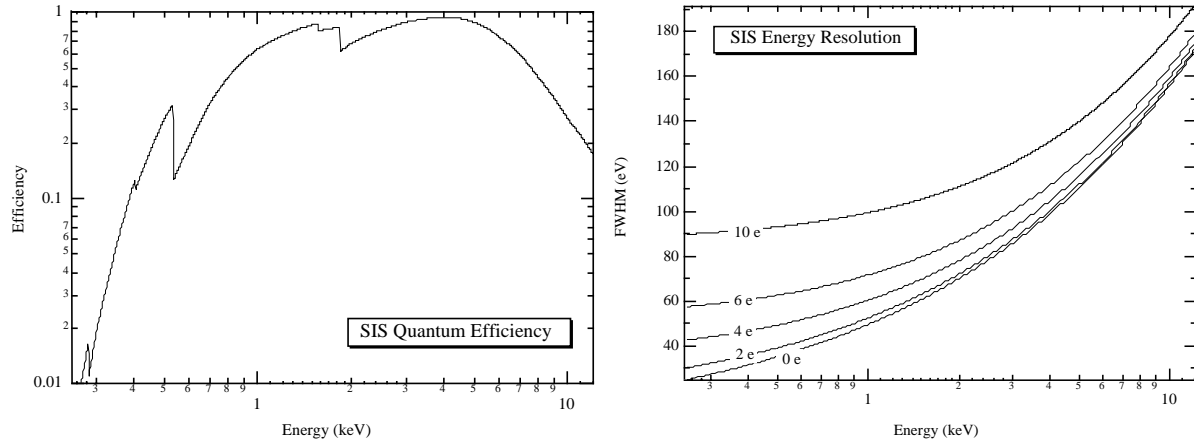


Figure 2.9: (left panel) Detection efficiency of SIS. K-edges of O (0.53 keV), Al (1.56 keV), and Si (1.84 keV) are clearly seen in the figure.

(right panel) Energy resolution of SIS as a function of incident energy. Plotted are the energy resolutions with different read-out noise N . The read-out noise are shown as the equivalent number of electrons.

In the case of a frame transfer CCD, half of the CCD aperture is covered by a shield so as not to detect X-rays from the aperture. The half not covered by the shield is called a “image region” and another half is called a “frame store region”. Charges induced by X-rays are transferred in parallel from the image region into the frame store region in a relatively short time (parallel transfer). Then charges in the frame store region are transferred by one pixel in the same direction of the parallel transfer so that charges in pixels at the edge of the frame store region are moved into a “shift register” next to the frame store region. In the shift register charges are transferred in a perpendicular direction to the parallel transfer and fed to an amplifier at a read out node pixel by pixel (serial transfer). In this way all the pixels are read out at one amplifier, so a large number of pixels can be easily read out with simple electronics; however, it takes a relatively long time, which reduces the time resolution.

The energy resolution of the CCD is determined by 1) fluctuation of the number of electrons in a electron cloud, 2) generation of thermal electrons, and 3) read-out noise of the first stage amplifier. Since the generation of thermal electrons can be suppressed by cooling the CCD, its contribution to the energy resolution is negligible. Hence, the

energy resolution is given as

$$\Delta E(\text{FWHM}) = W \sqrt{8 \ln 2 \left(N^2 + \frac{FE}{W} \right)}$$

where E is the energy of incident X-ray, W is the mean ionization energy, N is the equivalent noise power in units of the number of electrons, and F is the Fano factor. For an X-ray CCD for SIS, $W \sim 3.65\text{eV}$, $N \sim 5$, and $F \sim 0.12$. The energy resolution is shown in Figure 2.9 as a function of incident energy. In the figure the energy resolutions with different read-out noise N are plotted.

2.3.3 On-Board Data Processing

Data processing at SIS-DE and DP depend on the operation mode of SIS; there are three observation modes and four diagnostics modes. The observation modes are designed for scientific observations and consists of faint mode, bright mode, and fast mode. In the observation modes the data are processed every four seconds independent of the bit rate (see §2.6 for explanation). The diagnostics modes are used to check the condition of the SIS instrument in orbit and consists of frame mode, integration mode, histogram mode, and dark image mode. The diagnostics modes are available only when the bit rate is high. In addition, the order of reading of the CCD chips can be changed in accordance with the aim of observation (CCD mode). Three CCD modes are designed for standard observations: 1-CCD mode, 2-CCD mode, and 4-CCD mode. The numbers preceding “CCD” in mode names are the number of chips to be read out.

In faint mode and bright mode X-ray images and spectra are simultaneously obtained with poor time resolution of 4s at most. Information on detected X-rays are acquired almost in the same way in both modes, except that the information is compressed in bright mode. 1-, 2-, and 4-CCD modes are available in faint and bright modes. In fast mode high time resolution up to $\sim 16\text{ms}$ is achieved at the cost of imaging capability by projecting an image onto one axis of the CCD chip. The projection is realized by summing charges in the direction of the parallel transfer in the shift register on the chip. One can also obtain spectral information as well as in other observation modes. Only 1-CCD mode is available in fast mode. In Table 2.3 operation mode of SIS are summarized.

We trace here the flow of the on-board data processing for SIS data. SIS-AE converts pulse heights of all the pixels in a CCD chip into integer values of 12 bits length (hereafter PH data). SIS-DE calculates a pixel level of each pixel by subtracting a dark level from each PH data. The dark level is defined as the value of PH data when no X-ray is detected in the pixel and is calculated from PH data in previous exposures. Then SIS-DE searches SIS events defined as pixels satisfying two conditions: 1) their pixel levels exceed an

Table 2.3: Summary of observation modes in SIS

	Faint	Bright	Fast
Time Resolution	4/8/16 sec	4/8/16 sec	16 ms
	(1/2/4CCD mode)		(1CCD mode)
Event Trans. Rate (cts/sec/2 sensors)	128/16/4	512/64/16	1024/128/32
	(High/Medium/Low bit rate)		
Data size per event	128 bits	32 bits	16 bits
CCD ID	2 bits	—	—
Pixel level	12 bits \times 9	11 bits	11 bits
Event position	9 bits \times 2	9 bits \times 2	1 bit
Time stamp	—	—	3 bits
Grade	—	3 bits	1 bits

event threshold and 2) neighboring pixels have pixel levels less than the pixel. The event threshold is set to 100 usually. The number of neighboring pixels to be compared are eight for faint and bright modes and two for fast mode.

The detected events are sent to DP of the satellite. In faint mode DP merely collects a set of information on each detected event; a CCD ID indicating in which chip the event is detected (2 bits), a position of the event (9 bits for each of two axes), and pixel levels of a center pixel and surrounding pixels (12 bits for each pixel) so that the total size of the data is 128 bits per event. In bright mode DP classifies an event by assigning a “grade”. The grade ranges from 0 to 7 depending on the pattern of the pixel levels of neighboring pixels whose pixel levels exceed a split threshold. The split threshold is set to 40 in normal operation. Definitions of grades are shown in Table 2.4 and in Figure 2.10. DP also sums pixel levels which exceed the split threshold and are not of detached corner pixels, and compresses the summed pixel level with 12 bits length into 11 bit data (bit reduction) in the following way;

$$\begin{aligned}
 y &= x & \text{for } 0 \leq x < 2^{10} \\
 y &= (x - 2^{10})/2 + 2^{10} & \text{for } 2^{10} \leq x < 2^{11} \\
 y &= (x - 2^{11})/4 + 2^9 + 2^{10} & \text{for } 2^{11} \leq x < 2^{12}
 \end{aligned}$$

where x is a summed pixel level and y is a compressed one. DP collects the grade of the event(3 bits), the position of the event (9 bits for each of two axes), and the compressed pixel level (11 bits for each pixel) so that the total size of the data is 32 bits per event. In fast mode DP also assigns a grade for each event but in a different way because there are

only two neighboring pixels. The grade in faint mode is 0 or 1 and definitions of grades are summarized in Table 2.4. DP also summed pixel levels if necessary and compressed into 11 bits length as in bright mode. DP collects a grade of the event (1 bit), a flag indicating whether the event is found in a specified region (1 bit), the fine time stamp of the event (3 bits), and a compressed pixel level (11 bits for each pixel) so that the total size of the data is 16 bits per event.

Table 2.4: Summary of grades of SIS.

Faint and Bright mode		
Grade	Name	Pixel(s) exceeding a split threshold
0	single	center pixel only
1	single+	center + corner(s)
2	vertical split	center + vertical (+ detached corner(s))
3	left split	center + left (+ detached corner(s))
4	right split	center + right (+ detached corner(s))
5	single-sided+	center + sided + touched corner (+ detached corner(s))
6	L+square	center + vertical + horizontal (+ detached corner(s)) square pixels (+ detached corner pixel(s))
7	others	other combinations
Fast mode		
Grade	Name	Pixel(s) exceeding a split threshold
0	single	center pixel only
1	others	other combinations

The information collected by DP is edited into a telemetry format, stored into a bubble data recorder (BDR), and transferred to a ground station as described in §2.6.

2.3.4 Fundamental Reduction of SIS data

Several fundamental data reductions have to be performed specially for the analysis of SIS data. Some of them relate to the property of an X-ray CCD camera itself and others are due to the on-board data processing described in §2.3.3. In this section we summarize characteristics commonly seen in SIS data and introduce how to cope with them in an analysis on the ground.

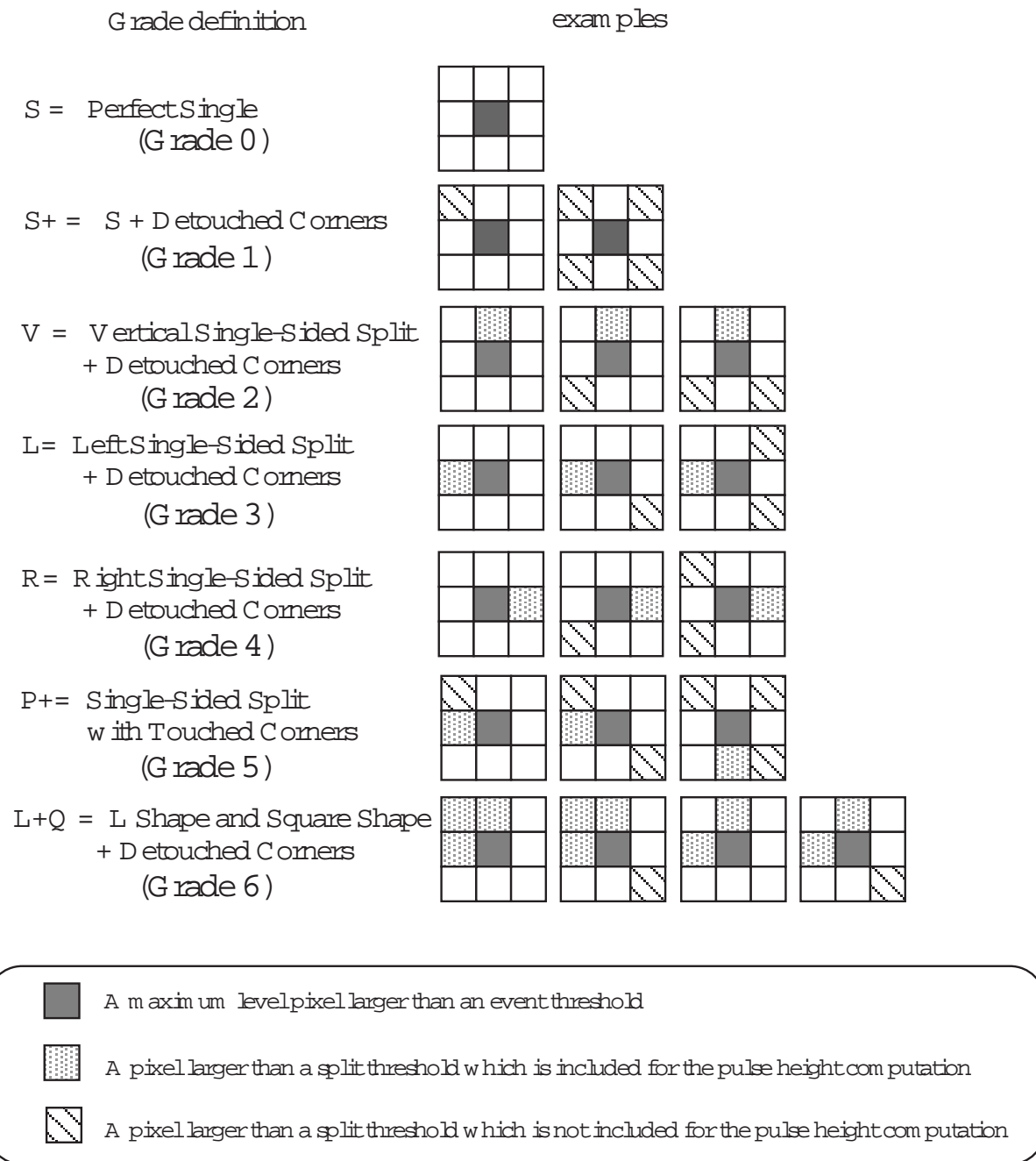


Figure 2.10: Definitions of grades of events.

Hot and Flickering Pixels

A pixel creating events with no incident particle is called a “hot pixel” or a “flickering pixel”. These pixels are those with a large dark current, caused by lattice defects on the insulator layer under electrodes of the CCD (see 2.3.2). The dark current creates a significant amount of charge in the pixel and causes spurious events. If the amount of charge is high enough, spurious events are seen in all the exposures of the CCD. Such a pixel is called a hot pixel and corresponds to a white pixel in an optical CCD. If the dark current is moderate and creates a small charge cloud with statistical fluctuations, spurious events appear not in all the exposures. Such a pixel is called a flickering pixel. Since events from these pixels contaminate results such as a spectrum and an image, these pixels have to be masked in the analysis.

The hot and flickering pixels create spurious events in addition to the normal events due to X-rays. The hot pixels are easy to identify because they create events in all the exposures. The flickering pixels are slightly difficult to distinguish from a normal pixel, but there is a statistical test to find them, as follows. The number of events detected at a flickering pixel becomes larger than those at a normal pixel. Therefore, a pixel can be regarded as a flickering pixel if the number of events at the pixel largely exceeds the average among surrounding pixels. Precisely stated, first the probability that the number of events exceeds the detected one, assuming the Poisson distribution with an expectation value equal to the average among neighborhood, is estimated. The pixel is identified if the Poisson probability is larger than a given threshold. In a standard analysis the average is calculated from 5×5 pixels centering a pixel of interest. The threshold probability is set to $10^{-5.25}$, which corresponds to a probability that one out of all the pixels in a chip (422×420 pixels in total) exceeds the threshold by chance, namely, $1/(420 \times 422)$.

Echo

A pixel level suffers an artificial increase by an “echo” phenomenon, which originates from a transitional property of SIS-AE. In SIS-AE an analog signal from the CCD leaves an extra signal after the main signal as a result of a “ringing” effect. A significant pulse height remains even at a time when the signal from a next pixel is processed. As a result, a pixel level at a certain pixel is added by a constant fraction to the pixel level at the pixel which is read out next, *i.e.*, at its right-hand pixel. The fraction is called “echo fraction” and is known to increase. Figure 2.11 shows averaged pixel levels of right-hand pixels over numbers of events against the pixel level at the center pixel for SIS0 and SIS1 for several observation periods. The solid lines in the figure indicate a straight line model

for each plot. The figure indicates a gradual increase of the echo fraction.

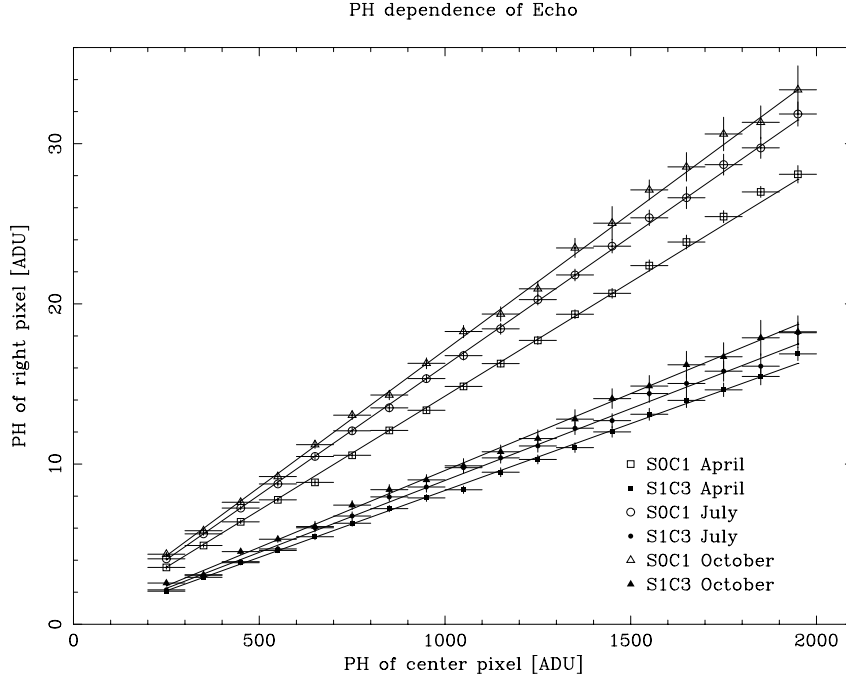


Figure 2.11: Echo phenomenon. Plotted are averaged pixel levels of right-hand pixels versus pixel levels of the center pixels for SIS0 and SIS1 for several observation periods. In the figure the solid lines indicate a straight line model to each plot. The figure indicates a gradual increase of the echo fraction.

In the analysis, the echo fraction can be calculated from the observed data by accumulating SIS events in the data to plot pixel levels of right-hand pixels against those of the center pixels, as in Figure 2.11. In this stage the pixel level of the right-hand pixel is subtracted from that of the left-hand pixel to cancel an effect of the dark frame error described elsewhere in this section. Fitting the plot to a straight line gives the echo fraction as its inclination. In addition, the echo fraction at the time of interest is known from a calibration database which includes information on secular variation of the echo fraction. Faint mode data can be corrected to remove the echo phenomenon by subtracting pixel levels of the center pixel from that of right-hand pixels by the echo fraction for an observation period. In bright mode data, however, only summed pixel levels are obtained so that no correction to the data can be performed. In this case one should use a response matrix taking into account the echo phenomenon.

Dark Frame Error (DFE)

A dark frame error (hereafter DFE) is a residual dark level (see §2.3.3 for definition of a dark level) causing pixel levels to be shifted by a constant amount, depending on the

SIS condition during an observation. The DFE arises from incomplete estimation of dark levels in calculating pixel levels in SIS-DE. The dark level is calculated as an average of raw PH data (see §2.3.3 for definition of PH data) which distributes asymmetrically around the true dark level. Figure 2.12 shows a distribution of pixel levels of corner pixels in 3×3 pixels, *i.e.*, upper left, upper right, lower left, and lower right pixels in reference to the central pixel. These pixels rarely include a charge cloud so that the distribution represents a distribution of pixel levels of pixels with no incident particle. In Figure 2.12 the distribution tends to have a higher values at positive pixel levels than those at negative pixel levels, due to a slight contamination of events with low pixel levels. This asymmetry makes the calculated dark level higher than the true one, therefore, DFE value is usually negative.

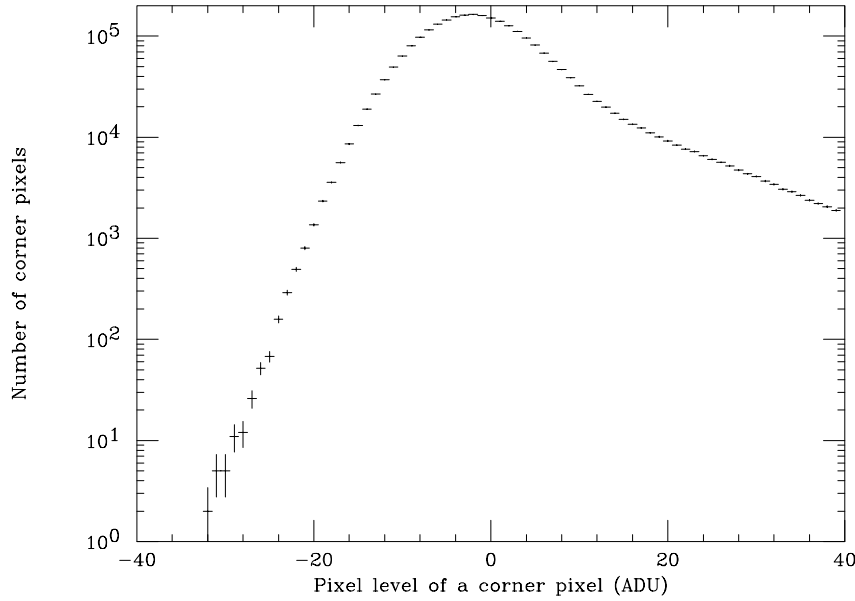


Figure 2.12: Distribution of pixel levels of corner pixels, which represents a distribution of pixel levels of pixels with no incident particle. One can clearly see that the distribution is asymmetric, and that it has higher values at positive pixel levels than those at negative pixel levels.

The DFE is mainly due to light input in an optical band, because such light leaks into the CCD chips and increases number of pixels with low pixel levels. Therefore, DFE is nearly zero when the satellite is at night, and relatively high otherwise. In order to correct the DFE, this characteristic is made use of; the distribution of pixel levels at corner pixels are accumulated for each short time interval, each 64s usually, and compared with a template shown in Figure 2.12 by cross-correlating them. The template is created by collecting events when the satellite is at night by the *ASCA* calibration team and supplied by the *ASCA* Guest Observer Facility (*ASCA* GOF) at ISAS and NASA/GSFC. This estimation is repeated throughout an observation period, and the time history of

DFE values are obtained. Usually the FTOOLS “faintdfe” is used to do this task and it is also supplied by the *ASCA* GOF. For faint mode data the estimated DFE are subtracted from pixel levels of all the pixels sent to the ground. Since no DFE correction can be made for bright and fast mode data, the effect of DFE on a spectral analysis are eliminated by using an appropriate response matrix.

Charge Transfer Inefficiency (CTI)

Charge transfer inefficiency (CTI) is defined as the probability that an electron in a charge cloud is not transferred from a pixel to the next pixel. The CTI is caused by charge traps by lattice defects in channels of electrons in the CCD chips. Since such lattice defects are created by charged particles in orbit, CTI increases gradually.

Suppose that N electrons are transferred n times in the CCD. When one assumes CTI is the same in all pixels, then the number of electrons detected at the read out amplifier N_{out} is

$$N_{out} = N(1 - n \times f_{CTI}),$$

where f_{CTI} is CTI at an observation period. Therefore, CTI reduces the apparent center energy of line X-rays by a constant fraction depending on the position of the X-ray source on the CCD chip. In reality CTI depends on the clocking frequency. As a result, the parallel and serial transfers may cause different CTI's. These CTI's were measured by observing well-known supernova remnants, such as Puppis A, IC 443, and Cassiopeia A, which emits line X-rays with their center energies known. In Table 2.5 results from measurements in August 1994 are summarized.

In an analysis on the ground CTI can be corrected, except for fast mode data. The method of the correction is straightforward: reading a CTI table to obtain CTI at an observation period, calculating a reduction factor of energy scale for each event by multiplying CTI by the number of transfers of electrons of the event, and dividing the pixel level of the event by the reduction factor. By doing this calculation for both parallel and serial CTI's individually, one finally obtains a pixel level of each event which is proportional to the number of electrons of the event, therefore, proportional to incident energy of the X-ray.

Table 2.5: Charge Transfer Inefficiency measured in August 1994^{a)}

Chip	Parallel CTI ^{b)}	Serial CTI ^{b)}
S0C0	2.85 ± 0.38	3.07 ± 0.50
S0C1	2.31 ± 0.18	3.09 ± 0.22
S0C2	3.19 ± 0.28	2.57 ± 0.39
S0C3	2.39 ± 0.38	6.47 ± 0.51
S1C0	3.42 ± 0.31	6.20 ± 0.51
S1C1	2.14 ± 0.30	2.83 ± 0.40
S1C2	2.13 ± 0.35	5.22 ± 0.49
S1C3	2.38 ± 0.20	-0.23 ± 0.25

a) Errors are quoted with 90% confidence level.

b) In units of 10^{-5} transfer⁻¹

2.4 GIS

ASCA GIS is a gas scintillation imaging proportional counter and features high time resolution and high detection efficiency for hard X-ray photons. Two GIS's (hereafter GIS2 and GIS3) are on-board the *ASCA* satellite and placed on focal planes of another two of the four XRT's. They were produced by University of Tokyo and Institute of Space and Astronautical Science (ISAS).

2.4.1 System Description

GIS consists of a gas cell, a position sensitive photo-multiplier (Imaging Photo-Multiplier Tube; IPMT), a high voltage unit, a housing, and electronics (GIS-E). Below are brief descriptions of these components.

The gas cell has a cylindrical shape with ~ 60 mm diameter and ~ 25 mm height. A schematic drawing of a cross sectional view of a gas cell and a position sensitive photo-multiplier tube of GIS are shown in Figure 2.13. A circular aperture of 50mm diameter is covered by a Be foil of $\sim 10\mu\text{m}$ thickness supported by two stainless meshes with 1.2mm pitch, 0.15mm height, 0.08mm width, and 87% transmission. The meshes are supported by a supporting grid made of molybdenum with 5mm pitch, 3.5mm height, and 0.1mm thickness. The field of view of GIS is circular with 50' diameter in the sky. Xe gas (96%) and He gas (4%) are filled in the gas cell. In front of the gas cell a plasma shield is placed to protect GIS from radiation damage. The gas cell is divided into two regions: a drift region and a scintillation region. IPMT is attached below the gas cell as shown in Figure 2.13. They are optically connected with each other through a quartz window at the bottom of the gas cell and a bialkali photo-electrode at the top of IPMT. Design parameters and performance of GIS are summarized in Table 2.6.

Table 2.6: Design parameters and performance of GIS

Energy Band	0.7-15 keV
Energy Resolution	8% at 5.9 keV (FWHM)
Effective Area	50 mm diameter
Positional Resolution	0.5 mm (FWHM)
Time Resolution	$\sim 61 \mu\text{sec}$ (Minimum in PH Mode)
	1.95 ms (Minimum in MPC Mode)

The high voltage unit is attached at the side of the detector as shown in Figure 2.14.

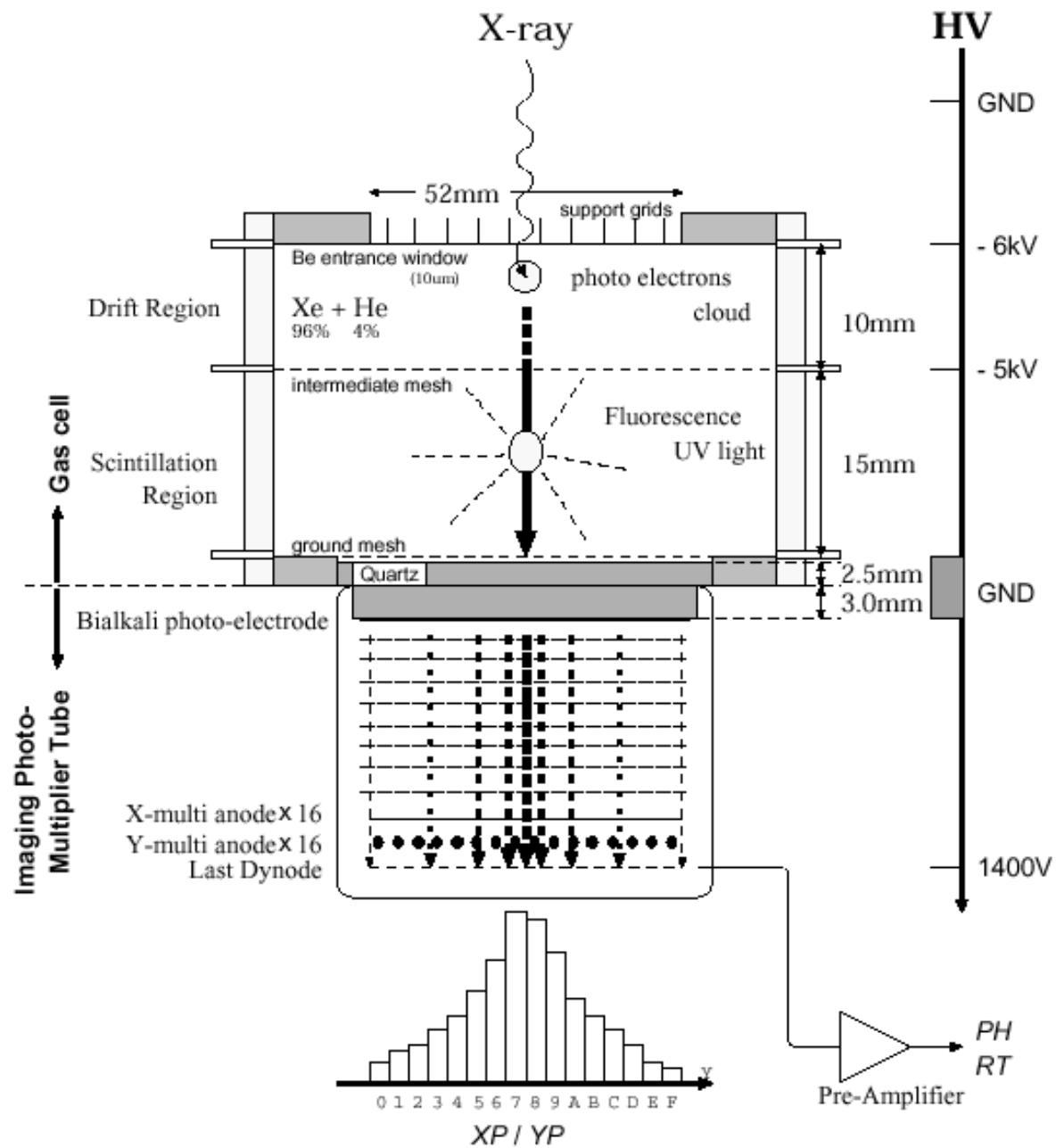


Figure 2.13: Cross sectional view of a gas cell and a position sensitive photo-multiplier tube of GIS. The voltage of each part of the detector supplied by a high voltage unit is shown at the right of the figure for reference. A schematic drawing of an X-ray detection is also shown.

The high voltage unit supplies appropriate voltages to the gas cell and IPMT as shown at the right in Figure 2.13. A bleeder is placed below IPMT and supplies voltages to a dynode and to the anodes of IPMT by dividing a high voltage from the high voltage unit. At the end of GIS2 a radiation belt monitor (RBM) is installed to monitor the flux of charged particles. When the flux exceeds a given threshold, RBM asserts an “RBM flag” which warns GIS-E of high level of radiation. When the RBM flag is detected, GIS-E controls the high voltage unit to reduce the voltage in order to protect GIS’s from the radiation.

One GIS-E is on-board the satellite and processes signals from GIS2 and GIS3. GIS-E converts analog signals from two GIS’s into digital signals with two 12 bits ADC and four 8 bits flash ADC. The CPU in GIS-E collects and edits this information and sends it through a FIFO (First-In First-Out logic) to the DP of the satellite, which commonly edits SIS data and GIS data into a telemetry format (see §2.6 for details). GIS-E also supplies power to two GIS’s and RBM, controls the high voltage unit and the preamplifier to operate GIS, and handles the RBM flag to prevent the detectors from radiation damage. A more detailed description of on-board data processing of GIS data are shown in §2.4.3.

2.4.2 Principle of X-ray Detection

X-rays are absorbed in the drift region of the gas cell through photoelectric absorption (see Figure 2.13). The photo-electron travels, losing its energy through ionization and excitation processes, and generates electron-ion pairs in the gas cell. Since the number of pairs is proportional to the energy of an incident X-ray, one can measure the energy by measuring the number of pairs. The electrons and ions drift in opposite directions due to an electric field in the gas cell; the electrons move into the scintillation region and the ion go to the aperture and are absorbed by the Be window. Since the electric field in the drift region is not so strong (< 1 keV/cm) that it can accelerate electrons to ionize or excite Xe atoms in the gas, the number of electrons in the cloud is conserved and no scintillation occurs.

In the scintillation region the electron cloud is accelerated by a stronger electric field and ionizes or excites Xe atoms in the gas, which generates fluorescent lights of wavelength ~ 170 nm (ultraviolet) when they recover to the ground state. The electric field here, however, is not so strong (< 6 keV/cm) that gas amplification takes place. The ultraviolet lights are emitted along the path of the electron cloud and distribute on a bialkali photo-electrode of IPMT centering around the position of the X-ray detection. The lights are absorbed by the photo-electrode and converted into electric signals by IPMT. An electric signal from the last dynode rises in $\sim 2\mu$ s because arrival times of the fluorescent lights

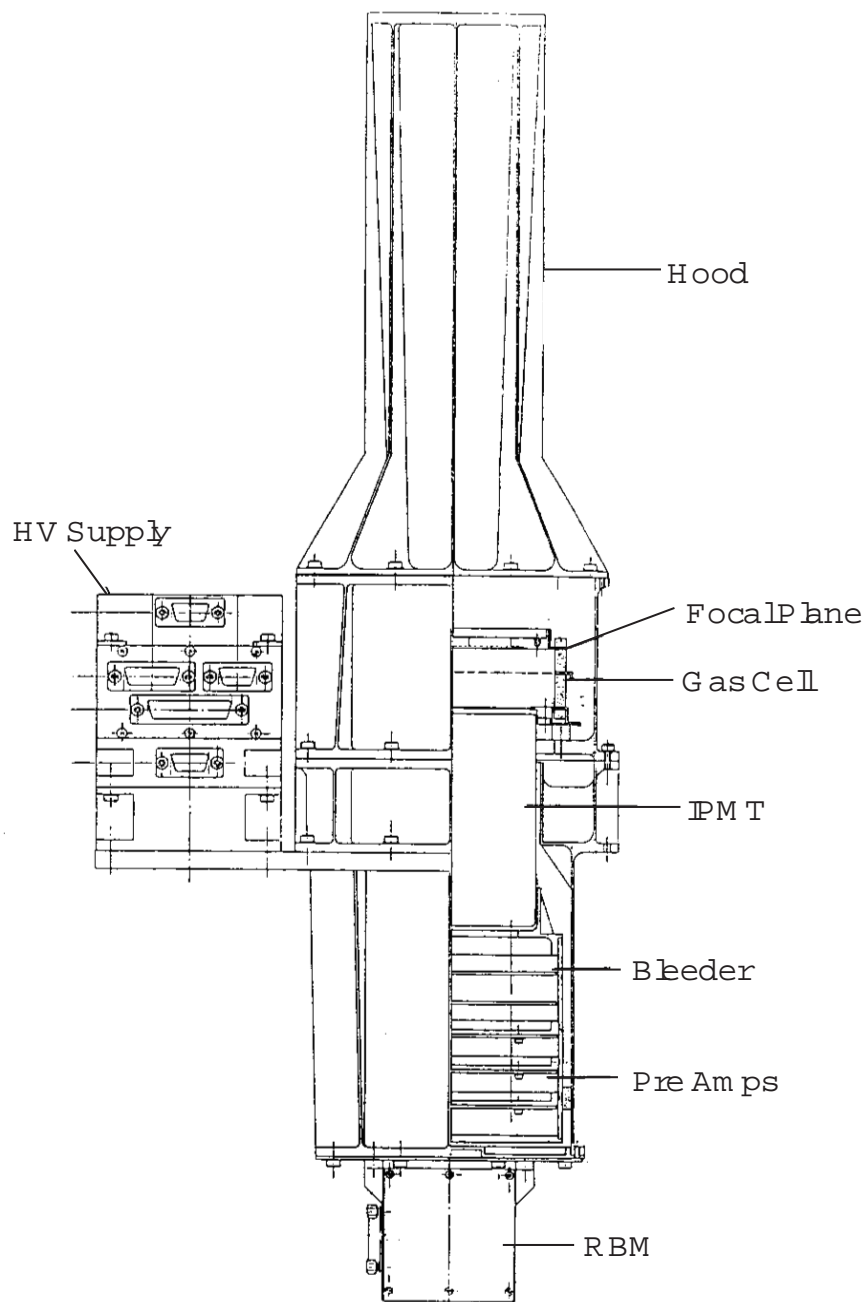


Figure 2.14: Cross sectional view of GIS. The full length of GIS2 is 58 cm.

distribute within $\sim 2\mu s$, which corresponds to a time for an electron cloud to run through the scintillation region. This property of the dynode output plays an important roll for background rejection described in §2.4.4.

The detection efficiency of GIS for low energy X-rays is determined by the thickness of the Be window, the plasma shield, and the thermal shield of XRT, because low energy X-rays are significantly absorbed by these materials. For high energy X-rays the stopping power of Xe gas limits the detection efficiency. Figure 2.15 shows energy dependence of the detection efficiency of GIS. The energy resolution of GIS is given as:

$$\left(\frac{\Delta E}{E}\right)^2 = \frac{2.355^2}{N} \left(F + \frac{1}{L} \left(1 + \frac{1-\gamma}{\gamma} + \frac{1}{\gamma} \frac{2f_p}{\delta-1} \right) \right),$$

where N is the number of electrons in the electron clouds, L is the number of fluorescent photons created by a single electron, γ is the quantum efficiency at the photo-electrode of IPMT, $\delta (\simeq 2.8)$ is an amplification factor per dynode of IPMT, $F (\simeq 0.2)$ is the Fano factor of the gas, and $f_p (\simeq 0.5)$ is the Fano factor in IPMT. The energy resolution is about 8% at 5.9 keV and is inversely proportional to the square root of the energy of an incident X-ray as shown in Figure 2.15.

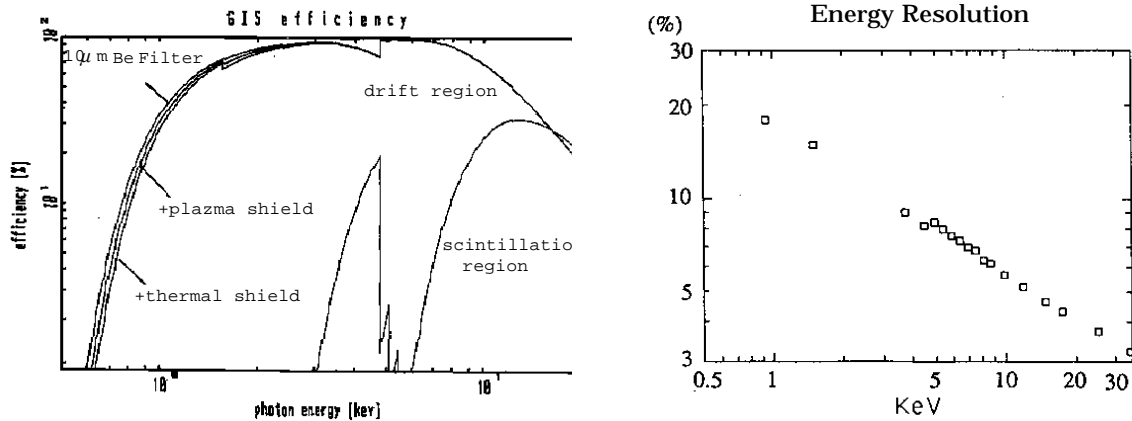


Figure 2.15: (left panel) Detection efficiency of GIS. The L-edge of Xe (4.7 keV) is clearly seen in the figure. (right panel) Energy resolution of GIS as a function of incident energy.

2.4.3 On-Board Data Processing

Data processing at GIS-E depends on the operation modes of GIS; it has three observation modes and a GIS memory check mode. The observation modes are designed for scientific observations and consists of PH normal mode (PH mode in short), PH PCAL mode (PCAL mode in short), and MPC mode. In PH mode X-ray images and spectra are

simultaneously obtained with high time resolution up to $61\mu s$. The GIS memory check mode is used to check the memory for the CPU in GIS-E. In this mode the contents of two 32KB RAM are dumped and sent to a ground station to be checked. All the data processing for GIS data depends on the bit rate (see §2.6 for explanation).

Electric signals from IPMT are of two types: signals from 16×2 anodes from which X-ray positions are calculated and signals from a dynode whose pulse height and rise time are measured. They are fed to preamplifiers after 32 signals from the anodes are multiplexed into four groups of signals. Output signals from the preamplifier are sent to GIS-E. Their pulse heights are converted into digital signals with 8 bits flash ADC. GIS-E also measures the pulse height and the rise time of a signal from the dynode with 12 bits ADC. GIS events are discriminated with their pulse heights and the rise times. Scalers in GIS-E count up the number of events of each kind, which is called “monitor counts”, to monitor the behavior of GIS. Arrival times of X-rays are measured with scalars counting the system clock of the satellite (“time stamp” of the event). The frequency of the system clock depends on the bit rate: it is 16384 Hz for high bit rate, 2048 Hz for medium bit rate, and 512 Hz for low bit rate. In Table 2.7 the clock speed relating to time assignment of GIS are listed. In the table maximum counting rates observable with GIS are also listed.

Table 2.7: Clock speed relating to time assignment of GIS

Bit Rate ^{a)}	Time stamp		Telemetry output ^{b)}		Maximum Counting Rate ^{c)}
	Frequency	Period	Frequency	Period	
High	16384 Hz	$\sim 61 \mu s$	256 Hz	$\sim 4 \text{ ms}$	256 c/s
Med	2048 Hz	$\sim 488 \mu s$	32 Hz	31.25 ms	32 c/s
Low	512 Hz	$\sim 1.95 \text{ ms}$	4 Hz	125 ms	8 c/s

a) See §2.6 for explanation.

b) T_{tlm} in Figure 2.16.

c) For GIS2 + GIS3.

In PH mode digital signals such as pulse heights are collected by two CPU’s (80C286) in GIS-E. Positions of incident X-rays are calculated from pulse heights of 32 anode signals by fitting a pulse height distribution on each axis with a Lorentzian (Fast Lorentzian Fit; FLF). The width of the Lorentzian is called the “spread” of the scintillation light and is used to eliminate non-X-ray background events (see §2.4.3 for details). One GIS event occupies 32 bits in a telemetry format (see §2.6). Table 2.8 shows the arrangement of a GIS event in the 32 bits; sensor ID, a pulse height, a position, a rise time, a spread and a

time stamp of the event are packed. The length of each component can be changed by a command from a ground station (see also §2.6). The possible length of each component is shown in Table 2.8. If the length of a certain component is specified to be n , n bits from the most significant bit (MSB) of the component are picked up and packed into the telemetry format.

Table 2.8: Summary of bit assignment of GIS PH mode

Sensor ID	Pulse Height	X Position	Y Position	Rise Time	Spread	Arrival Time
ID	PH	XP	YP	RT	SP	TIM

Data	# of bits ^{a)}	Contents
ID	<u>1</u>	Sensor which detects the event (0:GIS2, 1:GIS3)
PH	8, <u>10</u>	Pulse height of dynode's output
XP	2,4,6, <u>8</u>	X-ray position on x-axis
YP	2,4,6, <u>8</u>	X-ray position on y-axis
RT	0, <u>5</u> ,6,8	Rise time of dynode's output
SP	<u>0</u> ,8	Spread of scintillation light
TIM ^{b)}	<u>0</u> ~ 10	Time stamp of the event

a) The numbers of bits underlined in the table are default values.

b) Determined as a remainder in assigning bits for others with 10 bits as its maximum.

The assignment of their lengths is called the “bit assignment” and is determined for each observation. The number of bits for the time stamp (hereafter “timing bits”) is the remainder after assigning bits for other components with 10 bits as its maximum. The bit assignment is indicated such as “10-8-8-5-0-0”, which means 10 bits for PH, 8 bits for XP, 8 bits for YP, 5 bits for RT, 0 bit for SP, and 0 bit for TIM in Table 2.8.

2.4.4 Fundamental Reduction of GIS data

To take the best advantage of GIS, a few fundamental data reductions are introduced in a standard analysis. In this section we summarize the methods of these standard data reductions and introduce how they are efficient for the GIS capabilities.

Estimation of Photon Arrival Time

A time sequence of an X-ray detection by GIS is schematically drawn in Figure 2.16. When an X-ray is detected at t_{arr} , a flag is asserted by GIS-E. The CPU in GIS-E detects this flag and starts the on-board data processing described above. This procedure takes $T_{CPU} \sim 8\text{ms}$ for an event. After the process the CPU puts the set of data for that event into FIFO. In addition, the CPU picks up a set of event data from FIFO and sends it to DP at t_{tlm} every T_{tlm} as triggered by a “telemetry clock”. The event therefore waits in FIFO for a certain time T_{FIFO} . If n events are filled in FIFO when an X-ray event is detected, the event waits for another $n \times T_{tlm}$ to be sent to DP. The interval T_{tlm} in Figure 2.16 depends on the bit rate (see §2.6 for explanation) as listed in Table 2.7. T_{arr} in Figure 2.16 is the time interval between an X-ray detection and the latest telemetry output timing.

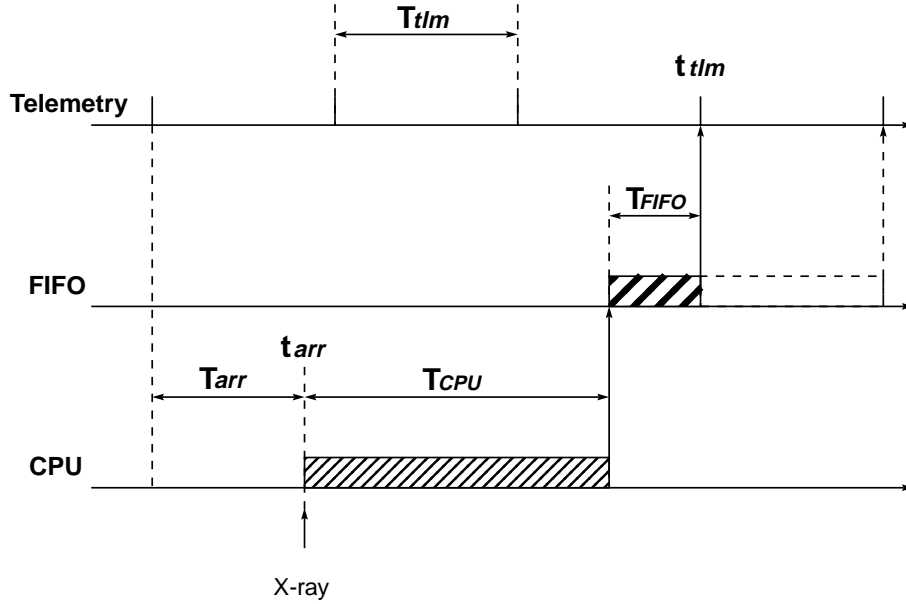


Figure 2.16: Time sequence of an X-ray detection by GIS.

The UTC (Universal Coordinated Time) time t_{tlm} of an event is known since the telemetry clock is calibrated to UTC through an atomic clock at the ground station at Kagoshima Space Center (KSC). Then t_{arr} is estimated from t_{tlm} with an ambiguity of $\pm 16m \times T_{tlm}$ (m is an integer), which corresponds to the time in which the scaler for the time stamp overflows. The ambiguity, however, is long enough for any observations except for those with extremely high counting rates, which causes a significant deadtime of CPU and an event may wait in the FIFO for much longer time than $16T_{tlm}$. Hence if the length of the timing bits is non-zero the ambiguity is negligible and the estimated t_{arr} is accurate enough for temporal analyses.

If length of the timing bits is set to zero there is no way to estimate t_{arr} from t_{tlm} . In temporal analyses t_{tlm} is used as the photon arrival time instead of t_{arr} . With simple manipulations, it is clear that t_{tlm} is delayed with respect to t_{arr} by a certain time T_{delay} ranging from $T_{CPU} + N_{FIFO}T_{tlm}$ to $T_{CPU} + (N_{FIFO} + 1)T_{tlm}$, where N_{FIFO} is the number of events presently occupying FIFO, depending on T_{arr} and the total counting rate of the observation. The relationship between T_{delay} and T_{arr} is illustrated in Figure 2.17 for the case that $N_{FIFO} = 0$. For observations with low counting rates $N_{FIFO} = 0$ for most events, then t_{delay} distributes from T_{CPU} to $T_{CPU} + T_{tlm}$ uniformly. As a result t_{delay} is estimated to be $T_{CPU} + T_{tlm}/2$ as an average with an uncertainty of T_{tlm} . For an observation with the timing bits set to 10, for example, $t_{delay} \simeq 10\text{ms}$ and its uncertainty is $\sim 4\text{ms}$. One should note that this discussion is only valid for observations with low counting rates.

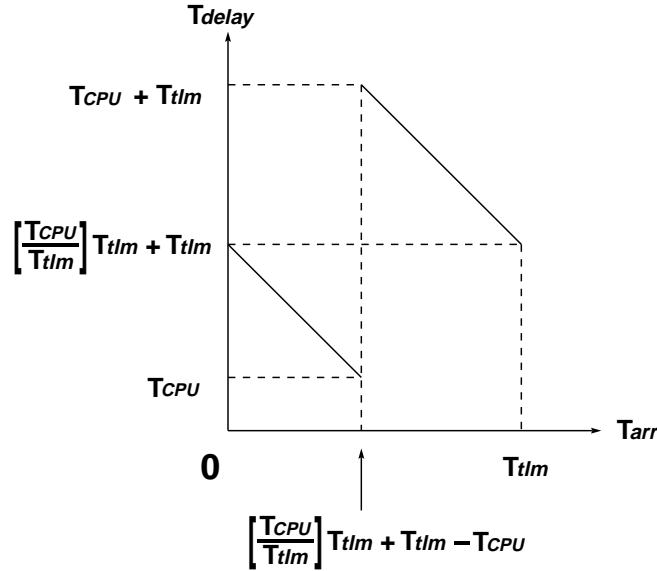


Figure 2.17: Relationship between T_{delay} and T_{arr} for $N_{FIFO} = 0$. See text and Figure 2.16 for definitions of symbols in the figure.

Gain Correction

The gain number of GIS mainly depends on the temperature of the gas cell and the position at which an X-ray is detected. The temperature dependence is due to characteristics of Xe gas in the gas cell. The positional dependence is caused by the positional dependence of the sensitivity of IPMT. On the surfaces of both GIS2 and GIS3 radioactive isotopes ^{55}Fe are mounted near the rim of their apertures. ^{55}Fe emits fluorescent X-rays of energy 5.895 keV. This X-ray line is used to measure the instantaneous gain number of GIS. The

imaging capability of GIS enables us to extract only events from the isotopes and events from the isotopes do not contaminate X-rays from celestial objects. Figure 2.18 shows the temperature dependence of the gain number. The figure shows that the gain number is correlated with temperature. Figure 2.19 shows the position dependence of the gain number normalized by the gain number at a certain position on the detector. The figure, called a “gain map”, is obtained from pre-flight calibrations on the ground and is revised by analyses of spectral lines when GIS images the bright earth in-flight.

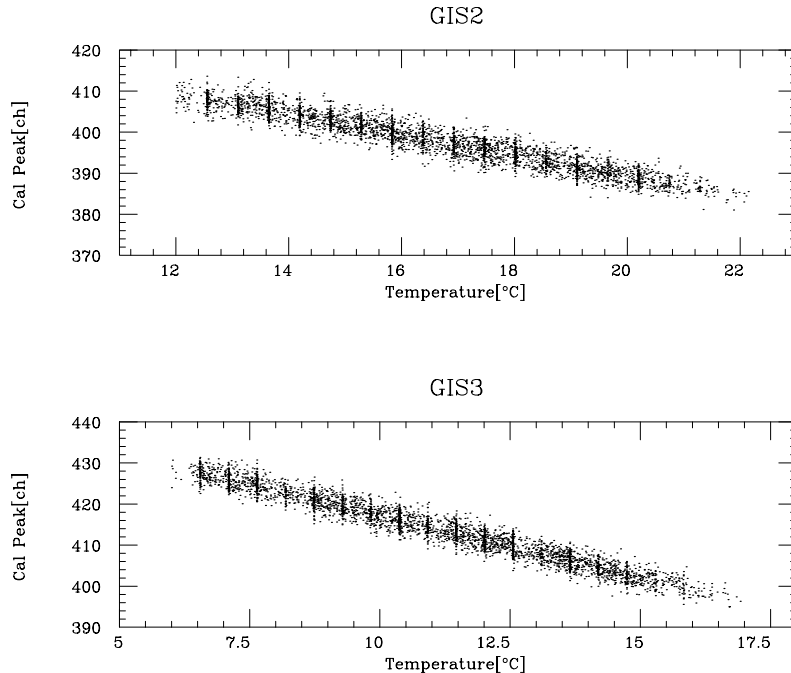


Figure 2.18: Temperature dependence of the gain number of GIS2 (upper panel) and GIS3 (lower panel). Centers of spectral peaks due to ^{55}Fe (5.895 keV) are plotted against gas temperature averaged over integration times of the spectra. In the figure thin vertical concentrations of data points are seen with a constant interval because temperature is monitored in units of 0.5° .

The gain correction for GIS events is divided into two steps. First, a pulse height of an event is corrected taking the gain map into account. After this correction the corrected gain number is constant all over the surface. Second, the resultant pulse height is further corrected so that X-rays from ^{55}Fe distribute centering on 500 ADU. This cancels the temperature dependence of the gain number and the corrected pulse height is independent of the observation conditions, called a pulse height invariant (PI). According to pre-flight and in-flight calibrations, the uncertainty in the GIS gain is known to be 1%.

The GIS gain has been monitored by the *ASCA* instrument team since the launch

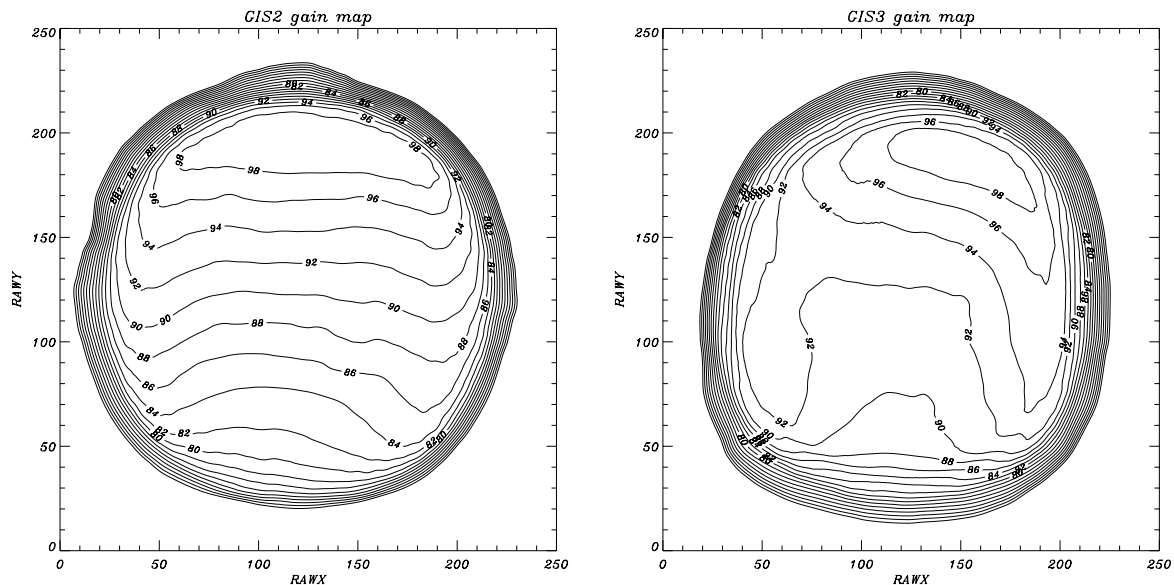


Figure 2.19: Positional dependence of the gain number of GIS2 (left panel) and GIS3 (right panel). Contours indicate the gain number at each position normalized by the gain number at a certain position on the detector.

because the gain reflects the condition of the Xe gas in the gas cell; the gain increases when the Xe gas leaks and decreases when the amount of impurities increases in the gas cell. According to the monitor, the gain at fixed temperature shows a secular decrease with time as shown in Figure 2.20. This may be because the quartz windows between the gas cell and IPMT are getting opaque gradually, as well as because the amount of impurities increases in the gas cell.

Background Rejection

Over 90% of background events can be rejected by means of evaluating a pulse height, a rise time, and the spread of the event. Sources of GIS background events are divided into three types as illustrated in Figure 2.21. Cases (a) is due to X-rays absorbed at abnormal positions in the gas cell and case (b) and (c) are due to charged particles or high energy γ -rays as described below.

In case (a) an X-ray is detected not in the drift region but in the scintillation region. These events have shorter rise time, since an electron cloud moves in the scintillation region shorter than in the case of normal events. Since they generate a smaller number of scintillation photons, they reduce the energy resolution of GIS. These events can be rejected by means of accepting events only with appropriate rise time (rise time discrimination). In case (b) an event is due to charged particles or high energy γ -rays. Charged

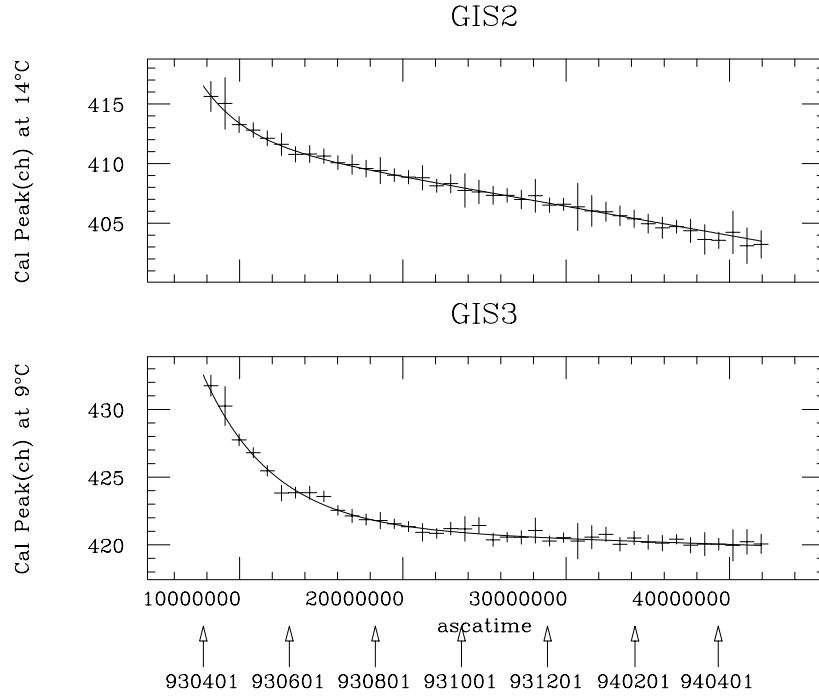


Figure 2.20: Secular trend of the gain number of GIS2 (upper panel) and GIS3 (lower panel). The vertical axis shows the center of the pulse height distribution due to fluorescent X-rays from ^{55}Fe (5.895 keV). The figure shows a secular decrease of the GIS gain.

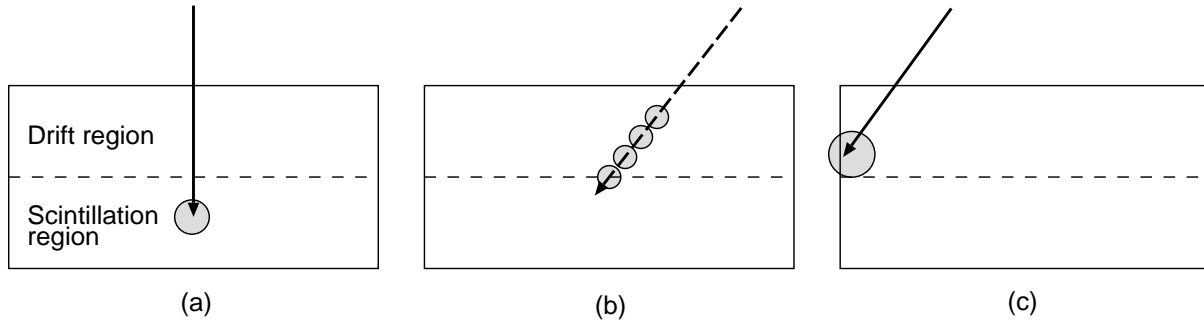


Figure 2.21: Three types of GIS background events. Cases (a) is due to X-rays absorbed at abnormal position in the gas cell. Case (b) and case (c) are due to charged particles and high energy γ -rays.

particles create electron clouds along their long tracks and multiple Compton scattering may take place for high energy γ -rays. Most of these events have larger pulse heights than an upper threshold for a pulse height and do not trigger the data acquisition system of GIS. The rest of these events can be rejected in the ground analyses because of large rise times due to largely spread electron clouds. Even if electron clouds align in a horizontal direction and result in a normal rise time, the large spread of the event enables us to re-

ject the event (spread discrimination). In case (c) an event is caused by charged particles or high energy γ -rays which interact with the side of the gas cell and create a cloud of primary electrons. The primary electrons spread wider than an electron cloud due to an X-ray and cause a large spread of the event. These events can be rejected by the spread discrimination.

Figure 2.22 shows the background rejection with rise time discrimination. The upper left panel shows an image of a point X-ray source (EXO 0748-676) without a rise time discrimination. Pulse heights and rise times of events are plotted in the upper right panel. In the figure the dense part with a rise time ~ 190 corresponds to events detected in the drift region (normal events) and others are background events. The lower left panel shows the same image but with a rise time discrimination. Pulse heights and rise times of events are plotted in the lower right panel. We can see that there are significantly fewer background events near the rim of GIS with the rise time discrimination. Only events with rise times between 159 and 218 (rise time window) are collected in the on-board data processing and are sent to the ground station. 92% of background events are rejected by filtering events with a narrower rise time window in the data analyses. Different rise time windows are set for events with different pulse heights. A table of rise time windows for various pulse heights is called an “RT mask”.

Figure 2.23 shows the background rejection with a spread of an event. The spread discrimination rejects 60% of background events not rejected by the rise time discrimination. The vertical axis is the spread of the event and the horizontal axis is the square of the radius of the position of the detection referred to the detector’s center. Only events within the dashed lines in the figure are collected in the on-board data processing and are sent to the ground station. The figure shows that the spread discrimination rejects most of background events near the side of the gas cell, most of which seem to be caused in case (c).

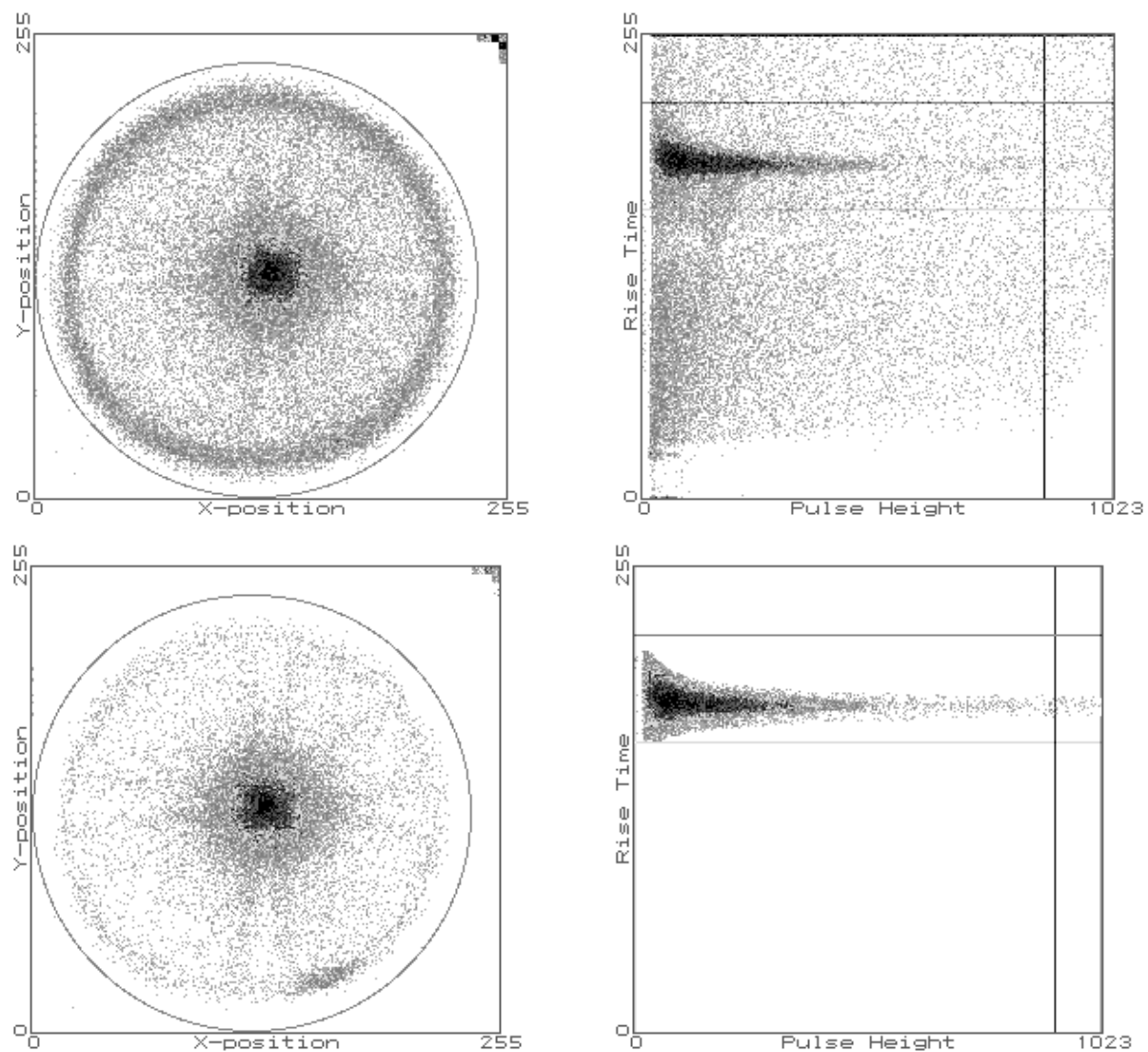


Figure 2.22: Background rejection with rise time discrimination. The upper left panel shows an image of a point X-ray source (EXO 0748-676) without a rise time discrimination. Pulse heights and rise times of events are plotted in the upper right panel. In the figure the dense part with a rise time ~ 190 corresponds to events detected in the drift region (normal events) and others are background events. The lower left panel shows the same image but with a rise time discrimination. Pulse heights and rise times of events are plotted in the lower right panel.

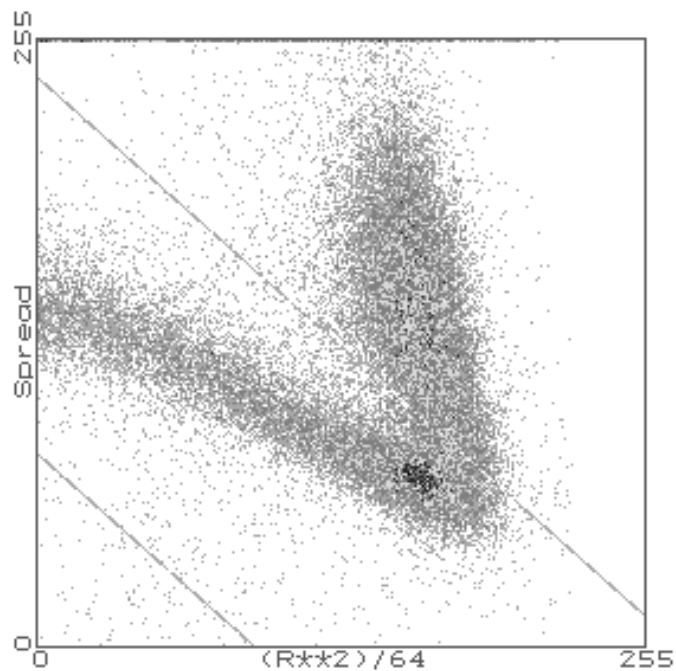


Figure 2.23: Background rejection with a spread discrimination. The vertical axis is the spread of the event and the horizontal axis is the square of the radius of the position of the detection referred to the detector's center. Only events within the dashed lines in the figure are collected in the on-board data processing and are sent to the ground station.

2.5 Alignment of the Detectors

The optical axes of the four XRT's point to slightly different positions on the sky. Also, the centers of the two SIS's and two GIS's correspond to different positions on the sky. This gives different effective areas to different detectors. The relationships between these positions are measured by the *ASCA* calibration team and are used to evaluate the detector's response in analyses. The relationships are shown in Figure 2.24. The positions of the optical axes and detector centers in reference to the center of SIS0 are projected on the focal plane in the figure. The figure also shows “nominal positions” for various observation modes, where an image of the target of an observation is planned to be placed. In 1-CCD mode, for example, the satellite's attitude is controlled so that an image of the target centers on the 1-CCD nominal position on the detectors.

2.6 Data Transfer

All data acquired on-board are arranged in a “frame” following a telemetry format by a common data processor (DP). The frame consists of 128 “words”, each of which consists of 8 bits. It is divided into three parts: SIS data, GIS data, and house keeping data. 64 frames are treated as the largest unit of the data and are called a “super frame”. The structure of the super frame is illustrated in Figure 2.25.

Data are stored into a bubble data recorder (BDR). The capacity of BDR is 134,217,728 bits (= 2048 super frames). In order to avoid an overflow of BDR a recording rate of the data, called a “bit rate”, can be chosen from three rates: 2^{15} bits per seconds (high bit rate), 2^{12} bits per seconds (medium bit rate), and 2^{10} bits per seconds (low bit rate). BDR can record the data for 1 hour 8 minutes 16 seconds in high bit rate, for 9 hour 6 minutes 8 seconds in medium bit rate, and for 36 hour 24 minutes 32 seconds in low bit rate. Lengths of components of a super frame in a unit of time are listed in Table 2.9.

Table 2.9: Lengths of components of a super frame in a unit of time

Bit rate	Word	Frame	Super Frame
Low	7.813 ms	1.0 sec	64.0 sec
Medium	1.953 ms	250.0 ms	16.0 sec
High	244.14 μ s	31.25 ms	2.0 sec

Stored data is reproduced in 8 minutes 32 seconds and sent to a ground station at radio frequencies. The ground stations which receive *ASCA* data are at the Kagoshima Space

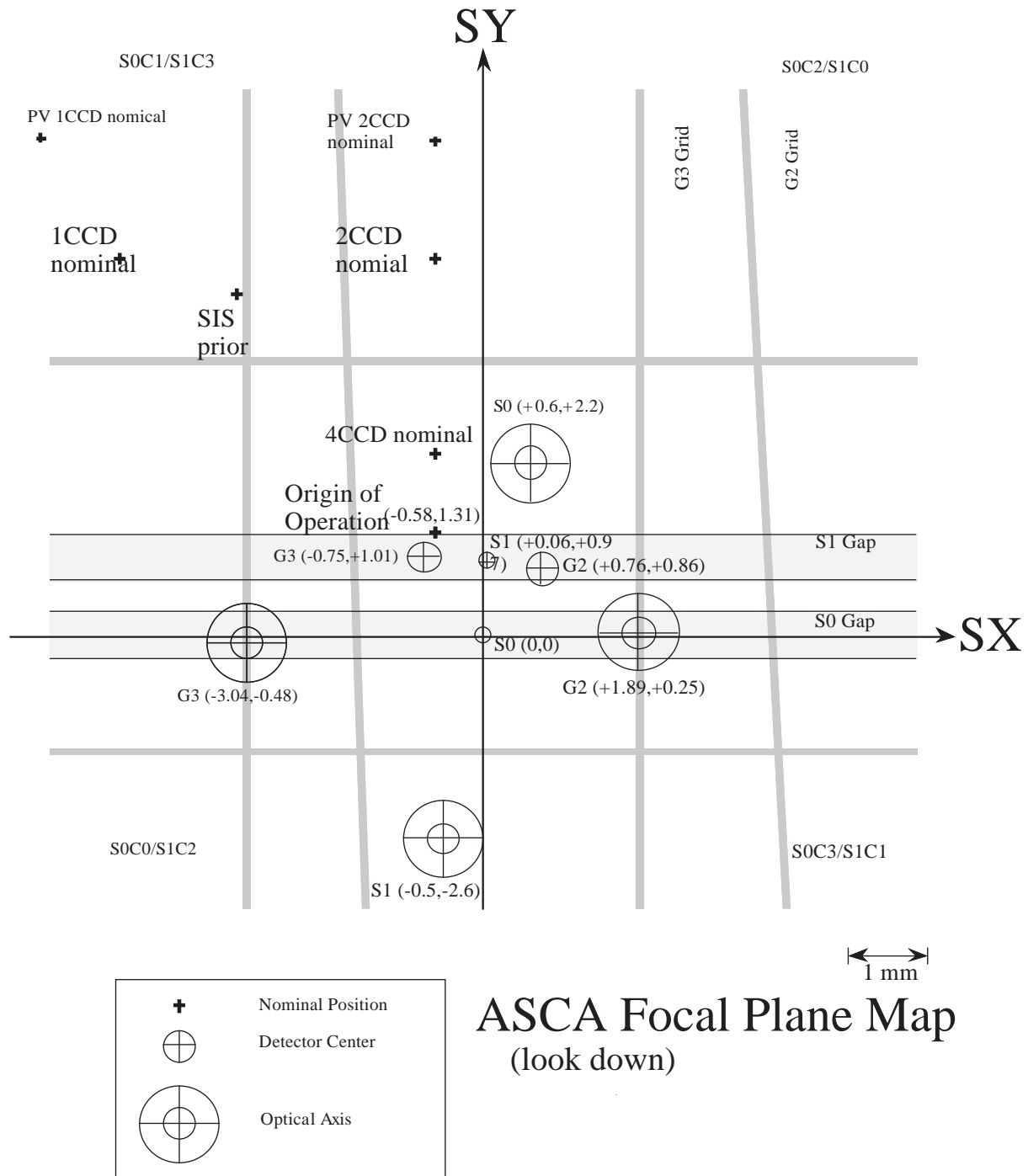


Figure 2.24: Alignment of the detectors. The optical axes and detector centers of SIS0, SIS1, GIS2, and GIS3 are shown. Nominal positions for various observation modes are also plotted in the figure.

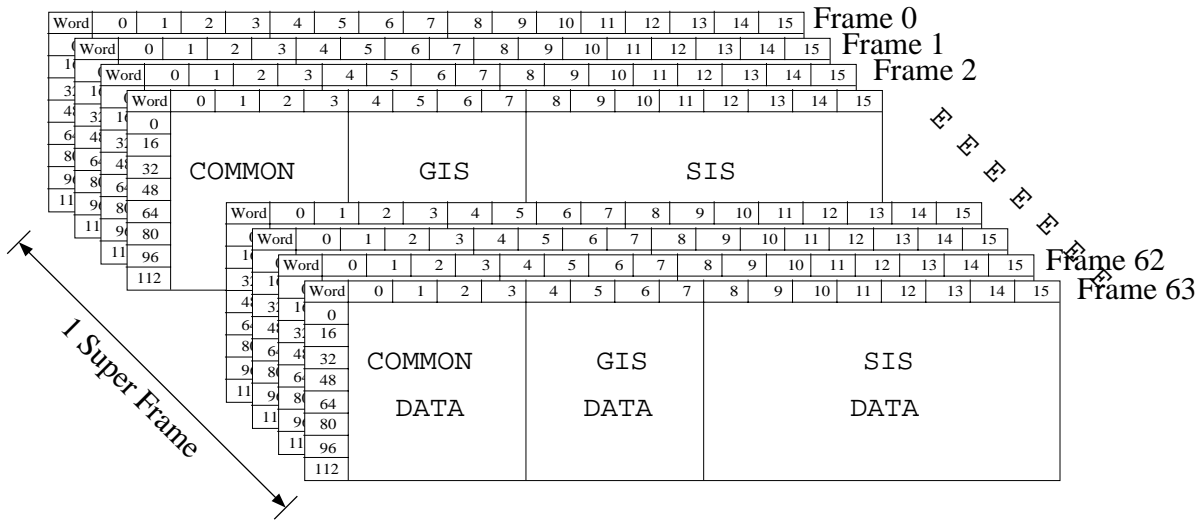


Figure 2.25: Structure of the telemetry format. One super frame consists of 64 frames which consists of 128 words = 1024 bits. A frame is divided into three, each of which includes SIS data, GIS data, and common data indicating the satellite's status.

Center (KSC) of ISAS. The Deep Space Network (DSN) stations by NASA also receive *ASCA* data. Data received at the KSC station and the DSN stations are transferred to the Sagami-hara Space Operation Center (SSOC) of ISAS and stored in a data base. The data is supplied to observers after reformatting and simple reduction.

2.7 Satellite Operation

A command plan is sent from the KSC station to the satellite once a day. The satellite observes celestial objects following the command plan including a schedule of observations, bit rates scheduling, operation modes of SIS and GIS for each observations, and so on. Usually the command plan is prepared by duty scientists at SSOC the day before. Duty scientists at KSC check the plan and send it to the satellite.

The attitude of the satellite is monitored by an inertial reference unit (IRU), two star trackers (STT), a non-spinning solar aspect sensor (NSAS), a spinning solar aspect sensor (SSAS), and a geomagnetic aspect sensor (GAS). In normal observations IRU and STT's detect the attitude in reference to celestial objects and offer information on the attitude to an attitude control system described below.

IRU consists of five gyroscopes facing in different directions and detects the angular momentum of the satellite. Its accuracy in determining the relative attitude of the satellite is up to 0.16", however, the attitude with respect to celestial objects can not be obtained only from IRU. STT is a CCD camera tracking bright stars and detects the

satellite's attitude in reference to celestial objects within an accuracy of $0.3'$. Information on tracking stars is transferred to the ground station through DP and is used to estimate the satellite's attitude against celestial objects in analyses on the ground. STT also offers information on the attitude to IRU and contributes to the correction of a small drift of the attitude due to a mechanical drift of IRU. NSAS is a two dimensional solar aspect sensor with angular resolution of $1.5'$. NSAS consists of two linear CCD's each of which detects the angle between the direction of the sun and one axis of the satellite. SSAS is also a solar aspect sensor with angular resolution of 1° . NSAS consists of a photo-diode with a narrow slit in its aperture and detects the direction of the sun using the spin of the satellite. GAS measures three orthogonal components of the geomagnetism and determines the attitude with respect to the geomagnetism with an accuracy of about 1° .

In order to point to a target of an observation, the satellite uses an attitude control system. The system consists of four reaction wheels (RW) and a three-axis magnetic torquer (MTQ). By exchanging angular momenta between RW's and the satellite, the satellite changes a pointing direction with total angular momentum conserved. MTQ interacts with the geomagnetism and gains or loses total angular momentum of the satellite to cancel the torque of the external force by the residual atmosphere.

Chapter 3

Observation

3.1 ASCA Observations of the System

The PSR B1259–63/SS 2883 system was observed with the *ASCA* satellite at six different orbital positions (hereafter obs1, obs2, obs3, obs4, obs5, and obs6). In Figure 1.4 we provide a schematic drawing of the pulsar’s orbit around the systemic center of mass, together with the approximate location of the pulsar during the *ASCA* observations and preceding X-ray observations reported by Cominsky et al. (1994) and Greiner et al. (1995). Also, Table 3.1 gives a summary of the six *ASCA* observations and of the orbital geometry for an assumed Be star mass $M_c = 10 M_\odot$.

Table 3.1: Geometry of the PSR B1259–63/SS 2883 system near *ASCA* observations

Observation	Date	MJD	ϕ ^{a)}	$s(10^{12} \text{ cm})$ ^{b)}	s/R_\odot
obs1	Dec. 28, 1993	49349	-75°	15	216
obs2	Jan. 10, 1994	49362	8°	10	144
obs3	Jan. 26, 1994	49378	90°	18	264
obs4	Feb. 28, 1994	49411	127°	39	552
obs5	Feb. 7, 1995	49755	170°	130	1860
obs6	Aug. 13, 1995	49942	178°	140	2040

a) True anomaly $\phi = 0$ at periastron.

b) Binary separation for assumed Be star and pulsar masses of $M_c=10 M_\odot$ and $M_p=1.4 M_\odot$.

The first three observations (obs1, obs2, and obs3) were performed about two weeks before, during, and about two weeks after the periastron passage of the pulsar near the beginning of 1994, as a part of a multi-wavelength campaign organized for the perias-

tron passage. These were the first opportunity for the system to be observed near the periastron in a high energy band. The *ASCA* TOO (Target Of Opportunity) observation (obs4) was assigned by the *ASCA* team when the radio pulsations reappeared after the periastron passage (see also §1.3). This observation was designed aiming detection of X-ray pulsation involved with radio pulse emission as seen in Crab-like pulsars. Another two observations (obs5, obs6) were made when the pulsar was approaching the apastron of the system. Through these observations we could measure the X-ray flux and obtain spectral information more precisely than *ROSAT* observations performed at nearly the same orbital positions during the previous apastron approach.

For all six observations two SIS were operated in 1-CCD faint mode with a time resolution of 4 s. Two GIS were in PH mode with higher time resolution, high enough to potentially study 48 ms pulsations from PSR B1259–63. The bit assignment of GIS data for each observation is listed in Table 3.2. The time resolution of GIS data is also listed in the table.

Table 3.2: Bit assignment of GIS for each observation

Observation	Bit Assignment		Time Resolution	
	High bit rate	Medium bit rate	High bit rate	Medium bit rate
obs1	8-6-6-5-0-6	8-6-6-0-0-10	~ 0.98 ms	~ 0.49 ms
obs2	8-6-6-5-0-6	8-6-6-0-0-10	~ 0.98 ms	~ 0.49 ms
obs3	8-6-6-5-0-6	8-6-6-0-0-10	~ 0.98 ms	~ 0.49 ms
obs4	8-6-6-5-0-6	8-6-6-0-0-10	~ 0.98 ms	~ 2.0 ms ^{a)}
obs5	8-6-6-0-0-10	8-6-6-0-0-10	~ 0.061 ms	~ 0.49 ms
obs6	10-8-8-5-0-0	10-8-8-5-0-0	~ 3.9 ms	31.25 ms

a) Due to temporal radiation damage on GIS on-board memory. See text for details.

We had a few troubles with the satellite operation during our observations. Some made parts of the data unavailable and others reduced the time resolution of GIS data. The troubles are summarized below along with their influences on our data analyses.

SIS operated in 4-CCD mode (obs4)

At the beginning of obs4 SIS was operated in 4-CCD mode although the observation was originally planned in 1-CCD mode. The cause of this trouble was an error in the command plan (see §2.7). The data obtained in 4-CCD mode suffers from different observation conditions such as a larger number of hot/flickering pixels (see §2.3.4) due to the longer exposure time. In order to keep the conditions constant through

all six observations we discarded the SIS data obtained in 4-CCD mode. Less than one fourth of SIS data was lost.

Partial loss of GIS spectral and temporal information (obs4)

Due to damage on the on-board memory of GIS by charged particles, three bits from LSB (Least Significant Bit) of the pulse height data and two bits from LSB of the timing data were not available for two months including the observation period of obs4 . Because the bit assignment of GIS for obs4 was 8-6-6-5-0-6 for high bit rate and 8-6-6-0-0-10 for medium bit rate, only 1 bit of pulse height data was lost for our observation. In the data analyses described in §4.3 we avoided this problem by summing more than two neighboring pulse height bins. The loss of the number of available timing bits reduces the effective time resolution of the GIS data by a factor of 4, *i.e.*, from ~ 0.49 ms to ~ 2.0 ms.

This trouble had no influence and resulted in no data loss for the SIS data. In addition, no other observations in this thesis suffered from this problem, since the damage on the memory was completely recovered by special efforts by the *ASCA* GIS team members.

No timing bit throughout an observation (obs6)

Throughout obs6 the GIS bit assignment was 10-8-8-5-0-0 instead of the planned 8-6-6-0-0-10. This reduced the time resolution of GIS to 3.9 ms in high bit rate and 31.25ms in medium bit rate. Since the expected pulse period of PSR B1259–63 is about 48 ms, only data obtained with the high bit rate was available to search for pulsations. In our data analyses data obtained in medium and low bit rates were discarded for the pulsation search and about one third of GIS data was lost by this procedure.

This trouble had no influence and resulted in no data loss for the SIS data and the spectral analysis with GIS data.

3.2 Satellite's Attitude during Observations

Pointing directions of the *ASCA* XRT during the observations were designed for PSR B1259–63 to be observed at 1-CCD nominal position (see §2.5 for explanation). Figure 3.1 shows the fields of view (hereafter FOV) of SIS0 and GIS2 at six observations. In the figure, SIS0 FOV of each observation is indicated as four neighboring squares, GIS2 FOV of each observation is indicated as a circle, and the vertical cross indicates the position of PSR B1259–63 in the sky; SIS1 and GIS3 FOV's are identical. The first five observations

were performed with almost the same attitude but obs6 was made with the roll angle reversed in order to expose the solar paddles to the Sun. From Figure 3.1 we can see PSR B1259–63 well in the nominal chip in all six observations, the best-calibrated chip in SIS0 which is used for observations of point sources.

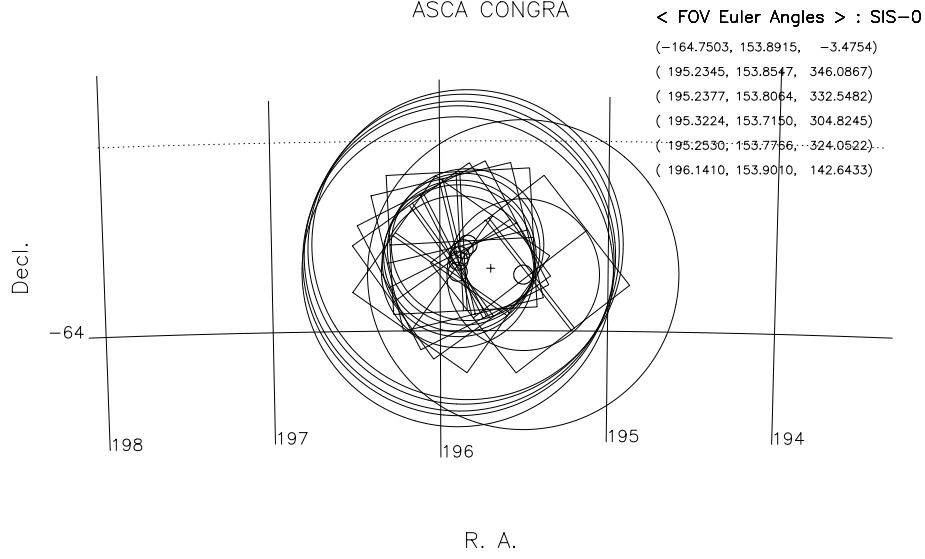


Figure 3.1: Fields of view of SIS0 and GIS2 at six observations. In the figure, SIS FOV of each observation is indicated as four neighboring squares, GIS FOV of each observation is indicated as a circle, and the vertical cross indicates the position of PSR B1259–63 in the sky.

The actual attitudes of the satellite during observations are monitored by the ACS system described in §2.7. Figure 3.2 shows results from attitude determinations for all the observations. In the figure the pointing directions are plotted against ASCATIME, seconds elapsed since $0^{\text{h}} 0^{\text{m}} 0^{\text{s}}$ on January 1 in 1993 (UTC). The upper left panel corresponds to obs1, upper right to obs2, middle left to obs3, middle right to obs4, lower left to obs5, and lower right to obs6. In each of the six panels the upper plot shows the right ascension of the satellite Z-axis, the middle plot shows the declination of the satellite Z-axis, and the lower plot shows the third Euler angle of the satellite. From the figure, we can see that the attitudes during all the observations were stable to well less than $\sim 1'$ of the *ASCA* pointing accuracy, although we can see fluctuations in the attitude due to thermal distortion of EOB (see §2.1 for explanation) in the figure. Though fluctuation in satellite's attitude may increase the uncertainty in the estimation of the angular response of XRT, the fluctuations seen in Figure 3.1 are negligible in the analyses described later

in this thesis.

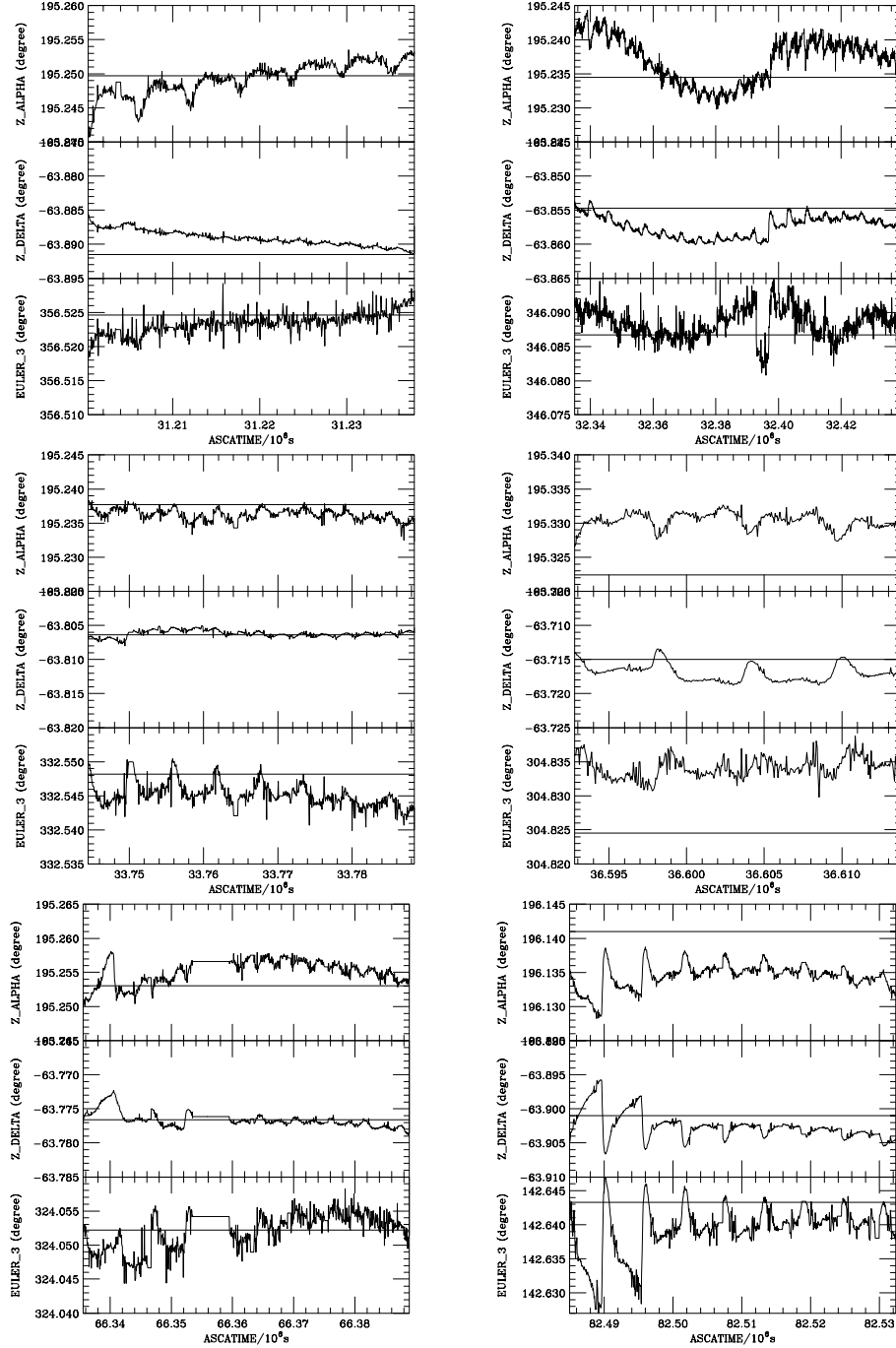


Figure 3.2: Actual attitudes of the satellite during the six observations by *ASCA*. In the figure pointing directions are plotted against ASCATIME, seconds elapsed since $0^{\text{h}} 0^{\text{m}} 0^{\text{s}}$ on January 1 in 1993 (UTC). The upper left panel corresponds to obs1, upper right to obs2, middle left to obs3, middle right to obs4, lower left to obs5, and lower right to obs6. In each of the six panels the upper plot shows the right ascension of the satellite Z-axis, the middle plot shows the declination of the satellite Z-axis, and the lower plot shows the third Euler angle of the satellite. Horizontal lines in figures indicate planned attitudes with which *ASCA* FOV lies as in Figure 3.1

Chapter 4

Analysis and Results

4.1 Data Reduction

The X-ray data were reduced with standard sets of analysis tools, including XANADU and FTOOLS packages supplied by the *ASCA* Guest Observer Facility (GOF) at the Goddard Space Flight Center (GSFC) and at the Institute of Space and Astronautical Science (ISAS). In the spectral analysis we also used a program “jbldarf” supplied by the *ASCA* calibration team to calculate XRT effective areas of our observations taking into account the detector’s responses. In the temporal analysis we utilized our original programs developed on the *ASCA*_ANL package, which we have been developing as a platform for flexible analysis of *ASCA* data. In these programs, however, the GOF-supplied routines were used for temporal corrections, such as the conversion of arrival times of photons to those at the solar system barycenter, to keep consistency between results from GOF-supplied tools and ours.

Prior to all analyses described below we did standard data reductions for *ASCA* data analysis. That is, we used only data obtained when the satellite was passing in a region with a cut off rigidity (hereafter COR) ≥ 6 GeV/c for SIS, COR ≥ 8 GeV/c for GIS, and when the elevation angle of the pointing direction of the satellite measured from the rim of the earth (hereafter ELV) was greater than or equal to 5° commonly for SIS and GIS. Furthermore, we analyzed only SIS data taken when the elevation angle of the satellite’s pointing direction measured from the rim of the bright earth (hereafter ELV_D, which stands for “Day earth ELeVation angle”) was greater than or equal to 25° , and SIS events detected during 200 s after the satellite pointed at the bright earth were rejected (hereafter DNGAP). A program “selecter” coded by the *ASCA* calibration team surveyed the entire observing epochs and provided time intervals in which these conditions were satisfied. In Table 4.1 we summarize the selection criteria described here. In addition, the

satellite’s attitude during observations constrains the time interval for SIS and GIS data to be analyzed. For each observation one time interval was determined during which the satellite’s attitude was sufficiently stable. Figure 3.2 in §3.2 shows the satellite’s attitude in the time intervals determined in that way.

Table 4.1: Selection criteria for SIS and GIS data

Selection	SIS	GIS
COR ^{a)}	6 GeV/c	8 GeV/c
ELV ^{b)}	$\geq 5^\circ$	$\geq 5^\circ$
ELV_D ^{c)}	$\geq 25^\circ$	—
DNGAP ^{d)}	200 s	—
Bit rate	High & Medium	High & Medium

a) Cut off rigidity

b) Elevation angle of a pointing direction of the satellite measured from the rim of the earth

c) The same as a) but measured from the rim of the bright earth

d) Time after the satellite’s pointing direction crosses a rim of the bright earth from the bright earth to the night earth or blank sky.

For SIS data removal of hot/flickering pixels, DFE correction, removal of echo effect, and CTI corrections were performed (see also §2.3.4). DFE values were calculated with a GOF-supplied program “faintdfe”. Figure 4.1 shows DFE values for all the observations. Echo fractions calculated from observed data as described in §2.3.4 are listed in Table 4.2. A GOF-supplied CTI table was used for CTI correction mainly in order to cancel the difference in gain numbers between CCD chips, as well as to take into account the positional dependence of the pulse height due to CTI. SIS events were classified into eight grades as described in §2.3.4. We selected SIS events with grades 0, 2, 3, or 4 to reject background events mainly caused by charged particles.

Table 4.2: Echo fractions

Sensor	obs1	obs2	obs3	obs4	obs5	obs6
SIS0	1.79%	1.78%	1.80%	1.85%	1.92%	2.04%
SIS1	1.02%	1.01%	0.97%	1.07%	1.20%	1.12%

For GIS data the normal data processing described in §2.4.4, such as gain corrections and assignment of photon arrival times, were performed with programs “frfread” and

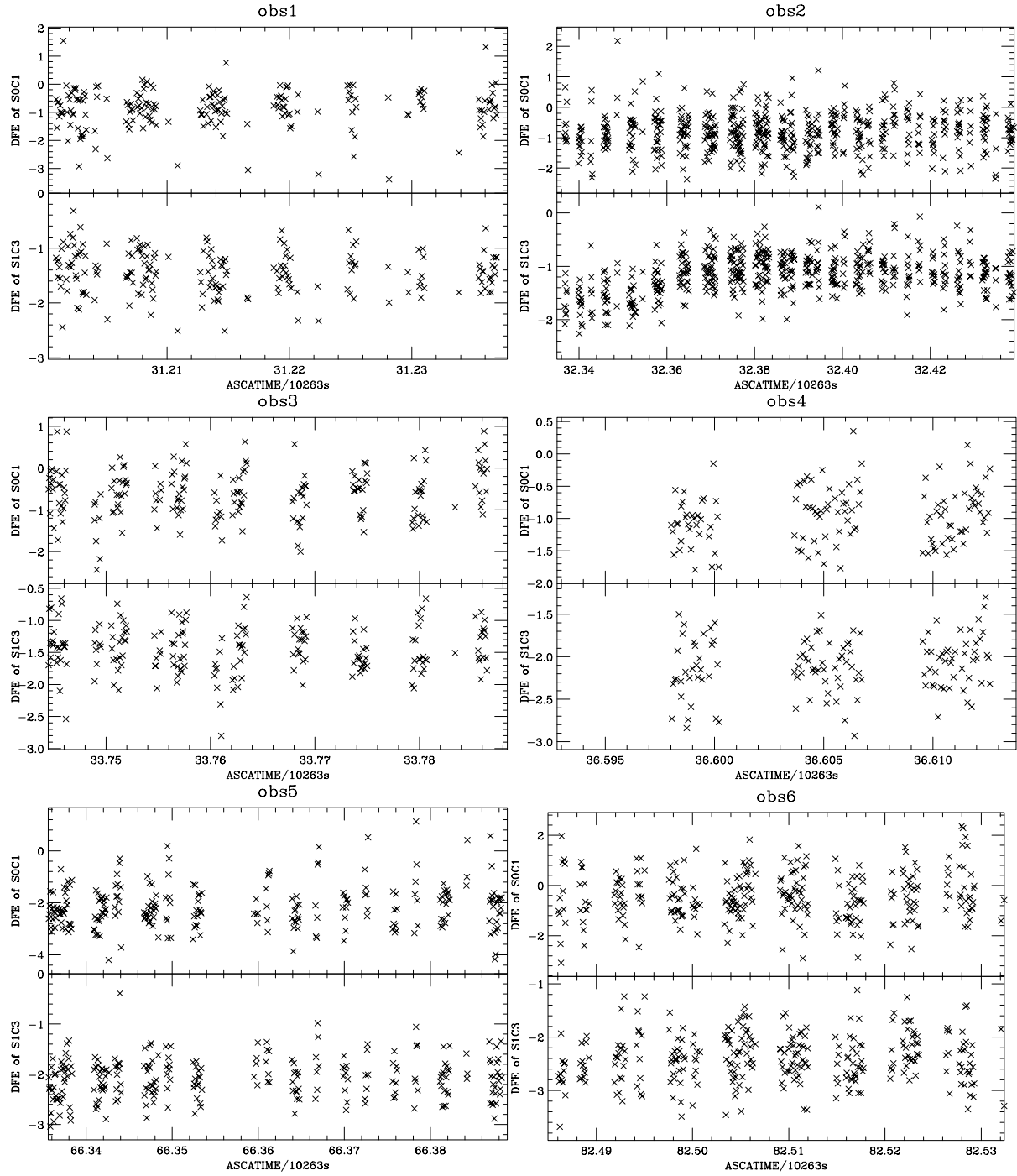


Figure 4.1: DFE values for the six observations are plotted against “ASCATIME”, seconds elapsed since $0^{\text{h}} 0^{\text{m}} 0^{\text{s}}$ on January 1 in 1993 (UTC), in units of ADU ($1 \text{ ADU} \sim 3.65 \text{ eV}$). Upper left panel shows DFE for obs1, upper right for obs2, middle left for obs3, middle right for obs4, lower left for obs5, and lower right for obs6, respectively. In each panel DFE of S0C1 is plotted in an upper part and DFE of S1C3 in a lower part.

“ascalin” in the FTOOLS package. In order to keep equivalent selection criteria for all the observations, we did not perform background rejection with “RT mask” (see §2.4.4

for explanation) since we had no rise time bit (see §2.8 for explanation) for some parts of the observations (see Table 3.2). Although lack of “RT mask” discrimination causes higher detection efficiency of GIS and also higher levels of background, we can cancel these effects in the following way. A program “gisnortarf”, supplied by the *ASCA* calibration team, was used to correct the detection efficiency of GIS for spectral analyses. Extra background was rejected by estimating the background from observed data as described in §4.3.1.

The net exposure times and source counts for the PSR B1259–63/SS 2883 system after the data selection are given in Table 4.3. Counting rates were calculated from source counts within 3' from X-ray positions of the system for SIS and 4' for GIS, both with background subtracted (see also §4.3.1).

Table 4.3: Net exposures and counting rates of *ASCA* observations

Interval	Net exposure (s)				Counting rate ^{a)} (cts s ⁻¹)			
	SIS0	SIS1	GIS2	GIS3	SIS0	SIS1	GIS2	GIS3
obs1	11721	11713	13122	13125	0.508 (8)	0.391 (7)	0.329 (5)	0.398 (6)
obs2	33106	33161	34602	34597	0.251 (4)	0.197 (4)	0.172 (2)	0.197 (3)
obs3	11048	11044	13894	13894	0.444 (8)	0.356 (7)	0.302 (5)	0.369 (5)
obs4	7834	7834	8975	8974	0.313 (8)	0.248 (6)	0.200 (5)	0.255 (6)
obs5	15127	15123	15033	15019	0.022 (3)	0.018 (2)	0.020 (2)	0.024 (2)
obs6	17739	17731	18844	18839	0.026 (3)	0.022 (2)	0.021 (2)	0.023 (2)

a) Calculated from source counts within 3' from X-ray positions of the PSR B1259–63/SS 2883 system for SIS, and 4' for GIS, both with background subtracted (see also §4.3.1). Numbers in parentheses in counting rates are 1σ statistical errors in last digit.

4.2 X-ray Image

At all six observed epochs, the PSR B1259–63/SS 2883 system was clearly detected with both SIS and GIS. SIS and GIS images for obs2 are shown in Figure 4.2. The brighter source seen in the GIS image is the system. The second source, some 10' south west of the pulsar, is unassociated X-ray source, and is not previously identified. The SIS image shows the signature of “four leaves shape” (like Figure 2.6) at the position of the pulsar, consistent with its identification as a point-source. The serendipitous source is in none of

the SIS images, as it lies outside the smaller SIS field of view. We do not consider the serendipitous source further in this thesis.

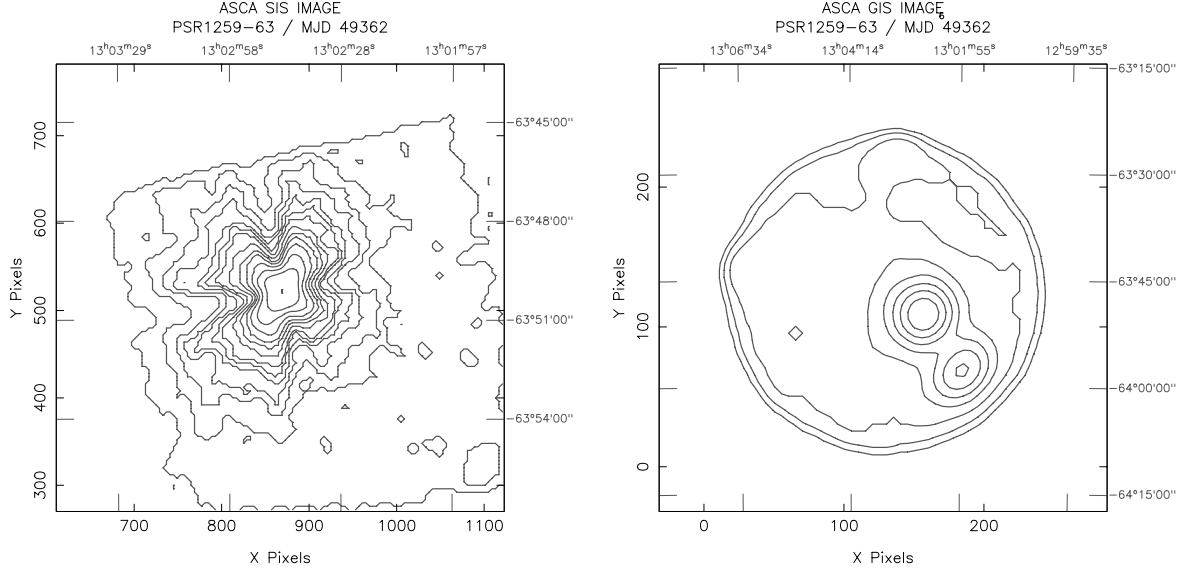


Figure 4.2: *ASCA* images of the PSR B1259–63/SS 2883 system for obs2. A logarithmic scale was used for these images. North is up and west is to the right for both images. (left panel) Image of the SIS0. A pixel is $0.026' \times 0.026'$. (right panel) Image of the GIS2. A pixel is $1' \times 1'$. The brighter source is the PSR B1259–63/SS 2883 system while the weaker source is a serendipitously discovered source unassociated with the PSR B1259–63/SS 2883 system. The weak enhancement seen in on east side of the image is due to the imperfectly removed *ASCA* calibration source.

The observed positions of the X-ray source were coincident with the position of PSR B1259–63 to within $1'$, the accuracy of the attitude determination of *ASCA* satellite (E. Gotthelf, private communication). The X-ray positions on the detectors were determined by fitting projections of X-ray images near the source onto X and Y axes of “detector coordinate” with a Gaussian function as a model function. The detector coordinates are defined individually on four sensors SIS0, SIS1, GIS2, and GIS3, with X and Y axes parallel to each other. One SIS channel corresponds to $\sim 0.026'$ in the sky and one GIS channel to $\sim 1'$ for obs1 to obs5 and $0.25'$ for obs6, respectively. Figure 4.3 shows the fit for obs2 as an example. X-ray positions determined in this way are listed in Table 4.4. In the table a lower row for each sensor shows the separation angles between the observed positions and the radio position by Manchester et al. (1995). The differences between the positions are due to the uncertainty in determining the satellite’s attitude and X-ray positions on detectors.

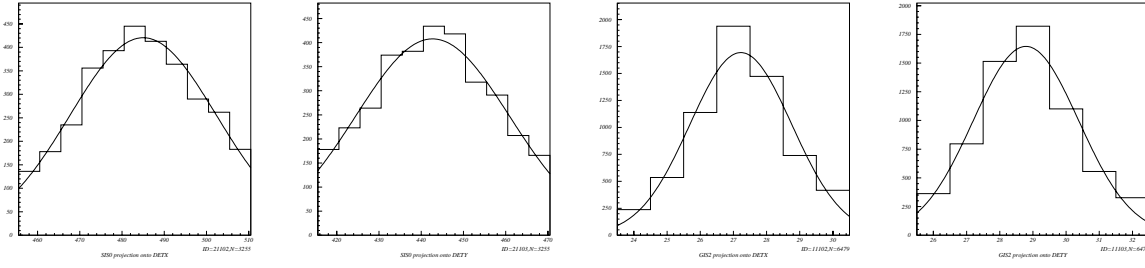


Figure 4.3: Determination of X-ray positions on detectors. The left two panels show the results of a Gaussian fitting to a projection of the SIS0 image onto X (left) and Y (right) axes of “detector coordinate” in units of channel. The right two show those of the GIS2 image. See the text for a brief explanation of the detector coordinate.

Table 4.4: Observed X-ray positions of the PSR B1259–63/SS 2883 system

Dataset	Position	SIS0	SIS1	GIS2	GIS3
obs1	$(x, y)^a$	(473, 447)	(472, 483)	(26.9, 28.9)	(29.6, 28.9)
	θ_{sep}^b	0' 20"	0' 21"	0' 30"	0' 56"
obs2	$(x, y)^a$	(485, 443)	(484, 478)	(27.2, 28.8)	(29.9, 28.8)
	θ_{sep}^b	0' 28"	0' 30"	0' 23"	1' 05"
obs3	$(x, y)^a$	(477, 460)	(476, 493)	(27.0, 29.1)	(29.7, 29.2)
	θ_{sep}^b	0' 15"	0' 19"	0' 30"	1' 08"
obs4	$(x, y)^a$	(476, 479)	(478, 516)	(27.2, 29.0)	(29.7, 29.8)
	θ_{sep}^b	0' 48"	0' 49"	1' 44"	1' 36"
obs5	$(x, y)^a$	(478, 449)	(477, 487)	(27.0, 29.9)	(29.8, 29.3)
	θ_{sep}^b	0' 23"	0' 21"	0' 29"	1' 18"
obs6	$(x, y)^a$	(486, 454)	(484, 487)	(110.7, 111.2)	(115.2, 112.1)
	θ_{sep}^b	1' 4"	1' 6"	1' 33"	1' 11"

a) X-ray positions on the detector expressed in detector coordinate in unit of channel.

b) Separation angles between observed positions and radio position by Manchester et al. (1995).

4.3 Spectral Analysis

Spectral analyses were done with the software packages XSPEC and the DISPLAY45. SIS0 and SIS1 data were summed into a single energy spectrum, and GIS2 and GIS3 data were also summed into another energy spectrum. For the spectral analyses described below photons within 3' for SIS and 4' for GIS from the position of the X-ray source (hereafter SRC region) were accumulated into a spectrum. In addition, photons were also

accumulated for background estimation (see §4.3.1 for background estimation) within a region arranged so that it did not include photons from the system (hereafter BGD region). Figure 4.4 shows the regions; we took identical regions for the other sensors in obs2 and for the other observations. X-rays within the hatched region in the figure were accumulated into a spectrum. In the left panel the circular region is the SRC region for SIS0 and the outer square region is the BGD region for SIS0. In the right panel the smaller circle is the SRC region for GIS2 and the larger circle is the BGD region for GIS2.

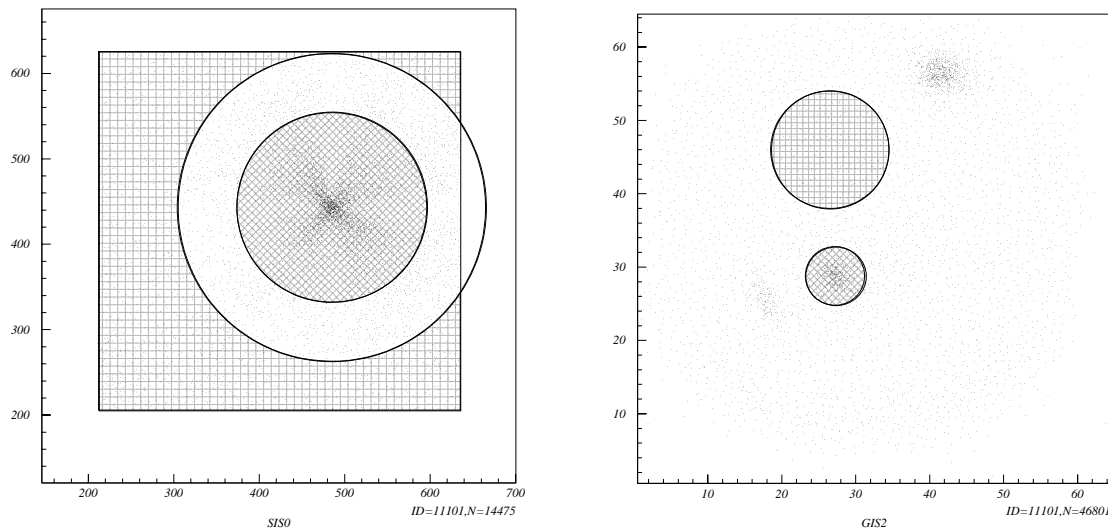


Figure 4.4: SRC and BGD regions for SIS0 (left) and GIS2 (right) superposed on X-ray images. X-rays within the hatched region were accumulated into a spectrum. In the left panel X-rays within a circular region (SRC region) were accumulated into an SIS0 spectrum from the system and X-rays within the outer square region (BGD region) into a spectrum for background estimation (see §4.3.1) of SIS0. In the right panel X-rays within the smaller circular region (SRC region) were accumulated into a GIS2 spectrum from the system and X-rays within the larger region (BGD region) into a spectrum for background estimation of GIS2.

After subtracting background spectra estimated in §4.3.1, the spectra were fitted with the detector’s response supplied by a combination of response matrices of SIS and GIS (stored in Response Matrix Files; hereafter RMF) and an effective area of XRT (stored in an Ancillary Response File; hereafter ARF). RMF for SIS and GIS are common for all six observations. Since SIS RMF depends on selection criteria of SIS data, RMF for our data selection were built with a program “sis_bldrsp2” by the *ASCA* calibration team. GIS RMF, supplied by the *ASCA* GOF in the calibration database, is available independent of the data reduction. ARF for SIS and GIS were created by “jbldarf” separately for the six observations, because the XRT effective areas depend on the observed X-ray positions.

The X-ray positions listed in Table 4.4 were used to create ARF in order to avoid influence of uncertainty in the satellite’s attitude determination.

The source fluxes detected in the apastron observations (obs5 and obs6) were so weak that the background spectrum was important, although it was negligible for the periastron observations (obs1, obs2, and obs3). Figure 4.5 compares the source spectra with the background spectra for obs2 and obs5. The upper two panels in the figure show SIS (left) and GIS (right) spectra for obs2 and the lower two for obs5. In each panel a spectrum in the SRC region is indicated by crosses with no background subtraction and a spectrum of “blank sky” in the same region is indicated by diamonds. The blank sky data is a superposition of 13 blank sky fields observed during the *ASCA* performance verification phase (from May 1993 to Nov 1993). The blank sky spectrum includes instrumental background, non-X-ray background due to charged particles, and the cosmic X-ray background. We can see that the background spectrum accounts for significant portion of the spectrum at obs5, though it is negligible at obs2.

4.3.1 X-rays from Galactic Plane as Background

In addition to the background included in the blank sky spectrum, the spectrum of the system is contaminated by X-rays from the Galactic plane because the position of the PSR B1259–63/SS 2883 system is near the Galactic plane ($b \sim -1^\circ$). Figure 4.6 shows the contribution. In the figure the spectrum in the BGD region is indicated for obs2 and the blank sky spectrum in the same region is indicated by diamonds. The contribution of the Galactic ridge emission lies between the two spectra in Figure 4.6. From the figure we can see the Galactic background can not be negligible.

The background spectrum behind the PSR B1259–63/SS 2883 system was estimated by correcting the observed spectrum in the BGD region to cancel the difference in accumulation regions. The observed spectra in the BGD region include the instrumental background, non X-ray background, the cosmic X-ray background, and the Galactic background. All of these background spectra slightly depend on where on the detector the accumulation region is. The dependence can be seen in Figure 4.7. In the figure the spectrum in the SRC region is indicated by crosses and that in the BGD region is indicated by diamonds. In order to cancel the same effect seen in the figure the observed spectra in the BGD region were multiplied by the ratio of two spectra in the figure; the spectrum of the Galactic background in the SRC region was estimated by

$$G^i = S_{\text{BGD}}^i \times \frac{B_{\text{SRC}}^i}{B_{\text{BGD}}^i} ,$$

where G^i is the number of photons in i -th bin of the estimated background spectrum,

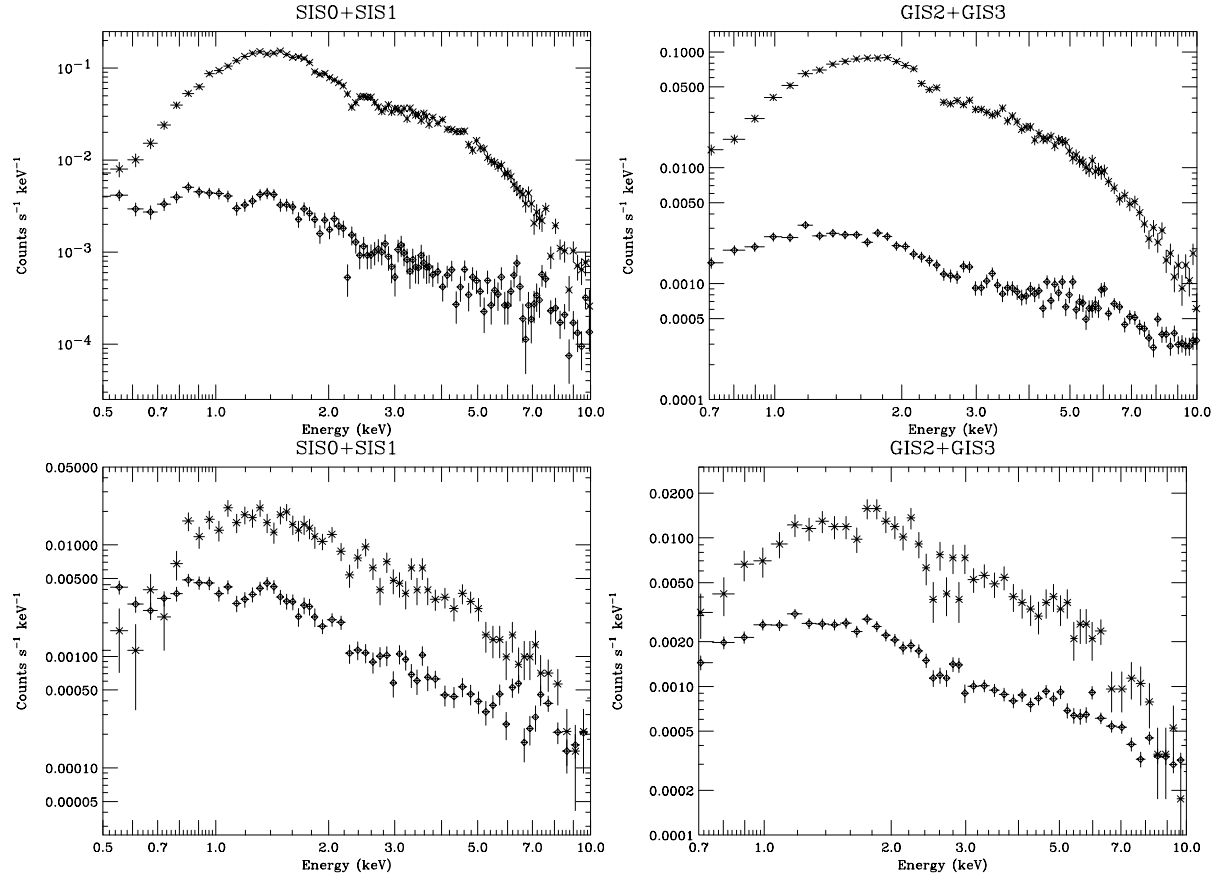


Figure 4.5: Comparison of source spectra with background spectra. The upper two panels in the figure show SIS (left) and GIS (right) spectra for obs2 and the lower two for obs5. In each panel a spectrum in the SRC region is indicated by crosses with no background subtraction and a spectrum of blank sky in the same region is indicated by diamonds.

S_{BGD}^i is that of the observed spectrum in the BGD region, B_{SRC}^i is that of the blank sky spectrum in the SRC region, and B_{BGD}^i is that of the blank sky spectrum in the BGD region. Hence the spectrum of X-rays from the system was evaluated by

$$\begin{aligned} N^i &= S_{\text{SRC}}^i - G^i \\ &= S_{\text{SRC}}^i - S_{\text{BGD}}^i \times \frac{B_{\text{SRC}}^i}{B_{\text{BGD}}^i}, \end{aligned}$$

where N^i is the number of photons in i -th bin of the spectrum of the system and S_{SRC}^i is that of the observed spectrum in the SRC region. Hereafter the background spectrum estimated in this method is called BGD⁰ for simplicity.

In order to study the uncertainty in the estimated background we consider the positional dependence of the background spectrum. The background is divided into two types: X-ray background from the aperture of XRT (hereafter CXB type; the cosmic X-ray background and the Galactic background) and others (hereafter NXB type; the

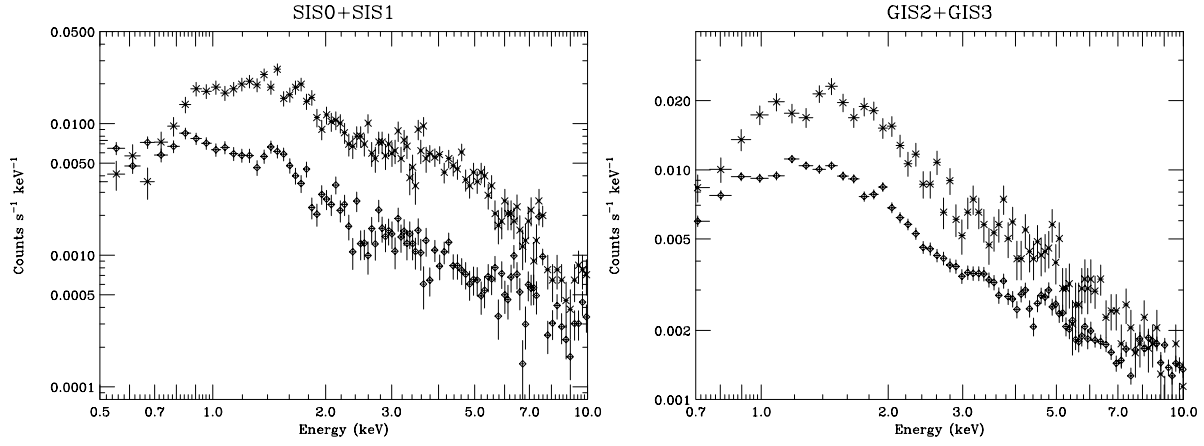


Figure 4.6: The contribution of X-ray emission from the galactic plane. The left panel indicates the contribution to SIS and the right to GIS. In each panel a spectrum in a BGD region is indicated by crosses for obs2 and the blank sky spectrum in the same region is indicated by diamonds. The contribution of galactic ridge emission lies between the two spectra.

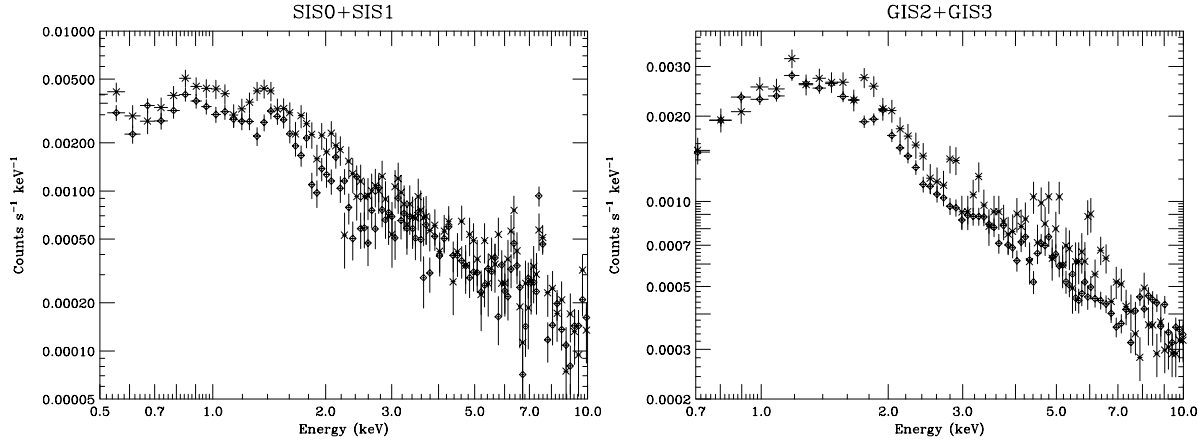


Figure 4.7: Comparison of blank sky spectra in different accumulation regions. In the figure a spectrum in the SRC region is indicated by crosses and that in the BGD region is indicated by diamonds.

instrumental background and non-X-ray background from charged particles). The CXB type background has maximum counting rate on the optical axis of XRT and decreases towards the rim of the detector for both SIS and GIS in all energy bands. On the other hand, the NXB type background has minimum counting rate at the center of the detector and increases towards the rim of the detector for GIS, while it is almost flat for SIS. These two effects cause the total background counting rate to decrease moderately towards the rim of the detector in all energy bands. As a result the counting rate in the SRC region is slightly higher than that in the BGD region because the SRC region lies more inside than the BGD region on average.

Systematic errors in the estimation of the background spectra were studied by creating another two background spectra, under- and overestimating the positional dependence of the background spectrum. The underestimated background spectrum (hereafter BGD⁻) was created by simply multiplying ratio of areas of the SRC and the BGD regions by the spectrum in the BGD region. The ratios of areas are listed in Table 4.5. Because the total background decreases towards the rim of the detector and the SRC region is more inside than the BGD region, BGD⁻ has lower counting rate than the true background. Overestimation was done as follows: the effective area of XRT were averaged in the regions in the sky corresponding to the SRC and the BGD regions, then the Galactic contribution in the spectrum in the BGD region was multiplied by ratio of the averaged effective areas. Figure 4.8 shows the ratio of SIS0 and GIS2 for obs2 as examples. In other words, we overestimated the background spectrum by

$$\begin{aligned} N_{\text{over}}^i &= (\text{the Galactic contribution}) \times R^i + B_{\text{SRC}}^i \\ &= (S_{\text{BGD}}^i - B_{\text{BGD}}^i) \times R^i + B_{\text{SRC}}^i, \end{aligned}$$

where N_{over}^i is the number of photons in the i -th bin of the overestimated spectrum and R^i is ratio of the averaged effective areas shown in Figure 4.8. Hereafter we call the overestimated background spectra created in this way BGD⁺. Figure 4.9 shows comparison of the estimated background spectra. In the figure BGD⁻ is indicated by crosses and BGD⁺ is indicated by squares, with BGD⁰ also shown with diamonds. We can see the difference in three spectra BGD⁺, BGD⁰, and BGD⁻ is comparable with statistical errors in each energy bin.

Table 4.5: Ratios of areas of the SRC and the BGD regions

Sensor	obs1	obs2	obs3	obs4	obs5	obs6
SIS0 + SIS1	0.48519	0.47625	0.47062	0.44464	0.47741	0.46811
GIS2 + GIS3	0.25	0.25	0.25	0.25	0.25	0.25

4.3.2 Spectral Model

With the XSPEC software package the SIS and GIS spectra with BGD⁰ subtracted were fitted with a single power law model and a thermal bremsstrahlung model both with photoelectric absorption. We found that the single power law model described the data well for all six observations. The spectral fits for obs2 are shown in Figure 4.10 as examples.

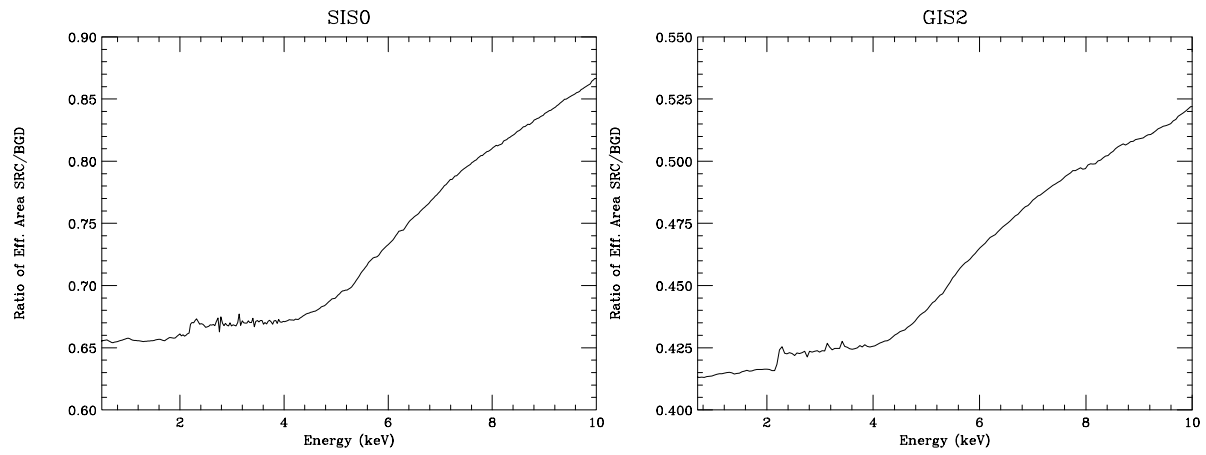


Figure 4.8: Ratios of averaged effective areas of SIS0 (left panel) and GIS2 (right panel) for obs2. In both panel an averaged effective area for the SRC region is divided by that for the BGD region.

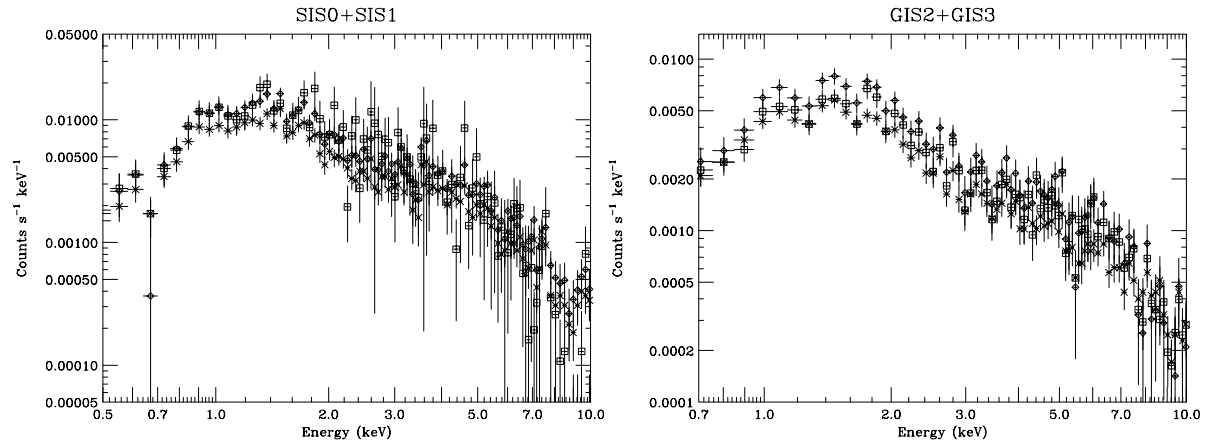


Figure 4.9: Comparison of differently estimated background spectra for obs2. In the figure BGD^- is indicated by crosses and BGD^+ is indicated by squares, with BGD^0 also shown with diamonds.

The results of the independent three-parameter fits with the single power law model are given in Table 4.6. For comparison, we also give in Table 4.6 parameters obtained from the three-parameter fit with the thermal bremsstrahlung model. In all cases, reduced χ^2 -values were only slightly higher for the thermal model compared with that for the power-law model, and we could not rule out the former on the basis of the *ASCA* observations alone. No evidence was found for any line features in the spectra. The upper limits for Iron K emission line flux are listed in Table 4.6. The absence of emission lines argues in favor of the power law model.

From Table 4.6, the model fits to the SIS and the GIS spectra result in identical spectral parameters within their uncertainties except for their normalizations; systematic

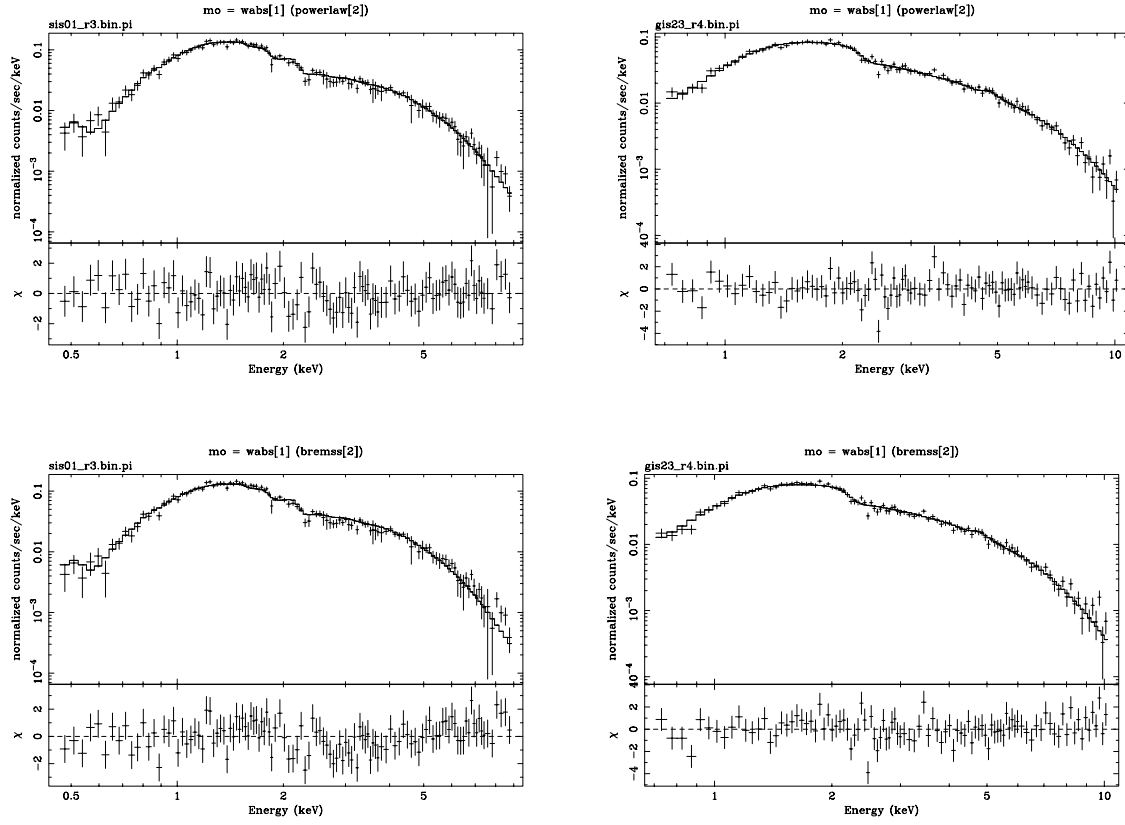


Figure 4.10: Spectral fits to SIS (left panels) and GIS spectra (right panels) for obs2. The spectral model is a single power law model (upper panels) and a thermal bremsstrahlung model (lower panels). BGD⁰ (see §4.3.1) is employed as background spectra. For a single power law model upper limits on Fe emission line flux are also given in the table.

differences between the normalizations are due to calibration inefficiencies reported by the *ASCA* calibration team. In order to obtain more precise spectral parameters, the SIS and the GIS spectra were fit simultaneously by the single power law model and the thermal bremsstrahlung model with common spectral parameters. The SIS and the GIS spectra for the six observations are shown in Figure 4.11. Resultant spectral parameters are listed in Table 4.7 and the intrinsic X-ray luminosities with no intrinsic absorption assumed are plotted in Figure 4.12 with an assumption of 2 kpc for the distance to the system. Because of the reported discrepancies between the SIS and the GIS fluxes, the normalizations for the SIS and GIS spectra were treated as independent parameters.

Confidence contours of the spectral parameters for the single power law model are plotted for six observations in Figure 4.13. The photoelectric absorption toward the source is small and consistent with an intrinsically unabsorbed source in the Galactic plane at the estimated distance to the system. We found no evidence for variation in the

Table 4.6: Best-fit parameters by individual fit to SIS and GIS spectra^{a)}

Power Law Model in Individual Fit to SIS and GIS				
Dataset	$N_{\text{H}}^{\text{b)}$ (10^{22} cm^{-2})	Photon Index ^{b)}	χ^2_{ν}	Fe Emission-Line Flux ($10^{-5} \text{ photons cm}^{-2} \text{ s}^{-1}$)
obs1	0.60(4)/0.60(7)	1.77(7)/1.79(6)	0.94/1.02	< 1.1/1.9
obs2	0.57(4)/0.55(6)	1.92(7)/1.95(6)	0.92/1.00	< 0.67/0.41
obs3	0.53(5)/0.61(7)	1.57(7)/1.75(6)	1.14/1.22	< 4.0/3.6
obs4	0.55(6)/0.67(13)	1.63(9)/1.65(10)	1.15/0.71	< 3.8/1.6
obs5	0.5(3)/0.7(5)	1.5(4)/1.7(4)	0.65/0.79	< 0.40/0.67
obs6	0.3(2)/0.6(4)	1.3(3)/1.8(4)	0.80/0.82	< 0.65/0.11

Thermal Bremsstrahlung Model in Individual Fit to SIS and GIS			
Dataset	$N_{\text{H}}^{\text{b)}$ (10^{22} cm^{-2})	$kT^{\text{b)}$ (keV)	χ^2_{ν}
obs1	0.49(3)/0.42(5)	8(1)/9(1)	1.01/0.97
obs2	0.44(3)/0.33(4)	5.9(7)/6.8(7)	1.16/1.10
obs3	0.45(4)/0.43(6)	15(4)/10(2)	1.25/1.25
obs4	0.46(5)/0.50(9)	11($^{+5}_{-2}$)/14($^{+5}_{-3}$)	1.25/0.87
obs5	0.4(2)/0.6(4)	14($^{(c)}_{-9}$)/12($^{+53}_{-6}$)	0.66/0.79
obs6	0.3(2)/0.4(3)	94($^{(c)}_{-36}$)/8($^{+16}_4$)	0.80/0.84

a) Numbers before a slash are of SIS and those after a slash are of GIS.

b) Numbers in parenthesis represent the 90% confidence interval uncertainties in the last digit quoted. The uncertainties quoted are statistical, and do not include any contribution for unknown systematic calibration errors.

c) Could not be determined because upper boundary of parameter exceeds 200 keV.

absorption with orbital phase, which also argues against intrinsic absorption. In addition, our observed absorptions are consistent with approximate values measured independently near apastron by the *ROSAT* observations (Cominsky et al. 1994; Greiner et al. 1995), although those have large uncertainties.

4.3.3 Systematic Errors in Spectral Analysis

In order to estimate uncertainties in the spectral analysis due to systematic errors in the background estimation, spectral fits were performed with the underestimated background

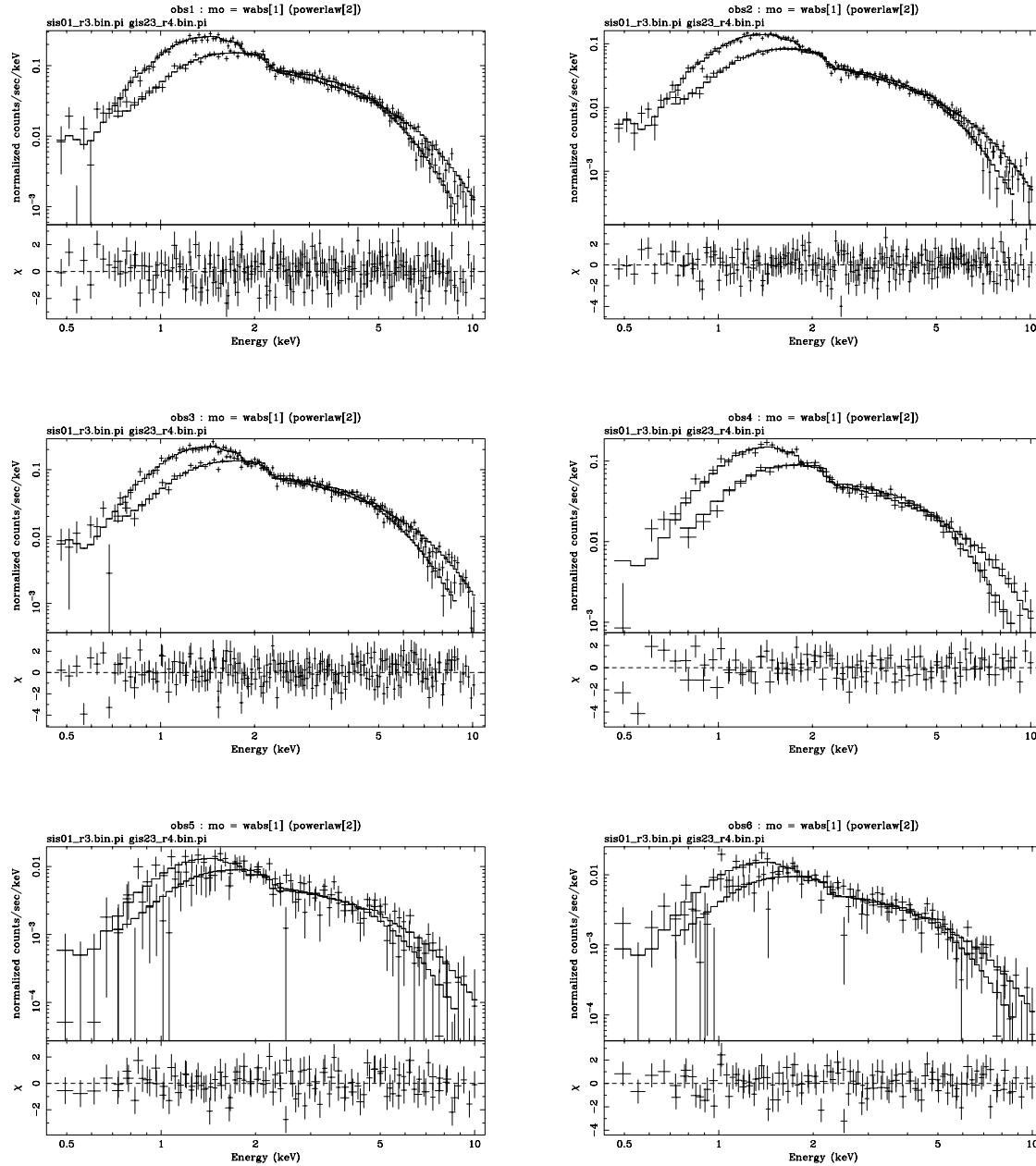


Figure 4.11: X-ray spectra obtained with *ASCA* SIS and GIS. The upper left panel corresponds to *ASCA* obs1, upper right to *ASCA* obs2, middle left to *ASCA* obs2, middle right to *ASCA* obs2, lower left to *ASCA* obs2, and lower right to *ASCA* obs2, respectively.

spectrum BGD^- and the overestimated one BGD^+ subtracted from the source spectrum. Luminosities obtained from the fits with the three backgrounds are compared in Table 4.8. The values in Figure 4.12, for which BGD^0 is used as background, are also listed in the table for comparison. It is seen that fluxes obtained with the three backgrounds are consistent with each other within 90% confidence statistical errors. The confidence

Table 4.7: Model parameters for *ASCA* observations of the PSR B1259–63/SS 2883 system obtained by fitting SIS and GIS spectra simultaneously

Power Law Model in Simultaneous Fit				
	$N_{\text{H}}^{\text{a)}$	Photon Index ^{a)}	1–10 keV Flux ^{a)b)}	χ^2_{ν}
Dataset	(10^{22} cm^{-2})		($10^{-11} \text{ erg cm}^{-2} \text{ s}^{-1}$)	
obs1	0.60(4)	1.78(5)	3.43(19)/2.96(16)	0.97
obs2	0.58(3)	1.96(4)	1.54(8)/1.42(7)	0.96
obs3	0.58(4)	1.69(4)	3.08(18)/2.76(16)	1.22
obs4	0.56(6)	1.61(6)	2.15(18)/1.88(16)	0.98
obs5	0.5(3)	1.6(3)	0.17(5)/0.18(5)	0.71
obs6	0.5(2)	1.6(2)	0.19(6)/0.18(5)	0.84

Thermal Bremsstrahlung Model in Simultaneous Fit				
	$N_{\text{H}}^{\text{a)}$	$kT^{\text{a)}$	1–10 keV Flux ^{a)b)}	χ^2_{ν}
Dataset	(10^{22} cm^{-2})	(keV)	($10^{-11} \text{ erg cm}^{-2} \text{ s}^{-1}$)	
obs1	0.47(3)	8.6(8)	3.19(9)/2.76(7)	1.00
obs2	0.42(2)	6.1(4)	1.40(4)/1.30(4)	1.19
obs3	0.46(3)	11(1)	2.90(8)/2.60(6)	1.29
obs4	0.46(4)	13^{+4}_{-2}	2.04(7)/1.79(6)	1.08
obs5	0.5(2)	12^{+32}_{-4}	0.19(6)/0.18(5)	0.71
obs6	0.4(2)	14^{+26}_{-2}	0.18(3)/0.17(2)	0.84

a) Numbers in parenthesis represent the 90% confidence interval uncertainties in the last digit quoted. The uncertainties quoted are statistical, and do not include any contribution for unknown systematic calibration errors.

b) Numbers before a slash are of SIS and those after a slash are of GIS. Systematic differences between SIS and GIS normalizations is due to calibration inefficiencies reported by the *ASCA* calibration team.

contours by the three fits are shown in Figure 4.14 with results from the spectral fits with BGD⁰ overlaid. Again, the contours with the three backgrounds overlapped each other well within 1σ statistical error bars. In conclusion we found the systematic errors in the spectral analysis due to uncertainties in the background estimation were negligible compared with the statistical errors.

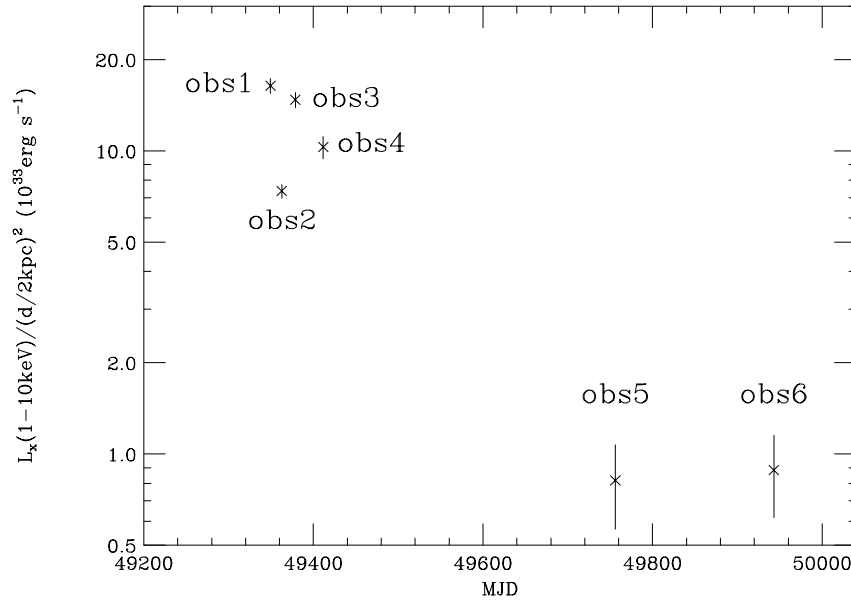


Figure 4.12: Luminosities of the PSR B1259–63/SS 2883 system observed with the *ASCA* satellite. The luminosities were calculated based on results from simultaneous fits to SIS and GIS spectra, with normalizations of the spectral model for SIS spectra used. The distance to the system is assumed to be 2kpc.

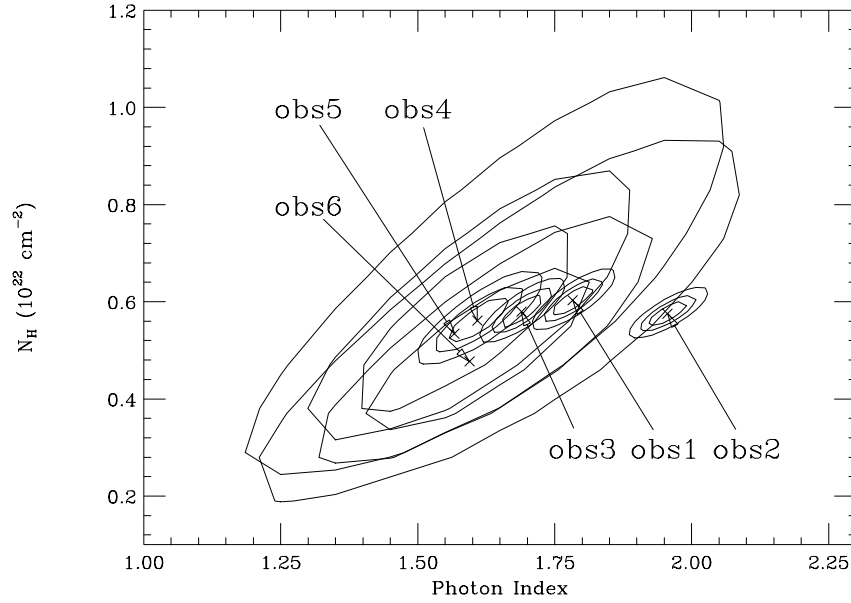


Figure 4.13: Confidence contours for a single power law model by simultaneous fits to SIS and GIS spectra.

4.4 Temporal Analysis

Short time variability of X-ray emission from the PSR B1259–63/SS 2883 system was studied by X-ray light curves and by search for the 48 ms pulsation. For these investi-

Table 4.8: Comparison of 1–10 keV SIS fluxes^{a)}

Background	1–10 keV SIS Flux (10^{-11} erg cm $^{-2}$ s $^{-1}$)					
	obs1	obs2	obs3	obs4	obs5	obs6
BGD $^{-}$	3.50(18)	1.60(8)	3.11(17)	2.18(18)	0.193(46)	0.211(45)
BGD 0	3.43(19)	1.54(8)	3.08(18)	2.15(18)	0.171(53)	0.185(56)
BGD 0	3.43(9)	1.53(7)	3.03(9)	2.11(18)	0.172(59)	0.181(56)

a) The fluxes were results from simultaneous fits to SIS and GIS spectra.

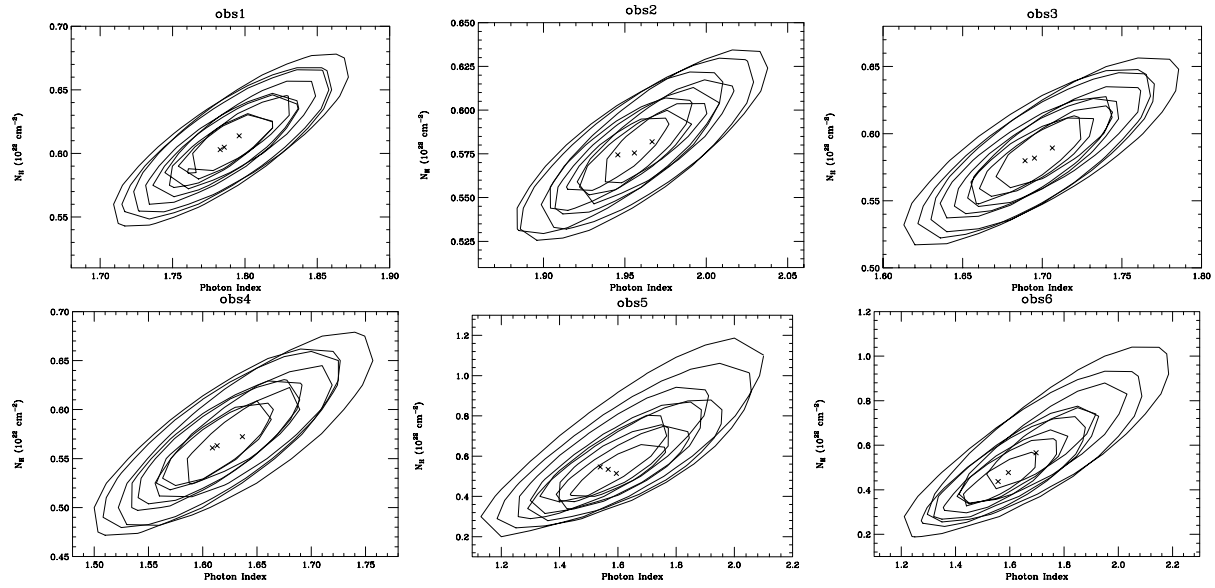


Figure 4.14: Confidence contours for a single power law model with three different types of backgrounds BGD 0 , BGD $^+$, BGD $^-$. The upper left panel is the contours of obs1, upper central is of obs2, upper right is of obs3, lower left is of obs4, lower central is of obs5, and the lower right is of obs6, respectively.

gations temporal analyses were done with the software packages developed originally on the ASCA_ANL platform. For the temporal analyses we selected photons within $3'$ for SIS and $4'$ for GIS from the position of the X-ray source, *i.e.*, photons in the SRC region in Figure 4.4. GIS2 and GIS3 data were combined with each other to obtain maximum sensitivity in searching for the 48 ms pulsation. Because of the insufficient time resolution, SIS data could not be used for the search, while it is available for drawing the X-ray light curves.

4.4.1 X-ray Light Curve

Stability of X-ray emission is a characteristics to be investigated. It is known that emission from Crab-like pulsars are very stable (e.g. Sekimoto et al. 1995), while X-ray pulsars exhibit rapid variability in the X-ray flux. Hence X-ray stability gives us another important information in determining origin of the X-ray emission from the system. In order to study the stability of the X-ray emission from the system X-ray light curves were integrated. Figure 4.15 shows the light curves for SIS and GIS data at all six observed epochs. In the figure counting rates are plotted against elapsed time from the beginnings of observations. SIS0 data and SIS1 data were summed and GIS2 data and GIS3 data were also combined with each other. The data shown in the figure have been binned in 300 s intervals and divided by the exposure time of each bin. We note the absence of any rapid variability in the X-ray flux and the X-ray emission is very stable within the time scale of the *ASCA* observation ~ 1 day.

4.4.2 Search for X-ray Pulsations

The X-ray emission from the system may be pulsed with a 48 ms period, because X-rays can originate from the magnetospheric or from the surface as in the case of the Crab and the Vela pulsars. Or, it may be emitted from accreted matter channeled by the strong pulsar magnetic field (3.3×10^{11} G) as in the case of the Be-star system A0538–66, which produced pulsed X-ray emission with a 69 ms period during a strong outburst in 1982 (Skinner et al. 1982). In both cases the X-ray emission is pulsed with the same period of as neutron star’s spin. Thus, pulsed X-rays from PSR B1259–63 are a possibility that requires investigation.

Preceding the pulsar search, a few corrections were done to photon arrival times as follows. We first converted the arrival time of a photon into “barycentric time”, when the photon should have arrived at the solar system barycenter. This conversion is called the “barycentric correction” and cancels the Doppler effect by the orbital motion of the satellite and the motion of the earth around the solar system barycenter. After the barycentric correction, we further corrected the arrival time into a time when the photon should have arrived at the solar system barycenter if the photon had been emitted at the center of gravity of the binary system (hereafter “binary correction”). This correction cancels the Doppler shift caused by the motion of PSR B1259–63 in the binary system. The JPL ephemeris was used for the barycentric correction and the orbital parameters by Manchester et al. (1995) was used for the binary correction.

Then, the resultant time series data were “epoch-folded”. For the corrected photon

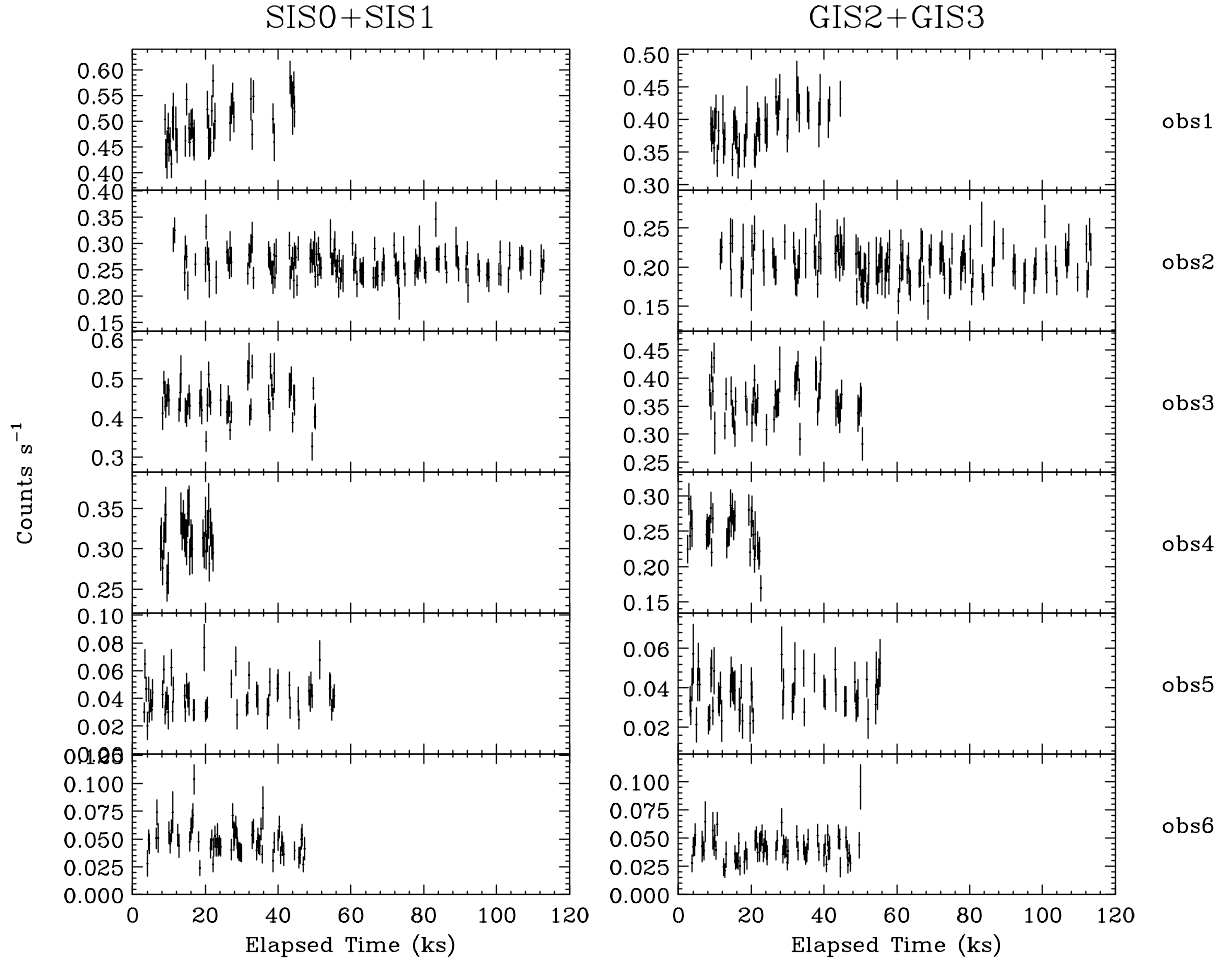


Figure 4.15: Light curves of the PSR B1259–63/SS 2883 system at the six observed epochs. In the figure counting rates are plotted against elapsed time from the beginnings of observations. The data shown here have been binned in 300 s intervals and divided by the exposure time of each bin.

arrival time, we compute a quantity ϕ by

$$\phi = \frac{t - t_0}{P_{\text{trial}}},$$

where t is a photon arrival time, t_0 is an arbitrary start time called the “epoch”, and P_{trial} is a trial period of pulsation. The integer part of ϕ means the number of rotations since time t_0 , and the decimal part of ϕ , called the “pulse phase”, represents when within a pulse period the photon arrives. The distribution of the pulse phase is called a “folded light curve” and shows the intrinsic pulse profile of the X-ray emission from the pulsar. For each folded light curve, we computed

$$S = \sum_{k=1}^j \frac{(C_k - C)^2}{\sigma_k^2},$$

where C_k is the observed counting rate of the k th phase bin, C is the averaged counting rate, σ_k is defined by $\sigma_k \equiv jC/T$, and T is the duration of the observation. S values were calculated with hundreds of trial periods near the expected pulse period. If coherent pulsations exist in the data, the quantity S becomes large with a maximum at the pulse period.

The expected pulse period of PSR B1259–63, as determined by the radio ephemeris (Manchester et al. 1995), is listed in Table 4.9. The search was done within $\pm 1\mu\text{s}$ from the expected period. The period range was oversampled by setting a step in the pulsation search to $P^2/5T$, or one fifth of the Fourier step, where P is the expected period and T is duration of the observation. Figure 4.16 shows a plot of S values versus trial periods, called a “periodgram”, with $j = 32$. In the figure the trial periods were subtracted from the expected period at the observation. Dashed lines in the figure are pulse detection limits with 99% confidence, estimated with a method discussed by Leahy et al. (1983); the detection limit is determined so that 1% is the probability that a data set from a constant counting rate (*i.e.*, with no pulsation included) exceeds the detection limit by chance. No significant pulsations can be seen in the figure. Searches for pulsation by the epoch-folding method were also done with $j = 8, 16, 32$ to ensure sensitivity to a variety of pulse profiles. In addition searches in the 0.5–2 keV and 2–10 keV bands were performed individually to detect possible pulsations only seen in a narrow energy band. Again, no significant pulsations were detected. In conclusion, we detected no X-ray pulsations at the radio period.

Table 4.9: Expected pulse period and parameters for the pulsation search

Dataset	MJD	$P_{\text{exp}}^{\text{a)}$ (ms)	Period Range (ms)	Step (ns)	$N_p^{\text{b)}$	$\delta P^{\text{c)}$ (ns)
obs1	49349.02083	47.762309	47.7613 – 47.7633	10	201	51
obs2	49362.13889	47.762311	47.7613 – 47.7633	4	501	20
obs3	49378.46528	47.762315	47.7613 – 47.7633	10	201	46
obs4	49411.50000	47.762321	47.7613 – 47.7633	20	101	115
obs5	49755.73958	47.762389	47.7614 – 47.7634	8	250	41
obs6	49942.65278	47.762426	47.7614 – 47.7634	8	250	43

a) Expected period calculated based on radio data by Manchester et al. (1995).

b) Number of trial periods.

c) Fourier step defined as $\delta P = P_{\text{exp}}^2/T$ with duration of an observation T .

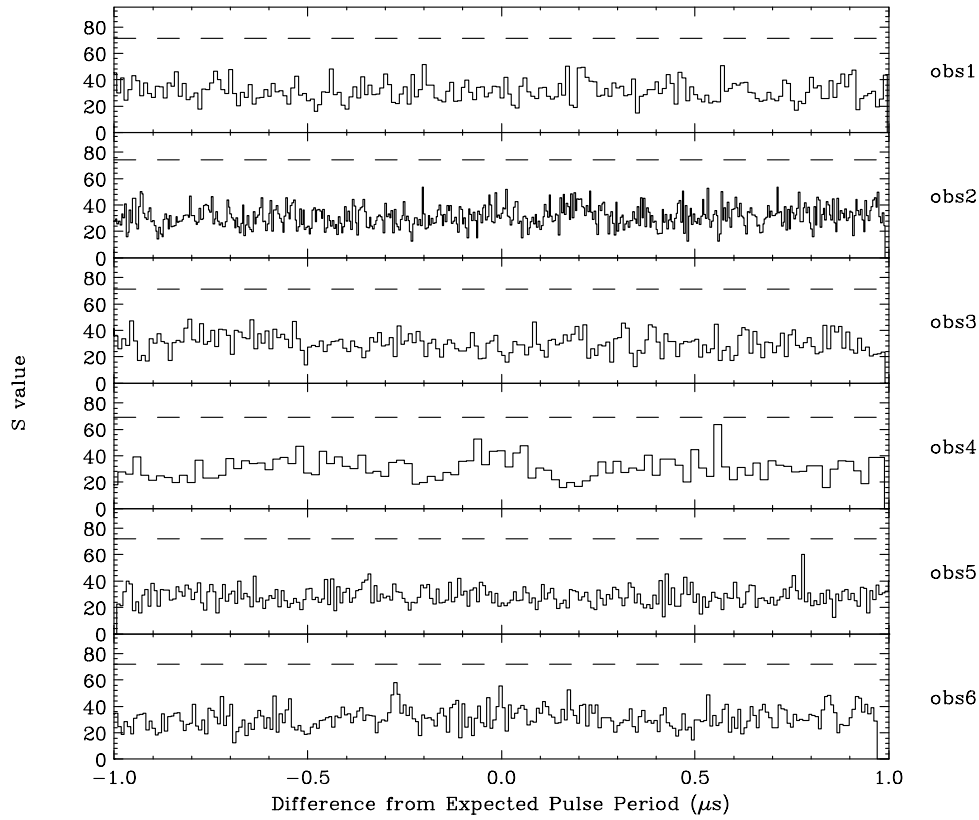


Figure 4.16: Periodograms, *i.e.*, plots of S values versus trial periods, for six observed epochs. GIS2 and GIS3 data were combined with each other. In the figure periods were subtracted by the expected period of the observation. Dashed lines in the figure is a pulse detection limit with 99% confidence, estimated in a method discussed by Leahy et al. (1983).

We also tried Z_n^2 test (Buccheri et al. 1983) for our data. In this test the quantity Z_n^2 is computed by

$$Z_n^2 = \sum_{k=1}^n \left[\left\{ \sum_{j=1}^N \cos(k \cdot 2\pi\phi_j) \right\}^2 + \left\{ \sum_{j=1}^N \sin(k \cdot 2\pi\phi_j) \right\}^2 \right],$$

where N is the number of photons, and ϕ_j is the pulse phase of j -th photon. Again, Z_n^2 values were calculated with hundreds of trial periods near the expected pulse period. If coherent pulsations exist in the data, the quantity Z_n^2 also becomes large with a maximum at the pulse period.

The trial periods are the same as in the search by the epoch-folding and listed in Table 4.9. Figure 4.17 shows a plot of Z_n^2 values against trial periods for $n = 1$ and Figure 4.18 show that for $n = 2, 3, 4$. No significant pulsations can be seen in the figure, except for obs4; we have a peak around the expected pulse period in the figure for obs4. In order to confirm the periodicity seen at obs4 a folded light curve at the expected period was integrated at the expected pulse period from the radio data (Manchester et al. 1995).

The folded light curves are shown in Figure 4.19 for all six observations. The shapes of all the folded light curves look consistent with X-ray emission with a constant flux. In addition we have no significant S value at the period (Figure 4.17). Both facts argue against the pulse detection at obs4. Searches for pulsation by the Z_n^2 test were also done for the 0.5–2 keV and 2–10 keV bands individually to detect possible pulsations only seen in a narrow energy band. No significant pulsation was detected even for obs4 in this case. From these facts, in conclusion, we again detected no X-ray pulsation at the radio period.

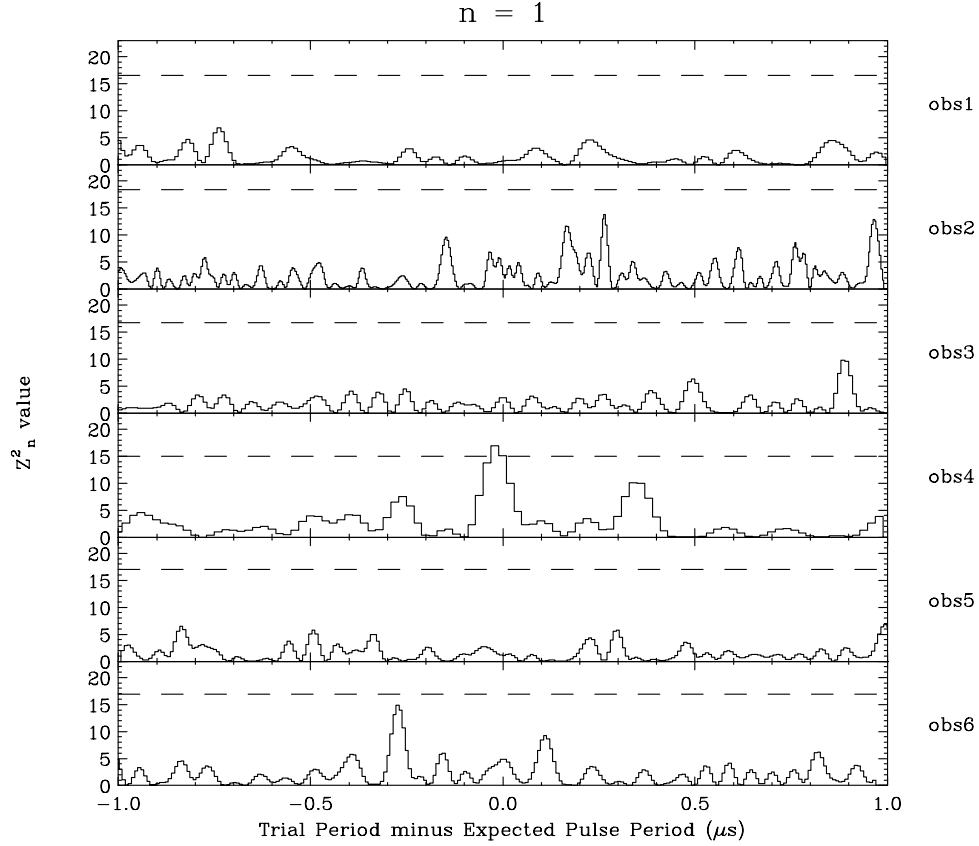


Figure 4.17: Z_n^2 values versus trial periods for $n = 1$. GIS2 and GIS3 data were combined with each other. In the figure periods were subtracted from the expected period of the observation. Dashed lines in the figure are the pulse detection limit with 99% confidence, estimated using a method discussed by Leahy et al. (1983).

As an additional check we searched the X-ray pulsation without the binary correction. Since the orbital period of the PSR B1259–63/SS 2883 system (~ 3.4 year) is much longer than duration of the *ASCA* observations (~ 1 day), the Doppler effect due to the binary motion can be represented by a combination of a constant shift in pulse period and a constant period derivative for all six observations. This allows us to search for pulsations

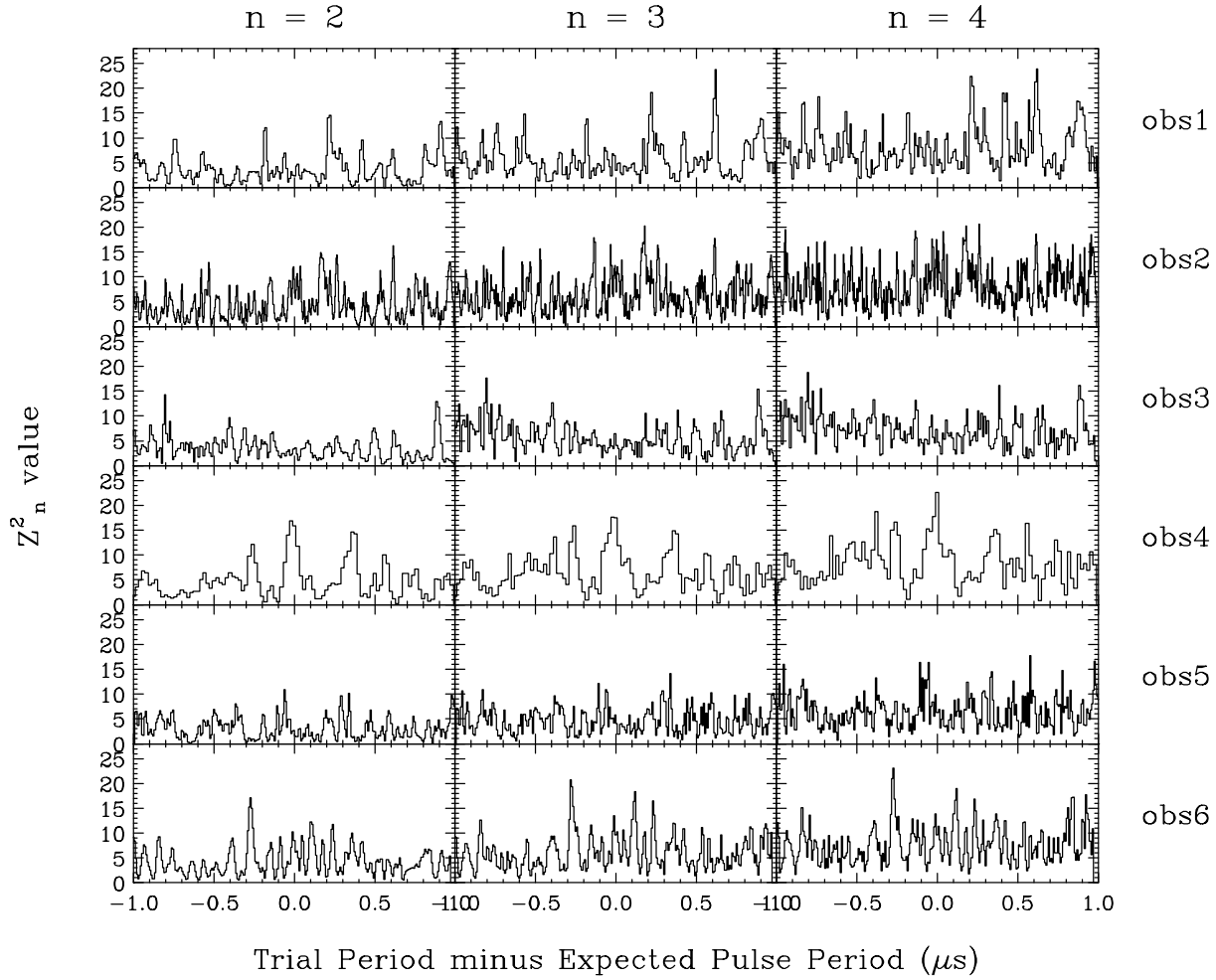


Figure 4.18: Z_n^2 values versus trial periods for $n = 2, 3, 4$. GIS2 and GIS3 data were combined with each other. In the figure periods were subtracted by the expected period of the observation.

in $P-\dot{P}$ space. After the barycentric correction a pulse phase is calculated by

$$\phi = \frac{t - t_0}{P_{\text{trial}}} - \frac{1}{2} \frac{\dot{P}_{\text{trial}}}{P_{\text{trial}}^2} (t - t_0)^2,$$

where P_{trial} is a trial period and \dot{P}_{trial} is the apparent period derivative due to the binary motion.

The search was done with the epoch-folding method around the period shifts and the period derivatives expected based on the ephemeris by Manchester et al. (1995). In Table 4.10 expected period shifts and derivatives are listed with parameters for the pulsation search in $P-\dot{P}$ space. As a result, no significant pulsations were detected in this search. This result supports and confirms the previous result from the epoch-folding search with the binary correction.

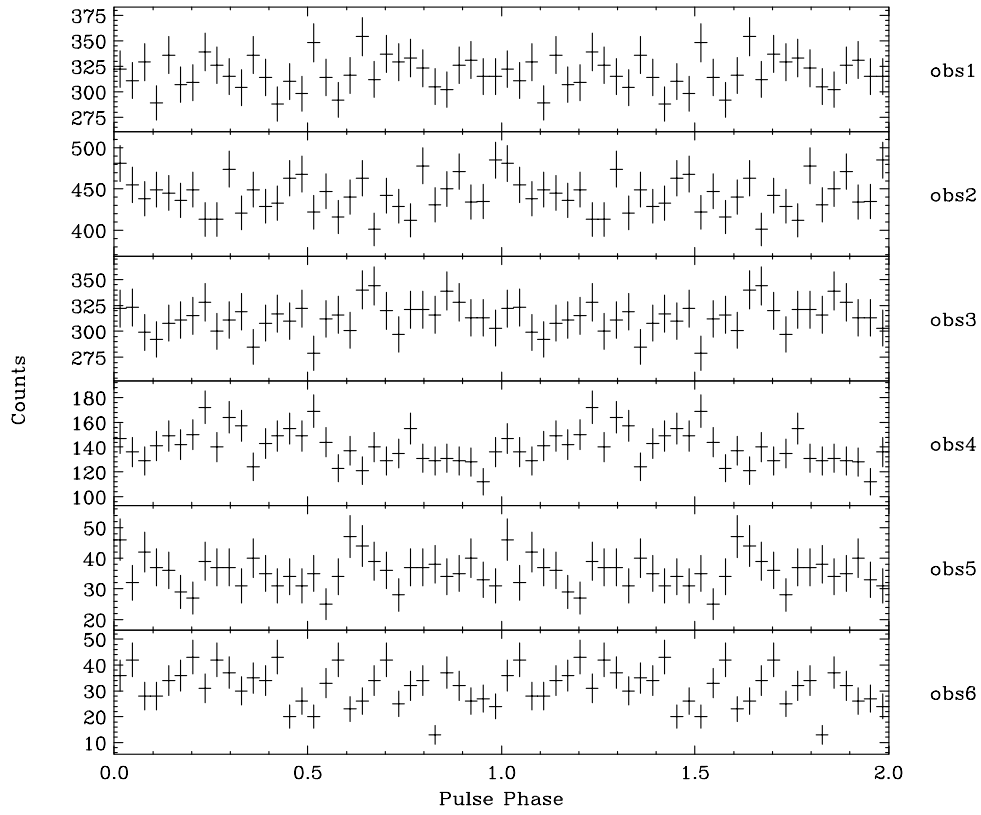


Figure 4.19: Folded light curve at the expected pulse period. GIS2 and GIS3 data were combined with each other.

Table 4.10: Apparent pulse periods and parameters for pulsation search in P - \dot{P} space

	MJD	$P_{\text{app}}^{\text{a)}}$	$\dot{P}_{\text{app}}^{\text{b)}}$	Period Range	\dot{P} Range
Dataset		(ms)	(10^{-12})	(ms)	(10^{-12})
obs1	49349.02083	47.760768	-4.8	47.7600 – 47.7616	-20.0 to 0.0
obs2	49362.13889	47.751241	-6.7	47.7613 – 47.7633	-8.0 to -5.0
obs3	49378.46528	47.752691	+2.7	47.7613 – 47.7633	0.0 to +18.0
obs4	49411.50000	47.756972	+0.81	47.7559 – 47.7579	0.0 to +2.0
obs5	49755.73958	47.762203	+0.057	47.7614 – 47.7634	0.0 to +0.12
obs6	49942.65278	47.763017	+0.042	47.7614 – 47.7634	0.0 to +0.10

a) Apparent pulse periods expected from ephemeris by Manchester et al. (1995).

b) Apparent period derivatives expected from ephemeris by Manchester et al. (1995).

4.4.3 Upper Limit on X-ray Pulsation

The upper limits to the pulsed component in our data were estimated with a method described in Leahy et al. (1983). In the method the pulse profile is assumed to be

sinusoidal in shape, expressed as

$$r(t) = r_0 \left[1 + A \sin \left(\frac{t}{P} \right) \right],$$

where $r(t)$ is the instantaneous counting rate at time t , r_0 is an averaged counting rate, A is a pulsed fraction to be estimated, and P is a pulse period. When we epoch-folded the photon arrival times, the S value for the data includes contributions of statistical fluctuations χ_{noise}^2 and of sinusoidal shape χ_{signal}^2 , *i.e.*, $S = \chi_{\text{noise}}^2 + \chi_{\text{signal}}^2$. Since χ_{signal}^2 increases as the pulsed fraction increases, the upper limit on the pulsation is calculated from the maximum value of χ_{signal}^2 . The maximum χ_{signal}^2 , in turn, is determined so that χ_{noise}^2 is as small as possible under a given confidence level. Because χ_{noise}^2 obeys χ^2 distribution with $(n - 1)$ degrees of freedom for a n -bin folded light curve, the desired χ_{signal}^2 at percent confidence level c is given by solving

$$(1 - c/100) = N_p Q_{n-1}(S_{\text{max}} - \chi_{\text{signal}}),$$

where N_p is the number of independent trial periods, $Q_n(\chi^2)$ is the integrated χ^2 distribution with n degrees of freedom, and S_{max} is the maximum value of S in the search. Leahy et al. (1983) showed χ_{signal} as a function of a pulsed fraction A is given by

$$\chi_{\text{signal}} = \frac{0.935}{2} A^2 N_\gamma \frac{\sin^2(\pi/n)}{(\pi/n)^2},$$

where N_γ is the number of photons. The pulsed fraction A determined in this way is an upper limit on the X-ray pulsation at percent confidence level c .

Listed in Table 4.11 are the upper limits on the X-ray pulsation from the PSR B1259–63/SS 2883 system at the 99% confidence level. The limits were estimated by the pulsation searches with the epoch-folding method with $j = 32$ for three energy bands: 0.5–10 keV (full band), 0.5–2 keV, and 2–10 keV. In the table upper limits on the amplitude of counting rates, AN_γ divided by net exposure time, are also listed.

Table 4.11: Upper limits on X-ray pulsation^{a)}

Dataset	0.5–10 keV		0.5–2 keV		2–10 keV	
	Fraction ^{b)}	Flux ^{c)}	Fraction ^{b)}	Flux ^{c)}	Fraction ^{b)}	Flux ^{c)}
obs1	8.71	0.0338	15.1	0.0204	11.8	0.0280
obs2	7.58	0.0155	13.4	0.0114	10.7	0.0125
obs3	8.38	0.0302	18.4	0.0243	11.3	0.0253
obs4	15.1	0.0378	22.2	0.0187	15.3	0.0249
obs5	29.1	0.0110	44.8	0.00642	36.3	0.00828
obs6	29.9	0.0125	49.6	0.00783	37.0	0.00902

a) Calculated with 99% confidence.

b) In units of percent.

c) In units of photons s⁻¹.

Chapter 5

Discussion

5.1 Summary of ASCA results

Before discussing possible mechanisms of X-ray emission from the PSR B1259–63/SS 2883 system, we review the *ASCA* results presented in the previous chapter. In all six observations we have clearly detected the system in the energy band ranging from 1 keV to 10 keV. From spectral and temporal analyses of the *ASCA* data, we found several characteristics of the X-ray emission from the system: a power law spectrum with little absorption, a constant column density, no rapid variation in X-ray flux on time scales from minutes to hours, absence of X-ray pulsations in all six observations, orbital dependent X-ray luminosity, and spectral softening at periastron.

The spectral results in Table 4.7 shows that the *ASCA* spectra are well represented by a single power law model with a photon index ranging from 1.5 to 1.9 absorbed by an equivalent column density $N_{\text{H}} \sim 6 \times 10^{21} \text{ cm}^{-2}$, which is consistent with the interstellar absorption toward the system. From confidence contours of the spectral parameters in Figure 4.13 we find the photon index significantly changes near the periastron, while the column density remains constant. The change in the photon index is plotted against a binary separation in Figure 5.2 assuming masses of $1.4 M_{\odot}$ for PSR B1259–63 and $10 M_{\odot}$ for SS 2883 assumed.

No rapid variations and no pulsations were observed in any of the six observed epochs, though a radio pulsation was detectable at obs4 and later. Upper limits on the X-ray pulsation at the period expected by radio data by Manchester et al. (1995) are listed in Table 4.11. We converted these into pulsed luminosities assuming the best fit spectral parameters in Table 4.7 and the assumed distance to the system $d = 2 \text{ kpc}$. The results are summarized in Table 5.1. In the table, numbers in parentheses are percentages of the upper limits on the pulsed luminosity divided by the spin-down luminosity

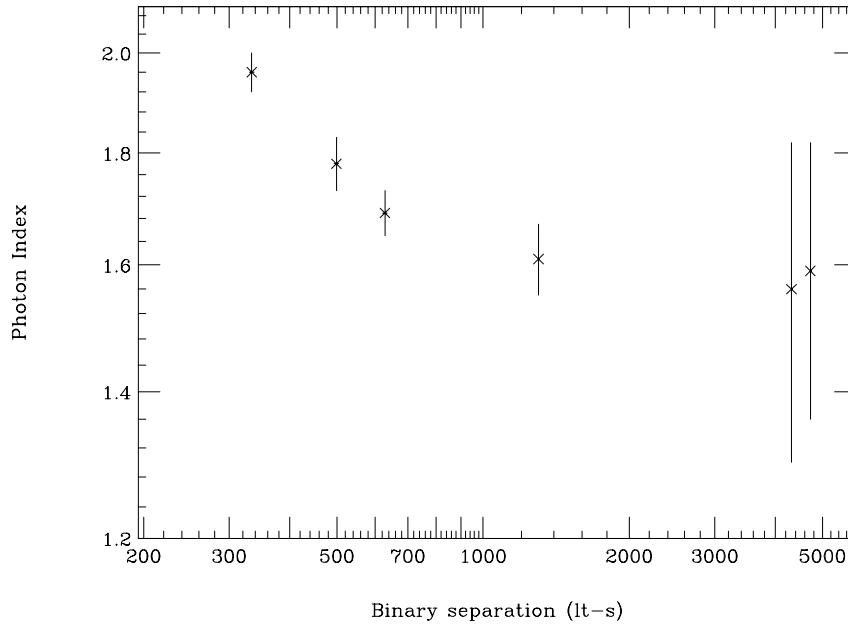


Figure 5.1: Photon indices of the PSR B1259–63/SS 2883 system from obs1 through obs6 is plotted against a binary separation assuming $1.4 M_{\odot}$ of PSR B1259–63 and $10 M_{\odot}$ of SS 2883.

of PSR B1259–63, $\dot{E}_{\text{rot}} = 8.28 \times 10^{35} \text{ erg s}^{-1}$, under the assumption of neutron star’s moment of inertia $I = 10^{45} \text{ g cm}^2$. Compared with the Crab pulsar, in which 0.3% of its spin-down luminosity is pulsed in energy band between 1 and 10 keV, these upper limits are quite small.

Table 5.1: Upper limits on pulsed X-ray luminosity

Dataset	0.5–10 keV		0.5–2 keV		2–10 keV	
	$L_{\text{UL}}^{\text{a)}$	$L_{\text{UL}}/\dot{E}_{\text{rot}}^{\text{b)}$	$L_{\text{UL}}^{\text{a)}$	$L_{\text{UL}}/\dot{E}_{\text{rot}}^{\text{b)}$	$L_{\text{UL}}^{\text{a)}$	$L_{\text{UL}}/\dot{E}_{\text{rot}}^{\text{b)}$
obs1	15.8	0.19%	9.19	0.11%	13.0	0.16%
obs2	7.26	0.088%	5.29	0.064%	5.62	0.064%
obs3	13.9	0.17%	5.63	0.068%	12.0	0.14%
obs4	12.6	0.15%	7.53	0.091%	11.6	0.14%
obs5	4.82	0.058%	2.31	0.028%	3.80	0.046%
obs6	5.63	0.068%	2.54	0.031%	4.62	0.056%

a) Upper limits on pulsed X-ray luminosity with 99% confidence in units of $10^{32} \text{ erg s}^{-1}$.

b) Spin-down luminosity of the PSR B1259–63. $\dot{E}_{\text{rot}} = 8.28 \times 10^{35} \text{ erg s}^{-1}$.

Here we present an argument against a pulse detection in obs4, even though the Z_n^2 value for obs4 slightly exceeds the 99% detection limit (see Figure 4.17). We found the upper limit for obs5 (0.058%), much less than the upper limit for obs4 (0.15%). We should

have observed the pulsed X-rays from the pulsar at obs5 if we detected real pulsations at obs4, if the pulsed emission from the pulsar does not vary. Sekimoto et al. (1995) showed that the pulsed emission from Crab-like pulsars is quite stable. If PSR B1259–63 emits pulsed X-rays as other Crab-like pulsars do, we would observe a steady pulsed component from the pulsar. In conclusion the pulse detection in obs4 is unlikely to be real, assuming the Crab-like pulse emission.

As is clear from Table 4.7 and Figure 4.12, the X-ray flux from the source was time-variable on a long time scale of weeks to a year. The variability in the X-ray luminosity is plotted against the binary separation in Figure 5.2 assuming masses of $1.4 M_{\odot}$ for PSR B1259–63 and $10 M_{\odot}$ for SS 2883, and a distance to the PSR B1259–63/SS 2883 system of $d = 2$ kpc. The X-ray luminosity near periastron is 10 times larger than that at apastron. At periastron, in addition, the luminosity drops to almost half of the values symmetrically around periastron. In the figure results from the previous X-ray missions are also plotted (Makino & Aoki, private communication; Cominsky et al. 1994; Greiner et al. 1995) with luminosity in the literature converted into that in 1–10 keV band.

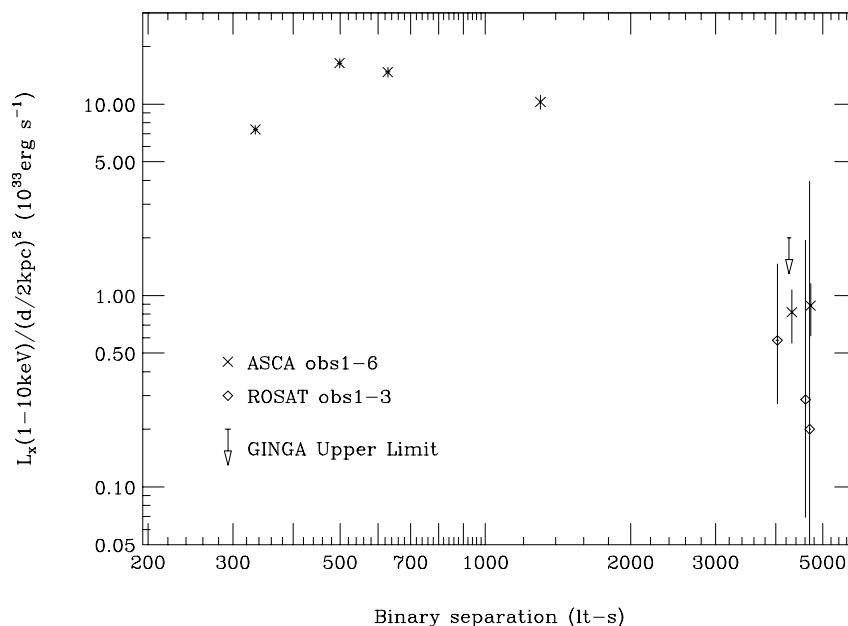


Figure 5.2: Luminosities of the PSR B1259–63/SS 2883 system from obs1 through obs6 are plotted against a binary separation assuming masses of $1.4 M_{\odot}$ for PSR B1259–63 and $10 M_{\odot}$ for SS 2883, and a distance to the PSR B1259–63/SS 2883 system $d = 2$ kpc. In the figure results from the previous X-ray missions are also plotted (Makino & Aoki, private communication; Cominsky et al. 1994; Greiner et al. 1995) with the luminosities in the literature extrapolated to the 1–10 keV band.

The observations by other missions in the soft and hard X-ray band are important to interpret the *ASCA* results. With the *OSSE* instrument aboard the *Compton Gamma-*

Ray Observatory the PSR B1259–63/SS 2883 system was observed for two weeks near periastron, and hard X-rays from the system were detected significantly up to 200 keV (Grove et al. 1995). Grove et al. (1995) showed that the spectrum obtained by the *OSSE* instrument during the periastron passage is consistent with a single power law model determined by Kaspi et al. (1995b) with the *ASCA* data of obs1, obs2, and obs3. Although the *ASCA* spectra could not rule out a thermal bremsstrahlung model with a relatively high temperature of several keV (see Table 4.7), the *OSSE* spectrum is inconsistent with the model because the *ASCA* spectra requires $kT \leq 15$ keV with 99% confidence and a thermal spectrum of such low temperature cannot reproduce the *OSSE* result. Hence, taking the detection of hard X-rays from the system by *OSSE* into account, we can conclude the thermal model is ruled out.

The *ROSAT* data in Figure 5.2 also helps us to interpret the time variability in X-ray luminosity. The PSR B1259–63/SS 2883 system was observed with the *ROSAT* three times around the previous apastron passage in 1992. Observed luminosities, converted into that in 1–10 keV band, are consistent with the *ASCA* results in this thesis (Figure 5.2). This fact supports the idea the observed time-variability in the X-ray luminosity is due to the change in the pulsar’s position in the system and not to intrinsic fluctuation of the X-ray emission.

As a result from the X-ray study on the emission from the PSR B1259–63/SS 2883 system, we obtain the following observational facts in X-ray band:

- 1) The emission is non-thermal and unpulsed.
- 2) The luminosity has no rapid variation.
- 3) The spectrum softens at periastron.
- 4) The luminosity depends on the pulsar’s orbital position.

In the following sections we discuss the X-ray emission from the system based on these observational facts.

5.2 Mechanism of X-ray Emission

Based on the observational facts listed in the previous section, here we consider various possible origins of the X-rays we have observed. The possible origins of X-ray emissions in the PSR B1259–63/SS 2883 system are coronal emission from the Be star, rotation-powered emission from the pulsar, emission from accretion onto the neutron star surface, emission from accreted materials intercepted by the pulsar’s magnetosphere, and emission from a shock front formed at the location where the ram pressures of the Be stellar wind

and the pulsar wind balance. Hereafter we examine contributions of these models for the observed X-rays to explain the results of the X-ray observations presented in this thesis.

5.2.1 Coronal Emission from the Be Star

Early-type B stars are known to emit X-rays, explained as originating from a line-driven wind heated by shocks (Bjorkman and Cassinelli 1993; Macfarlane and Cassinelli 1989; Lucy 1982). The observed X-ray luminosity L_X scales roughly with bolometric luminosity L_{bol} with proportionality constant $\sim 10^{-7}$ (Pallavicini et al. 1981). In a recent *ROSAT* survey of OB and OBe stars by Meurs et al. (1992), a similar relationship was found with *ROSAT* L_X/L_{bol} ranging from 10^{-8} to 10^{-4} , and no significant difference between X-ray luminosities of OB stars and OBe stars. Cassinelli et al. (1994) used *ROSAT* observations of B stars to reveal a transition in X-ray properties as a function of spectral type, with L_X/L_{bol} smaller for stars later than about B1 to B1.5. The bolometric luminosity for SS 2883 is $5.8 \times 10^4 L_{\odot} = 2.2 \times 10^{38} \text{ erg s}^{-1}$ as reported by Johnston et al. (1992b) assuming a distance of 2 kpc. The observed X-ray luminosities fall in the range $L_X = (0.8 - 16) \times 10^{33} \text{ erg s}^{-1}$ and imply $L_X/L_{\text{bol}} = (0.4 - 7) \times 10^{-5}$. Although this is larger than the empirical relationship by Pallavicini et al. (1981) by more than one order of magnitude, this is consistent with the relationship by Meurs et al. (1992) within the scatter.

Cassinelli et al. (1994) showed that X-ray spectra of main and near-main sequence B stars are characterized by emission from gas at a temperature of $\sim 2 \times 10^6$ K, with the brightest X-ray source in their sample having temperature 9.3×10^6 K. According to our spectral fits with the thermal bremsstrahlung model, the *ASCA* spectra are characterized by much higher temperatures, $T \sim 10^8$ K (see Table 4.7; $1 \text{ keV} = 1.2 \times 10^7$ K). Furthermore, the thermal model is ruled out by combining the *OSSE* and *ASCA* results at periastron. Finally, the fact that the observed X-ray luminosity decreases from periastron to apastron is hard to explain by coronal emission from the Be star. We therefore conclude that the coronal emission from the Be star is an unlikely source of the observed X-rays.

5.2.2 Emission from the Pulsar as a Spin-Powered Pulsar

Short period pulsars are occasionally observed to emit X-rays. Although high-energy emission is generally associated with pulsars having much smaller characteristic ages than that of PSR B1259–63 ($\sim 3 \times 10^5$ year), its short pulsation period of 48 ms makes it a plausible X-ray emitter. X-rays from isolated neutron stars are observed in two different forms: X-rays are produced either in the form of pulsations (e.g. Seward and Harnden

1982; Seward et al. 1984), or in weak unpulsed thermal emission arising from the cooling of the neutron star (e.g. Cordova et al. 1989; Halpern and Ruderman 1993). The observed X-rays, however, were non-thermal and unpulsed and we derived an upper limit on the pulsed fraction divided by its spin-down luminosity much smaller than that observed for the Crab pulsar. Furthermore, the X-ray luminosity would not be expected to vary with its orbital phase in either of the above cases. In conclusion both of these scenarios are ruled out.

5.2.3 Emission from Accretion onto the Neutron Star Surface

In binary systems consisting of a neutron star with strong magnetic field and a massive main-sequence star, X-rays from matter accretion onto the neutron star surface are generally expected. In such systems the stellar wind is trapped and channeled by the strong magnetic field of the neutron star and falls onto its magnetic pole. Near the pole infalling materials release their gravitational potential energy which is converted into high energy photons. Because the emission occurs locally at the magnetic pole of the neutron star, X-rays are emitted with a strongly anisotropic angular pattern (Shapiro and Teukolsky 1983). Observed X-rays are, therefore, modulated as neutron star spins if the magnetic dipole axis is tilted with respect to the neutron star rotation axis. Thus X-ray emission in this scenario is likely to be pulsed. Furthermore, Nagase (1989) reviewed X-ray observations of such accretion-powered pulsars and pointed out spectral features such as iron $K\alpha$ emission lines are commonly seen in X-ray spectra. From such systems spectral steepening at energies 10–40 keV is also commonly observed, as summarized by White et al. (1983).

The observed X-rays from the PSR B1259–63/SS 2883 system argues against the accretion scenario. First of all, no pulsations were detected from the *ASCA* data, while the radio pulsations was detectable for obs4 and later. Because the detection of the radio pulsations indicates that the magnetic pole can be seen from the earth, the absence of X-ray pulsation cannot be explained by invoking a geometry which hides the pole from the earth. Also, if accretion took place in the system, the radio pulsations should have been quenched and would not have been observed. In addition, the spectra observed with *ASCA* are well represented by the single power law model with no emission lines. Furthermore, by taking the *OSSE* spectrum into account, no spectral cut off was observed from the system. From these observational facts, we conclude this accretion scenario is unlikely to explain the X-ray emission from the system.

The accretion scenario is unlikely also from theoretical points of view. With reasonable assumptions about the ram pressures of the pulsar wind and the Be stellar wind, the

radius at which two pressures balance is well outside the gravitational accretion radius at all orbital phases (Kochanek 1993; Tavani et al. 1994). Parameterizing the Be stellar wind by $\Upsilon \equiv \dot{M}_{-8} v_{0,6}$, where the Be star mass-loss rate $\dot{M} \equiv (10^{-8} \text{ M}_{\odot} \text{ yr}^{-1}) \dot{M}_{-8}$, and the wind velocity at the stellar surface $v_0 \equiv (10^6 \text{ cm s}^{-1}) v_{0,6}$, Tavani et al. (1994) showed that accretion was possible near periastron only for $\Upsilon \gtrsim 10^4$ for standard pulsar wind parameters and characteristics of the Be star outflow. Under these conditions, however, accretion onto the neutron star should yield an X-ray luminosity much larger than the observed luminosity by several orders of magnitude. In conclusion accretion would be unlikely to occur even near periastron.

Based on the radio timing observations covering recent two periastron passages, Manchester et al. (1995) reported small jumps in pulse period at both periastron passages with $\Delta P/P \approx 10^{-9}$. They interpreted these jumps as being due to “propeller torques” caused by interaction between the pulsar wind and the Be stellar wind. The interpretation predicts an X-ray luminosity due to the torque much smaller than we have observed. Although we cannot rule out the interpretation with an impulsive strong Be stellar wind, dynamical effects (Kochanek 1993; Lai et al. 1995) are more likely the interpretation of the timing results. In any case, the radio result of little perturbations in the pulsar’s spin period provides additional evidence against the accretion scenario, because much larger perturbations should have been observed if accretion dominated the observed X-rays.

5.2.4 Emission from Accreted Materials Intercepted by Pulsar’s Magnetosphere

King and Cominsky (1994) proposed a model to explain the X-rays observed at the apastron as being due to release of gravitational potential energy of gaseous materials at a boundary radius where the pulsar magnetic pressure balances the ram pressure of the stellar wind. Based on this model, both the radio pulsation and the X-ray emission are expected to be detected, though accreting material within the light cylinder is expected to quench the radio emission. King and Cominsky (1994) found the boundary radius is located very close (within a factor of 2) to the light cylinder radius at apastron in this model. We note here that, although the King and Cominsky (1994) model used a dipolar magnetic field outside the light-cylinder in their pressure balance calculation, the correct $1/r$ field dependence does not change this result much.

At periastron, however, because the density of the Be stellar wind is much larger than at apastron by at least three orders of magnitude, there is no way to prevent the stellar wind from penetrating the light cylinder in this model. The penetration would result in

standard accretion, which has been already discussed in §5.2.3. We therefore conclude the King and Cominsky (1994) model is an unlikely explanation for the X-ray emission from the system.

5.2.5 Shock Emission

In a binary system containing a short period pulsar and a massive Be star, a shock is formed between two winds with a contact discontinuity at the location where the ram pressures of the two winds balance. In this scheme high-energy emission is generally expected from the shocked winds by converting the kinetic energy of the winds into high-energy photons through a process such as synchrotron emission. Based on this scheme, the kinetic energy of the pulsar wind is always larger than that of the stellar wind by a large factor of c/v at the contact discontinuity, because the momentum fluxes of the two winds are equal there. From this simple energetics argument, high energy emission from the shocked stellar wind is unlikely to dominate over that from the shocked pulsar wind. Kochanek (1993) estimated the total energy available to be radiated as high energy emission as $\sim 10^{32}$ erg s $^{-1}$ from the Be stellar wind $\sim 10^{36}$ erg s $^{-1}$ from the pulsar wind if one assumes standard stellar wind parameters. Hence the shocked pulsar wind can supply sufficient energy for the observed X-ray luminosity $L_X \sim 10^{34}$ erg s $^{-1}$, while the shocked stellar wind cannot.

The X-ray emission from the shocked pulsar wind is favored also from spectral points of view. Hoshino et al. (1992) considered a relativistic plasma consisting of thermalized electrons, positrons, and ions, and showed that acceleration in a transverse magnetohydrodynamic collisionless shock produces a non-thermal pair distribution downstream from the shock. The acceleration mechanism in this model is the pairs' cyclotron absorption of large amplitude magnetosonic waves produced by ions gyrating in the shock front. Up to $\sim 20\%$ of the ions' kinetic energy is transformed into electron/positron pairs (hereafter e^\pm pairs) through this mechanism. They showed that, in the absence of radiative losses, the pairs acquire a power law spectrum in the Lorentz factor γ , $N(\gamma) \propto \gamma^{-s}$, with $s \approx 2$ for $\gamma_1 < \gamma < \gamma_m$, where the cutoff $\gamma_m = \gamma_1 m_i / (Z m_\pm)$. Since the photon index α of synchrotron emission from such pairs is related to s with $\alpha = (s + 1)/2$, the observed photon index is expected to be $\alpha \approx 1.5$, which agrees well with the *ASCA* result in Figure 5.1 for obs4, obs5, and obs6.

In conclusion the emission from the shocked pulsar wind may explain the X-rays observed with *ASCA* presented in this thesis. Also, the synchrotron radiation from e^\pm pairs accelerated by a transverse magnetohydrodynamic collisionless shock naturally accounts for the *ASCA* spectra at large binary separations.

5.3 Shock-Powered Emission Model

From the discussions in §5.2, the shock-powered emission is favored as the mechanism for the X-ray emission from the PSR B1259–63/SS 2883 system. We now introduce how the X-ray emission occurs in the system in the context of shock the emission model.

The pulsar wind collides the stellar wind from the Be star and forms a shock between two winds (see Figure 5.3). The location of the shock is determined by pressure balance between the two winds. Assuming a spherical stellar wind with a constant velocity v , the ram pressure of the stellar wind at a distance r from the Be star, $P_{\text{SW}}(r)$, is $P_{\text{SW}}(r) = \rho(r)v^2$, where $\rho(r)$ is the mass density of the stellar wind at that distance. For the spherical stellar wind, we can easily derive $\rho(r) = \dot{M}/(4\pi r^2 v)$ with mass loss rate \dot{M} , and obtain

$$P_{\text{SW}}(r) = \frac{\dot{M}v}{4\pi r^2}.$$

For the pulsar wind we assume highly relativistic particles carry most of the kinetic energy. At a distance r from the pulsar, particles with energy E carry a momentum flux of $n(r)E/c$ traveling with a speed of light c , where $n(r)$ is the number density of the particles in the pulsar wind. Thus the contribution of the particles to the ram pressure is $n(r)E$. Letting \dot{E}_{PW} be the total energy of the pulsar wind emitted per unit time, the energy conservation law implies $n(r) = \dot{E}_{\text{PW}}/(4\pi r^2 cE)$. Hence the ram pressure of the pulsar wind at a distance r from the pulsar, $P_{\text{PW}}(r)$, can be written as

$$P_{\text{PW}}(r) = \frac{\dot{E}_{\text{PW}}}{4\pi r^2 c}.$$

Let the distance of the contact discontinuity from the pulsar be r_1 and that from the Be star be r_2 (see Figure 5.3). The pressure balance $P_{\text{PW}}(r_1) = P_{\text{SW}}(r_2)$ implies

$$\left(\frac{r_2}{r_1}\right)^2 = \frac{\dot{M}vc}{\dot{E}_{\text{PW}}} \equiv \lambda^2.$$

Defining λ as above, we obtain

$$\begin{aligned} r_1 &= \frac{1}{1+\lambda}r, \\ r_2 &= \frac{\lambda}{1+\lambda}r, \end{aligned}$$

where r is the binary separation. We note here that these formulas show that the location of the contact discontinuity scales with the binary separation for constant \dot{M} , v , and \dot{E}_{PW} .

In this shock model we can easily derive two important features of the kinetic energy of the pulsar wind poured into the shock: it is independent of the binary separation and

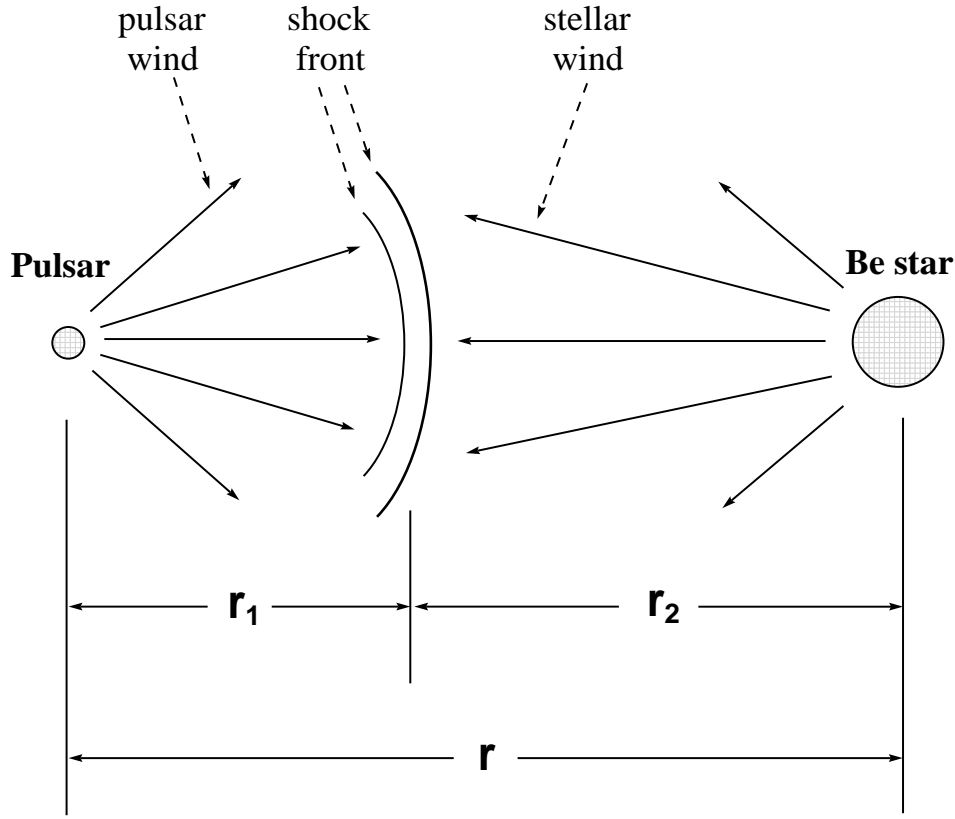


Figure 5.3: Schematic drawing of the shock formed in the PSR B1259–63/SS 2883 system.

it always dominates that of the stellar wind. Below we derive these features for further discussion.

We first show constant energy is supplied into the shock by the pulsar wind. Letting L_{PW} and L_{SW} be the kinetic energy of the pulsar wind and the stellar wind poured into the shock region, and γ_1 be the Lorentz factor of the particles just upstream the shock (which carry the kinetic energy of the pulsar wind, see Figure 5.4), we obtain

$$\begin{aligned} L_{\text{PW}} &= n(r_1)\gamma_1 mc^2 \cdot c \cdot A, \\ L_{\text{SW}} &= \rho(r_2)v^2 \cdot v \cdot A, \end{aligned}$$

where A is the total area of the shock. Since the location where the ram pressures of the two winds balance scales with the binary separation r , $A \propto r^2$. As previously discussed, $n(r_1) \propto r_1^{-2} \propto r^{-2}$. Thus $L_{\text{PW}} \propto n(r_1)A \propto r^0$ and we know the energy supplied by the pulsar wind is constant over the orbit.

We then see that the pulsar wind dominates the stellar wind on the energy supply into the shock. The pressure balance at the shock is expressed as

$$n(r_1)\gamma_1 mc \cdot c = \rho(r_2)v \cdot v.$$

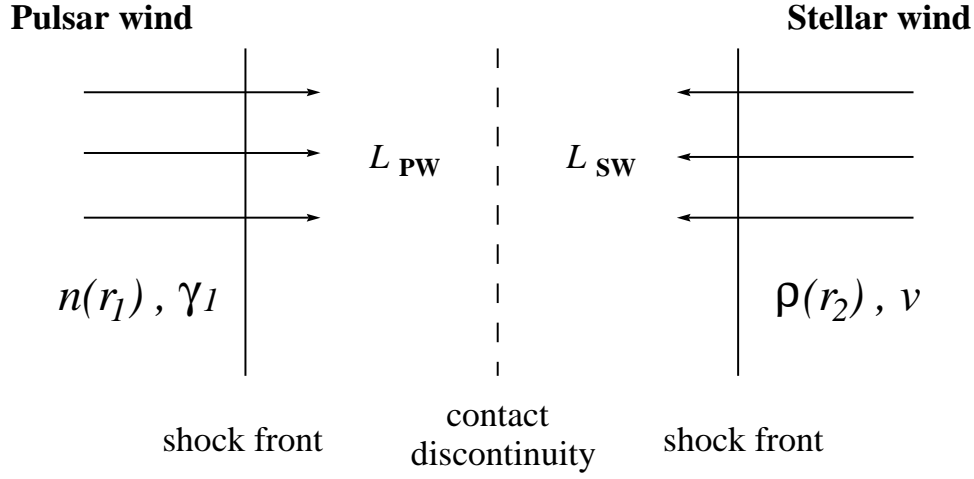


Figure 5.4: Kinetic energy of pulsar wind and stellar wind available in shocked winds.

The ratio of the energy supplied by the two winds is then

$$\begin{aligned} \frac{L_{PW}}{L_{SW}} &= \frac{n(r_1)mc\gamma_1 \cdot c \cdot A}{\rho(r_2)v^2 \cdot v \cdot A} \\ &= \frac{c}{v}. \end{aligned}$$

Since the velocity of Be stellar winds is $\sim 1000 \text{ km s}^{-2}$ (e.g. Cassinelli et al. 1994), the ratio is ~ 300 . This means the energy supply by the pulsar wind is larger than that by the stellar wind by two orders of magnitude.

5.4 Emission from the Shocked Pulsar Wind

X-rays may be emitted from e^\pm in the shocked wind by thermal bremsstrahlung, synchrotron emission, or inverse Comptonization of UV photons from the Be star. In this section we examine which may dominate the X-ray emission by estimating emission timescales of the mechanisms. Since the emission from the shocked pulsar wind always dominates that from the stellar wind as discussed in the previous section, we consider the emission from the shocked pulsar wind only.

Before considering the emission mechanisms, we first point out that the release of the wind kinetic energy must be completed within the flow time of the shocked pulsar wind. The binary separation of the system r is

$$r = \begin{cases} 9.90 \times 10^{12} \text{ cm} & \text{at periastron} \\ 1.42 \times 10^{14} \text{ cm} & \text{at apastron} \end{cases},$$

with $1.4 M_\odot$ for the neutron star mass and $10 M_\odot$ for the Be star mass assumed. Since the flow velocity of the pulsar wind behind the shock front is reduced to $c/4$ assuming a strong

shock, e^\pm pairs escape from the system within a timescale $\tau_f = r/(c/4)$, or numerically

$$\tau_f = \begin{cases} 1.32 \times 10^3 \text{ s} & \text{at periastron} \\ 1.89 \times 10^4 \text{ s} & \text{at apastron} \end{cases}.$$

Emission timescales estimated below should be compared with these values; if the timescale is less than τ_f , e^\pm pairs emit most of their kinetic energy through the emission mechanism in the shock, and otherwise, e^\pm pairs lose only part of their energy in the shock.

5.4.1 Thermal Bremsstrahlung

We first examine thermal bremsstrahlung emission. When the pulsar wind is thermalized behind the shock front, the temperature of the pair plasma reaches $kT \sim \gamma_1 m_e c^2$, where m_e is a rest mass of an electron. Here we assume protons carry most of the wind kinetic energy, then

$$\dot{E}_{\text{PW}} = n_p \cdot 4\pi r_1^2 \cdot c \cdot \gamma_1 m_p c^2,$$

where n_p is a number density of protons, m_p is the rest mass of the proton. The emission timescale for thermal bremsstrahlung, τ_b , is thus

$$\tau_b = \frac{n_p \cdot \gamma_1 m_p c^2}{\Lambda},$$

where n_e is a number density of electrons, C is the compression factor at the shock front, Λ is the energy emitted in unit time from unit volume and $\Lambda = \varepsilon_0 T^{1/2} n_e n_p C^2$ in CGS-gauss units with $\varepsilon_0 = 1.4 \times 10^{-27} \text{ erg s}^{-1} \text{ cm}^{-3}$ (Rybicki and Lightman 1979, p.162 Eq. 5.15b). We finally obtain

$$\begin{aligned} \tau_b &= \frac{4\pi C^4 \sqrt{m_p^3 k}}{\varepsilon_0} \frac{\gamma_1^{3/2}}{C^2 \dot{E}_{\text{PW}}} \left(\frac{r}{1+\lambda} \right)^2 \\ &= 1.39 \times 10^{20} \left(\frac{C}{4} \right)^{-2} \left(\frac{\dot{E}_{\text{PW}}}{\dot{E}_{\text{rot}}} \right)^{-1} \left(\frac{\gamma_1}{10^6} \right)^{3/2} \left(\frac{1}{1+\lambda} \right)^2 \left(\frac{r}{50 \text{ R}_\odot} \right)^2 \text{ s}, \end{aligned}$$

where \dot{E}_{rot} is the spin-down luminosity of the pulsar, and R_\odot is the solar radius. We use the upstream Lorentz factor $\gamma_1 = 10^6$ as a nominal value because the upstream Lorentz factor is estimated to be 10^6 for the Crab nebula by Kennel and Coroniti (1984a, 1984b) from a comparison of the wide band spectrum of the Crab nebula with numerical simulations of their shock acceleration.

We note here that the thermal bremsstrahlung emission is negligible in the system because of this large τ_b compared with τ_f . Since the shocked wind can emit only a part of the spin-down luminosity $\dot{E}_{\text{rot}} \sim 10^{35} \text{ erg s}^{-1}$ with a fraction of $\tau_f/\tau_b \sim 10^{-16}$ at

most, we can expect the thermal bremsstrahlung emission with $\sim 10^{19}$ erg s $^{-1}$, much less than observed X-ray luminosity $L_X = (0.1 - 1) \times 10^{34}$ erg s $^{-1}$. We thus exclude thermal bremsstrahlung as the dominant source of the observed X-rays.

5.4.2 Inverse Comptonization of UV Photons from the Be Star

In the PSR B1259–63/SS 2883 system UV photons are supplied by the Be star. Relativistic e^\pm pairs hit these photons and produce high-energy photons through inverse Comptonization. The emitted power per particle, P_{compt} , is

$$P_{\text{compt}} = \frac{4}{3} f_{\text{KN}} \sigma_{\text{T}} c \gamma^2 \beta^2 U_{\text{P}},$$

where γ is the Lorentz factor of e^\pm emitting inverse Compton photons, σ_{T} is the cross section for Thomson scattering, $\sigma_{\text{T}} = 6.65 \times 10^{-25}$ cm 2 , β is the velocity of e^\pm pairs normalized with the speed of light, U_{P} is the photon energy density expressed as,

$$\begin{aligned} U_{\text{P}} &= \frac{L_{\text{Be}}}{4\pi r_2^2} \\ &= \frac{L_{\text{Be}}(1 + \lambda)^2}{4\pi c \lambda^2 r^2}, \end{aligned}$$

and f_{KN} is the ratio of the Klein-Nishina cross section to the Thomson cross section (e.g. Rybicki and Lightman 1979, p.200 Eq.7.16a). According to the optical observations, the bolometric luminosity of the Be star in the optical band $L_{\text{Be}} = 5.8 \times 10^4 L_\odot$; then, the inverse Compton timescale τ_c is

$$\begin{aligned} \tau_c &= \frac{3\pi m_e c^3}{f_{\text{KN}} \sigma_{\text{T}}} \frac{\dot{M} v}{\gamma \dot{E}_{\text{PW}} L_{\text{Be}}} \left(\frac{r}{1 + \lambda} \right)^2 \\ &= 0.642 \left(\frac{f_{\text{KN}}}{1} \right)^{-1} \left(\frac{\gamma}{10^6} \right)^{-1} \left(\frac{\beta}{1} \right)^{-2} \left(\frac{\lambda}{1 + \lambda} \right)^2 \left(\frac{r}{50 R_\odot} \right)^2 \text{ s}. \end{aligned}$$

In order to consider the importance of the inverse Comptonization process as the energy source of the high-energy emission from the system, we discuss the energetics based on the derived timescales. We first assume that all the X-rays observed by *ASCA* and *OSSE* originate from the inverse Comptonization processes. Suppose that a soft photon with its energy ϵ is scattered by an electron or a positron with the Lorentz factor γ and then a photon with energy $h\nu$ is emitted from the electron or the positron. The relationship between these quantities is

$$h\nu = \gamma^2 \epsilon,$$

as plotted in Figure 5.5. Assuming the Be star has temperature $kT \sim 2 \times 10^4$ K (Cassinelli et al. 1994), we deduce a peak energy $\epsilon = 5$ eV. We then obtain $\gamma \sim 30$ for $h\nu \sim 5$ keV

representing the *ASCA* band and $\gamma \sim 140$ for $h\nu \sim 100$ keV representing the *OSSE* band. Emission timescales of the inverse Comptonization are then computed as

$$\frac{\tau_c}{\tau_f} = \begin{cases} 1.3 \times 10^2 \left(\frac{\lambda}{1+\lambda}\right)^2 & \text{for } e^\pm \text{ contributing } ASCA \text{ band} \\ 2.8 \times 10^1 \left(\frac{\lambda}{1+\lambda}\right)^2 & \text{for } e^\pm \text{ contributing } OSSE \text{ band} \end{cases}$$

The kinetic energies carried by these e^\pm in unit time, K_{e^\pm} , are evaluated from these ratios multiplied by the luminosities observed by *ASCA* ($L_X \sim 1.6 \times 10^{34}$ erg s $^{-1}$) and *OSSE* ($L_\gamma \sim 3 \times 10^{34}$ erg s $^{-1}$), respectively,

$$K_{e^\pm} = \begin{cases} 2.2 \times 10^{36} \left(\frac{\lambda}{1+\lambda}\right)^2 \text{ erg s}^{-1} & \text{for } e^\pm \text{ contributing } ASCA \text{ band} \\ 8.4 \times 10^{35} \left(\frac{\lambda}{1+\lambda}\right)^2 \text{ erg s}^{-1} & \text{for } e^\pm \text{ contributing } OSSE \text{ band} \end{cases}.$$

By summing these two kinetic energies we can obtain a lower limit of the kinetic energy of the pulsar wind as

$$\dot{E}_{PW} \gtrsim 3.0 \times 10^{36} \text{ erg s}^{-1} \left(\frac{\lambda}{1+\lambda}\right)^2.$$

Melatos et al. (1995) discussed the variation of the rotation measure and dispersion measure of PSR B1259–63 measured by the radio timing observations around the periastron passage in 1994. They concluded that the stellar wind likely dominates the pulsar wind in the momentum flux at periastron and showed $\lambda^2 \gtrsim 10$ is required to explain large variation in the dispersion measure. By combining this result with the estimate of the wind kinetic energy above, we obtain

$$\dot{E}_{PW} \gtrsim 1.7 \times 10^{36} \text{ erg s}^{-1}$$

in contradiction with the energetics, since the kinetic energy of the pulsar wind cannot exceed the spin-down luminosity $\dot{E}_{\text{rot}} = 8.28 \times 10^{35}$ erg s $^{-1}$. We therefore conclude the inverse Compton process cannot explain all the high-energy emission observed at periastron.

In addition, we can see that the inverse Comptonized X-rays are unlikely to dominate the observed X-rays as follows. Suppose that all the spin-down luminosity is carried by e^\pm pairs contributing to the X-rays observed by *ASCA* and *OSSE*. As discussed above, when we assume that all the observed X-rays originate from inverse Comptonized photons, the lower limit of the wind energy is larger than the spin-down luminosity by factor of ~ 2 . To avoid this contradiction we need to reduce the observed X-ray luminosity, or in other words, X-rays from the inverse Compton process can contribute less than a half of the observed X-rays. Considering this estimate is based on the conservative assumptions, we finally conclude the inverse Comptonization of UV photons from the Be star cannot dominate the observed X-rays and we need alternative X-ray emission mechanism such as synchrotron emission discussed in § 5.4.3.

5.4.3 Synchrotron Emission

The emission timescale τ_s of synchrotron emission is evaluated here. The emitted power per particle P_{synch} is

$$P_{\text{synch}} = \frac{4}{3} \sigma_T c \gamma^2 \beta^2 U_B,$$

where U_B is the magnetic energy density in the shocked wind (e.g. Rybicki and Lightman 1979, p.169 Eq.6.7b). The magnetic field in the shock region is parameterized by the ratio of the magnetic energy flux to the kinetic energy flux just upstream from the shock, σ . For $\sigma \ll 1$,

$$\begin{aligned} U_B &= \sigma \cdot \frac{\dot{E}_{\text{PW}}}{4\pi r_1^2} \cdot c^{-1} \\ &= \frac{\sigma(1+\lambda)^2 \dot{E}_{\text{PW}}}{4\pi c r^2}, \end{aligned}$$

then we obtain

$$\begin{aligned} \tau_s &= \frac{3\pi m_e c^2}{\sigma_T} \frac{1}{C^2 \gamma \dot{E}_{\text{PW}} \sigma} \left(\frac{r}{1+\lambda} \right)^2 \\ &= 9.4 \times 10^2 \left(\frac{C}{4} \right)^{-2} \left(\frac{\dot{M}}{10^{-8} \text{ M}_\odot \text{ yr}^{-1}} \right)^{-1} \left(\frac{v}{1000 \text{ km s}^{-1}} \right)^{-1} \left(\frac{\sigma}{0.005} \right)^{-1} \\ &\quad \times \left(\frac{\gamma}{10^6} \right)^{-1} \left(\frac{\beta}{1} \right)^{-2} \left(\frac{\lambda}{1+\lambda} \right)^2 \left(\frac{r}{50 \text{ R}_\odot} \right)^2 \text{ s}, \end{aligned}$$

We use $\sigma = 0.005$ as a nominal value because Kennel and Coroniti (1984a, 1984b) showed $\sigma \approx 0.005$ for the Crab nebula.

We note here that the Lorentz factor of e^\pm pairs emitting X-rays is much higher than in the case of the inverse Comptonization. Synchrotron power from e^\pm pairs with the Lorentz factor γ peaks at $0.29h\nu_c$, where

$$h\nu_c = \frac{3\hbar\gamma^2 e B \sin \alpha}{2mc},$$

B is the magnetic field strength, and α is a “pitch angle”, which is the angle between the magnetic field and the velocity of e^\pm . Letting $\sin \alpha = 2/\pi$ and energy of the synchrotron X-ray be 5 keV, $\gamma \sim 1.7 \times 10^6$ at periastron and $\gamma \sim 6.5 \times 10^6$ at apastron. The emission timescale τ_s for these pairs is

$$\frac{\tau_s}{\tau_f} = \begin{cases} 3.4 \left(\frac{\dot{M}}{10^{-8} \text{ M}_\odot \text{ yr}^{-1}} \right)^{-1} \left(\frac{v}{1000 \text{ km s}^{-1}} \right)^{-1} \left(\frac{\sigma}{0.005} \right)^{-1} \left(\frac{C}{4} \right)^{-2} \left(\frac{\lambda}{1+\lambda} \right)^2 & \text{at periastron} \\ 13 \left(\frac{\dot{M}}{10^{-8} \text{ M}_\odot \text{ yr}^{-1}} \right)^{-1} \left(\frac{v}{1000 \text{ km s}^{-1}} \right)^{-1} \left(\frac{\sigma}{0.005} \right)^{-1} \left(\frac{C}{4} \right)^{-2} \left(\frac{\lambda}{1+\lambda} \right)^2 & \text{at apastron} \end{cases}.$$

Here we can see synchrotron emission can produce the observed X-ray luminosity because the small τ_s/τ_f at periastron means the kinetic energy of the pulsar wind is

converted into X-rays with high efficiency through the synchrotron emission. Note that τ_s/τ_f stays small even with $\lambda^2 \gtrsim 10$ at periastron. In other words, in the shock region the synchrotron emission can convert the spin-down luminosity into high-energy photons with efficiency high enough to account for the observed X-ray luminosity.

In addition, synchrotron emission can reproduce the power law nature of the observed X-ray spectra. From e^\pm pairs whose energy spectrum is $N(\gamma) = \gamma^{-s}$, a power law spectrum with photon index $\alpha = (s + 1)/2$ is expected (e.g. Rybicki and Lightman 1979). In this context the observed X-ray spectra $\alpha \sim 1.5$ can be explained by the synchrotron X-rays from e^\pm pairs with $s \sim 2$. As a conclusion the synchrotron emission from the shocked pulsar wind is the most likely source of the observed X-rays.

5.5 Interpretation of Observed Features

We observed two significant features of the X-ray emission from the system; softening of the spectrum at the periastron passage and variability in X-ray luminosity. In this section we argue how these two features are interpreted in the scheme of synchrotron emission from the shocked pulsar wind.

5.5.1 Spectral Softening at Periastron

Although we concluded the inverse Compton process is unimportant as an emission mechanism of the observed X-rays, the process may be the most important to cool e^\pm pairs. Various emission timescales are plotted in the upper panel in Figure 5.5 for a wide range of the Lorentz factor γ with the flow time of the shocked pulsar wind. For the figure we assume stellar wind parameters $\dot{M} = 10^{-8} M_\odot \text{ yr}^{-1}$ and $v = 1000 \text{ km s}^{-1}$, which yield $\lambda = 1.51$. In the lower panel in the figure the relationship between the Lorentz factor of an electron/positron and the energy of emitted photon from the electron/positron is shown. As is clear from Figure 5.5, the inverse Compton emission timescale is shorter than that of the synchrotron emission for wide range of the Lorentz factor up to $\gamma \sim 10^9$. This means, for a single electron or positron with $\gamma \lesssim 10^9$, inverse Compton cooling is more efficient than the synchrotron cooling.

The spectral softening near the periastron passage can be interpreted as due to the inverse Compton cooling. At periastron, because the binary separation is smallest, the shock region is closest to the Be star. This means inverse Compton cooling by soft photons from the Be star is most significant at the periastron. As the pulsar moves away from the Be star, the distance of the shock region from the Be star increases and inverse Compton cooling will be less effective.

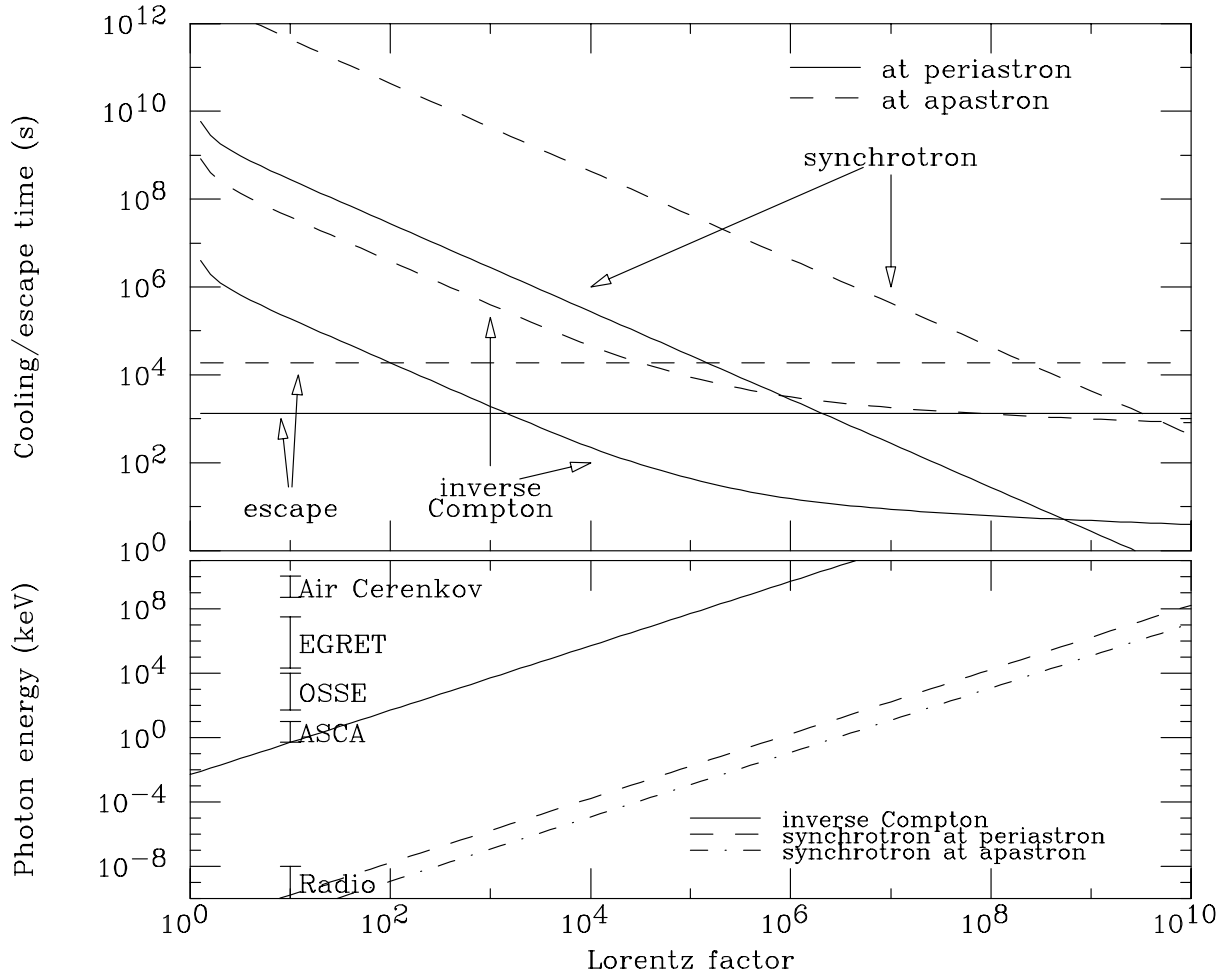


Figure 5.5: (upper panel) Timescales of synchrotron cooling and inverse Compton cooling are plotted with the escape time in the system. For the figure we assume stellar wind parameters $\dot{M} = 10^{-8} M_{\odot} \text{ yr}^{-1}$ and $v = 1000 \text{ km s}^{-1}$, which yield $\lambda = 1.51$. (lower panel) Relationship between the Lorentz factor of an electron/positron and the energy of an emitted photon from the electron/positron. In the panel mission names are written next to vertical bars which indicate energy band of the mission.

In order to illustrate this scheme quantitatively let us assume the e^{\pm} pairs are accelerated immediately downstream of the shock front in a shorter time than the inverse Compton cooling time and distribute in a power law spectrum there. For spectral variation of energy distribution of e^{\pm} pairs, we employ the well-known quasi-linear kinetic equation (Sagdeev and Galeev 1969; Melrose 1980; Melrose 1986). Letting $N(\gamma, x)d\gamma$ be the number of electrons and positrons with the Lorentz factor γ at a distance x from the shock front, $N(\gamma, x)d\gamma$ satisfies

$$v \frac{\partial N}{\partial x} = \frac{2}{3} \frac{\partial}{\partial \gamma} (f \gamma^2 N),$$

where $f = 16\pi f_{\text{KN}} e^4 / 3m_e^2 c^3$. For simplicity we regard f_{KN} as independent of γ , although

$f \propto \log \gamma/\gamma$ for $\gamma \gtrsim 10^6$ in reality. The evolution of the energy spectrum can be obtained by solving this equation under the boundary condition

$$N(\gamma, 0) = N_0 \gamma^{-s} H(\gamma_{\max} - \gamma),$$

where N_0 is a normalization factor, γ_{\max} is the maximum Lorentz factor of the pairs achieved in the shock acceleration, and H is the Heaviside function which exhibits a high energy cut off. We observe the integral of the evolving spectra, $N_{\text{obs}}(\gamma) = \int_0^{x_{\max}} N(\gamma, x) dx$, where x_{\max} is the size of the shock region. We finally obtain for $s \neq -1$,

$$N_{\text{obs}}(\gamma) = \begin{cases} \left(\frac{\gamma_{\max}}{s+1} \right) \left(\frac{x_c}{x_{\max}} \right) \left\{ \left(1 - \frac{\gamma}{\gamma_{\max}} \frac{x_{\max}}{x_c} \right)^{s-1} - 1 \right\} \gamma^{-s-1} & \text{for } \gamma/\gamma_{\max} < x_c/(x_c + x_{\max}), \\ \left(\frac{\gamma_{\max}}{s+1} \right) \left(\frac{x_c}{x_{\max}} \right) \left\{ \left(\frac{\gamma}{\gamma_{\max}} \right)^{s-1} - 1 \right\} \gamma^{-s-1} & \text{otherwise,} \end{cases}$$

where x_c is the inverse Compton loss length. The cooled spectrum, $N_{\text{obs}}(\gamma)$, is illustrated in Figure 5.6. The spectrum breaks at a critical Lorentz factor γ_c , determined by solving for $\gamma_c/\gamma_{\max} = x_c/(x_c + x_{\max})$, so that the inverse Compton loss length becomes comparable to the size of the shock region at $\gamma \sim \gamma_c$, or in other words, τ_c becomes comparable with τ_f at $\gamma \sim \gamma_c$. As indicated in the figure, the spectral index of e^\pm pairs increases by one from s to $(s + 1)$ around $\gamma \sim \gamma_c$ due to the inverse Compton cooling.

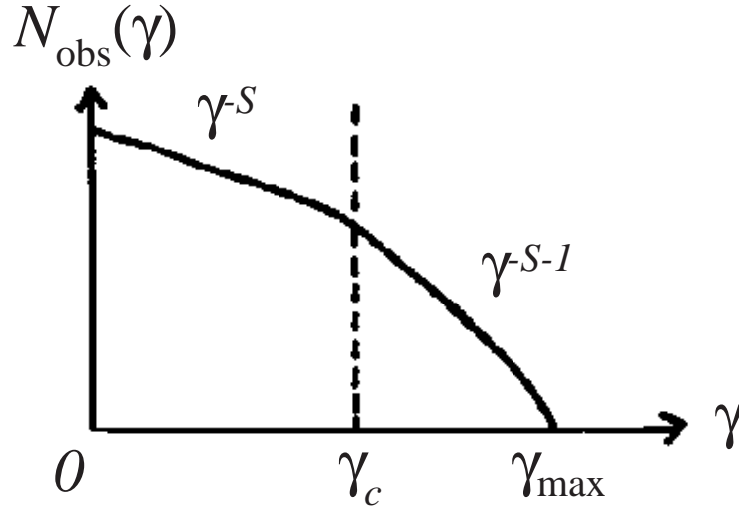


Figure 5.6: Schematic drawing of the integrated spectrum of e^\pm pairs' energy distribution.

Now we can consider the spectral softening observed at periastron. The observed photon index α is approximately 1.6 at apastron, gradually increases as the binary separation decreases, and approaches $\alpha \sim 2.0$ at periastron. When the electron's energy distribution just behind the shock front is $s \sim 2$, this variation can be interpreted as the effect of inverse Compton cooling in a scheme described above. Since the observed X-rays were

emitted by e^\pm pairs with $\gamma \sim (2-7) \times 10^6$, if inverse Compton cooling is not effective for the pairs, γ_c is so large that $\gamma_c \gtrsim 10^7$, the pairs' spectrum is unchanged with $s \sim 2$, then we will observe X-ray spectrum with $\alpha \sim 1.5$ ($s \sim 2$). On the other hand, if the cooling is efficient for the pairs, γ_c becomes so small that $\gamma_c \lesssim 10^6$, the pairs' spectrum becomes soft with $s \sim 3$, then we will observe a spectrum with $\alpha \sim 2.0$.

We therefore conclude that the change in the photon indexes of the observed X-ray spectra are due to inverse Compton cooling of the e^\pm pairs emitting the observed X-rays. The observed photon index can be explained by assuming that the the pairs have spectral index $s \sim 2$ just behind the shock front and that the cooling is very efficient at periastron while it does not influence the pairs. The detection of a soft index $\alpha \sim 2$ is evidence for radiative cooling by the inverse Compton interaction in the system.

5.5.2 Variability in Observed Luminosity

As seen in Figure 5.2, the observed luminosities range from $\sim 10^{34}$ erg/s near periastron to $\sim 10^{33}$ erg/s near apastron, while Figure 5.1 shows constant photon index when the pulsar is farther than ~ 1000 light second from the Be star. The constant photon index suggests that the emission mechanism and the cooling process does not change much. Hence we have two possibilities to explain this situation: e^\pm pairs may flow out from the system in a shorter time than the synchrotron emission timescale τ_s , or the kinetic energy poured into the shock region may decrease near apastron.

We consider the first possibility, the escape of e^\pm pairs. The ratio of the synchrotron emission timescale τ_s over the flow time τ_f is derived in §5.4.3 as

$$\frac{\tau_s}{\tau_f} = \begin{cases} 3.4 \left(\frac{\dot{M}}{10^{-8} \text{ M}_\odot \text{ yr}^{-1}} \right)^{-1} \left(\frac{v}{1000 \text{ km s}^{-1}} \right)^{-1} \left(\frac{\sigma}{0.005} \right)^{-1} \left(\frac{C}{4} \right)^{-2} \left(\frac{\lambda}{1+\lambda} \right)^2 & \text{at periastron} \\ 13 \left(\frac{\dot{M}}{10^{-8} \text{ M}_\odot \text{ yr}^{-1}} \right)^{-1} \left(\frac{v}{1000 \text{ km s}^{-1}} \right)^{-1} \left(\frac{\sigma}{0.005} \right)^{-1} \left(\frac{C}{4} \right)^{-2} \left(\frac{\lambda}{1+\lambda} \right)^2 & \text{at apastron} \end{cases}.$$

Setting $\dot{M} = 10^{-8} \text{ M}_\odot \text{ yr}^{-1}$, $v = 1000 \text{ km s}^{-1}$, and $\dot{E}_{\text{PW}} = \dot{E}_{\text{rot}} = 8.28 \times 10^{35} \text{ erg s}^{-1}$, we obtain $\lambda = 1.51$. The Lorentz factor of e^\pm pairs emitting X-rays is $\gamma \sim 1.7 \times 10^6$ at periastron and $\gamma \sim 6.5 \times 10^6$ at apastron as discussed in §5.4.3, then we finally obtain

$$\frac{\tau_s}{\tau_f} = \begin{cases} 1.2 & \text{at periastron} \\ 4.7 & \text{at apastron} \end{cases}.$$

Therefore, the pairs can emit most of the kinetic energy at periastron, while they can release ~ 20 % of their energy at apastron. In this scheme, however, the decrease of the X-ray luminosity by one order of magnitude cannot be fully explained. This implies that the energy supply into the shock region should decrease at apastron, although the simple

shock-powered emission model predicts the kinetic energy poured into the shock region remains constant independent of the orbital separation of the system (see § 5.3).

As discussed in §5.3, the large variability in Figure 5.2 can not be understood in a model assuming a spherically symmetric stellar wind with constant velocity. Even if one assumes a strong equatorial wind for the Be star, the model can be applied for that case by modifying the interpretation of mass loss rate of the Be star as long as the pulsar orbits in the equatorial plane; we just redefine \dot{M} from the wind density ρ on the equatorial plane at the distance r from the Be star so that $\dot{M} = 4\pi r^2 \rho v$. Thus, again no variation in luminosity is expected. These facts strongly suggest misalignment of the pulsar's orbit with the Be star's equatorial plane. Here we should note, in the shock-powered emission model, the luminosity from the shocked pulsar wind depends on the mass loss rate of the Be star along the orbital plane of the pulsar. In other words, variations in X-ray luminosity directly reflect the density of the stellar wind around the pulsar.

The misalignment is parameterized by an orbital dependent λ . In this scheme λ is no longer constant and depends on the orbital phase. Since the geometry of the system changes when λ changes, the solid angle Ω viewing the shock region from the pulsar changes with λ . The relationship between λ and Ω is given by $\Omega = 2\pi(1 - \cos \theta)$ where θ is half of the viewing angle of the shock region from the pulsar, as illustrated in Figure 5.7, and by an analytic formula by Eichler and Usov (1993) approximating numerical calculations of colliding stellar winds by Girard and Willson (1987),

$$\theta \simeq 2.1 \left(1 - \frac{\lambda^{4/5}}{4} \right) \lambda^{2/3}.$$

By calculating Ω for λ ranging from 0 to 1, corresponding to the case in which the pulsar wind dominates the stellar wind in momentum flux, we obtain a simple relationship

$$\Omega \sim 2\pi\lambda.$$

In the case λ is greater than unity, on the other hand, $\Omega \sim 2\pi$ is expected, since the stellar wind dominates the pulsar wind.

Because ~ 20 % decrease of the X-ray luminosity can be explained by the e^\pm escape from the shock region, we need to reduce the solid angle of the shock region by factor of two at apastron, $\Omega \sim \pi$, thus $\lambda \sim 0.5$. This requires

$$\frac{\dot{M}}{10^{-8} \text{ M}_\odot \text{ yr}^{-1}} \frac{v}{1000 \text{ km s}^{-1}} \sim 0.1$$

with $\dot{E}_{\text{PW}} = \dot{E}_{\text{rot}}$ assumed, and these parameters remain realistic.

In summary we can interpret the luminosity variation due to the combination of two effects: the e^\pm pairs escape from the system, and the change in the shock geometry in the

system due to the misalignment of the pulsar's orbit with respect to the equatorial plane of the Be star. Based on this point of view, Figure 5.2 can be interpreted as the cross section of the density distribution of the stellar wind with orbit of the pulsar. In line with this scheme, the nature of the Be stellar wind are further discussed below in §5.6.1.

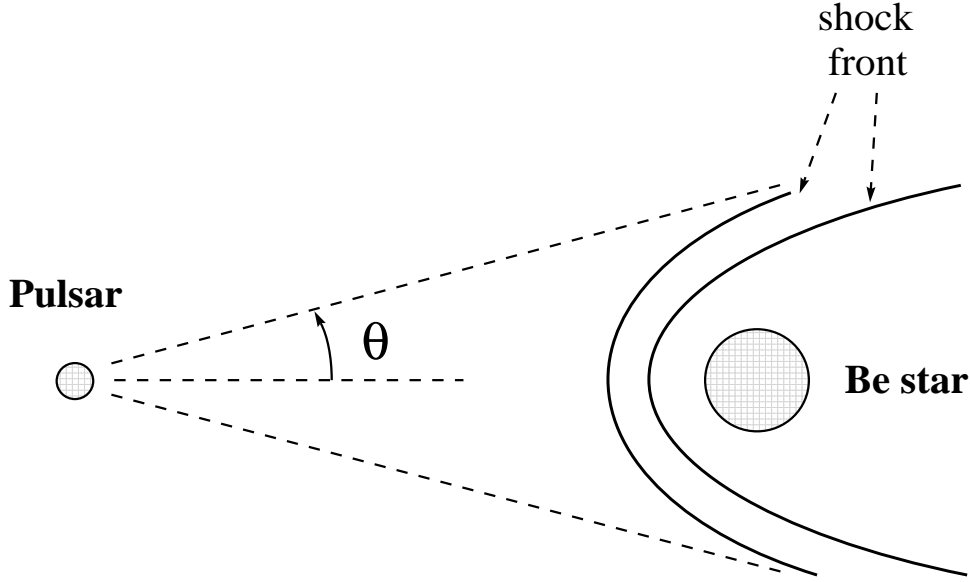


Figure 5.7: Viewing angle of the shock region from the pulsar.

5.6 Constraint on the System Parameters

In this section we show constraints on parameters of the pulsar wind and the stellar wind from the observational facts obtained in this thesis on the basis of the shock-powered emission model.

5.6.1 Structure of the Stellar Wind

We again consider the decrease of the X-ray luminosity at apastron in detail, although the rough consideration in §5.5.2 seems to succeed to explain the decrease. Here we take obs4 as a “brighter phase” and obs5 and obs6 as a “fainter phase” because these three observations show almost the same photon index $\alpha \sim 1.6$, but a significant change in flux by a factor of ~ 10 . For simplicity and clarity, quantities at the brighter phase are indicated by a subscript “bright” and those at the fainter phase “faint” in this section.

Here let us derive generalized form of τ_s/τ_f for the observed X-rays with energy $h\nu$.

By solving $h\nu = 0.29\omega_c$ about γ , where $\omega_c = 3\gamma^2 eB \sin \alpha / 2m_e c$, we obtain

$$\gamma = C^{-1/2} \left(\frac{2m_e c h \nu}{0.87 \hbar e \sin \alpha} \right)^{1/2} \left(\frac{c}{2\sigma \dot{E}_{\text{rot}}} \right)^{1/4} \left(\frac{r}{1+\lambda} \right)^{1/2},$$

and then,

$$\begin{aligned} \frac{\tau_s}{\tau_f} &= \frac{2.8\pi^{1/2} m_e^{1/2} c^{9/4} e^{1/2} (\sin \alpha)^{1/2}}{8\sigma_{\text{T}}} \frac{1}{C^{3/2} \dot{E}_{3/4} \sigma^{3/4}} \frac{r^{1/2}}{(1+\lambda)^{3/2}} \frac{1}{\nu^{3/2}} \\ &= 3.02 \left(\frac{C}{4} \right)^{-3/2} \left(\frac{\dot{E}_{\text{PW}}}{\dot{E}_{\text{rot}}} \right)^{-3/4} \left(\frac{\sigma}{0.005} \right)^{-3/4} \left(\frac{1}{1+\lambda} \right)^{3/2} \left(\frac{h\nu}{2 \text{ keV}} \right)^{-1/2} \left(\frac{r}{50 \text{ R}_{\odot}} \right). \end{aligned}$$

Note that τ_s/τ_f may depend the binary separation r only through λ and r itself.

On the basis of our model, the decrease in the X-ray luminosity can be caused by only two factors: competition of the synchrotron emission and the escape from the system, τ_s/τ_f , and the solid angle of the shock region, Ω . Because the emission efficiency saturates when $\tau_s/\tau_f \lesssim 1$, the ratio of synchrotron emissivity can be written as

$$\frac{\max(1, (\tau_s/\tau_f)_{\text{faint}})}{\max(1, (\tau_s/\tau_f)_{\text{bright}})}.$$

The solid angle of the shock region can roughly be estimated as

$$\Omega = \begin{cases} 2\pi\lambda & 0 \leq \lambda \leq 1 \\ 2\pi & 1 \leq \lambda \end{cases}$$

and the ratio of the solid angles is

$$\frac{\min(1, \lambda_{\text{bright}})}{\min(1, \lambda_{\text{faint}})}.$$

Therefore ratio of the observed luminosities is

$$\frac{L_{\text{bright}}}{L_{\text{faint}}} = \frac{\max(1, (\tau_s/\tau_f)_{\text{faint}})}{\max(1, (\tau_s/\tau_f)_{\text{bright}})} \times \frac{\min(1, \lambda_{\text{bright}})}{\min(1, \lambda_{\text{faint}})}.$$

By substituting τ_s/τ_f with the generalized form derived above, this formula relates λ_{faint} to λ_{bright} . The values $\lambda_{\text{faint}} = \lambda$ for obs5 and obs6 are plotted against λ_{bright} in the upper panel in Figure 5.8. We can see λ_{faint} is much less than unity for wide range of λ_{bright} . In the lower panel in the figure is shown the ratio of λ^2 of the bright phase and the faint phase, which is equal to the ratio of $\dot{M}v$ of the two phases. The plot indicates the ratio cannot exceed 0.1 for wide range of λ_{bright} . This means $\dot{M}v$ varies with respect to orbital phase, or in other words, this is the evidence that the pulsar's orbit is misaligned against the Be stellar wind disk. We should note here this conclusion does not depend on other parameters of the wind, such as \dot{E}_{PW} and σ .

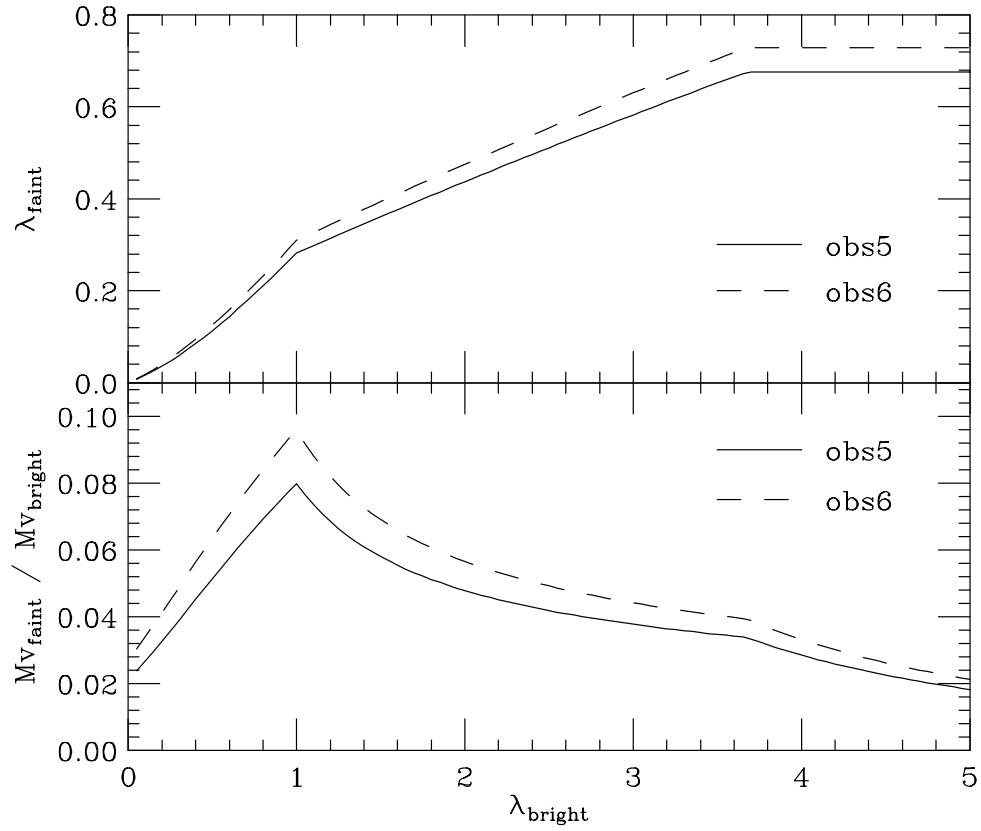


Figure 5.8: (upper panel) Relationship between λ_{bright} and λ_{faint} . The observed data in obs4 is used for the bright phase and in obs5 and obs6 for the faint phase. (lower panel) Ratios of $\dot{M}v$ of the faint phase over that of bright phase.

In conclusion the pulsar wind dominates the stellar wind in momentum flux since λ is smaller than unity near apastron based on our model. If one notes the stellar wind likely dominates the pulsar wind at periastron based on measurements of rotation measure and dispersion measure by the radio timing observation (Melatos et al. 1995), the location of the shock region moves from near the pulsar at periastron to near the Be star at apastron. In addition, based on our model, the observed decrease in the X-ray luminosity is evidence for a misalignment of the pulsar's orbit with the Be star's equatorial plane. This conclusion does not depend on the other wind parameters.

5.6.2 Kinetic Energy of the Pulsar Wind

As concluded in §5.5.1, inverse Compton cooling is unimportant near apastron, although it is efficient near periastron. In order to realize this situation, the e^\pm pairs must escape from the emission region of X-rays in a shorter time than the cooling time τ_c . Because the flow velocity of the post-shock pulsar wind is $c/4$ for the compression factor $C = 4$, the size of the shocked pulsar wind must be smaller than $\tau_c c/4$. The cooling time of e^\pm

emitting 2 keV photons is 2.2×10^3 s, obtained in the same manner as in §5.4.2, and the size of the shocked region d is less than 1.6×10^{13} cm, or $d/r \lesssim 0.11$. As concluded in §5.6.1, λ is less than unity at apastron with the pulsar wind dominating the stellar wind, and so the viewing angle of the shock region from the pulsar, θ , satisfies $\tan \theta \sim d/r$ (see Figure 5.7). The solid angle of the shocked region viewing from the pulsar, then, is $\Omega = 2\pi(1 - \cos \theta) \lesssim 3.1 \times 10^{-2}$ str. Since the observed X-ray luminosity cannot exceed the kinetic energy poured into the shocked region, we obtain a relation

$$L_X \leq \frac{\Omega}{\dot{E}_{\text{PW}}},$$

then, by substituting $L_X \sim 10^{33}$ erg s $^{-1}$ and using $\Omega \lesssim 3.1 \times 10^{-2}$,

$$\begin{aligned} \dot{E}_{\text{PW}} &\geq \frac{4\pi L_X}{\Omega} \\ &\gtrsim 4.1 \times 10^{35} \text{ erg s}^{-1}, \end{aligned}$$

or,

$$\frac{\dot{E}_{\text{PW}}}{\dot{E}_{\text{rot}}} \gtrsim 0.49.$$

In other words, more than half of the spin-down luminosity is converted into the kinetic energy of the pulsar wind in this binary system, although only a percent of the energy is emitted as X-rays.

This constraint is valid for $\lambda \leq 1.51$, although it is estimated for a standard set of stellar wind parameters with $\lambda = 1.51$. If λ is smaller than 1.51, the shock approaches the Be star, and the inverse Compton cooling becomes faster. This requires the smaller size of the emission region and hence smaller Ω , resulting in larger \dot{E}_{PW} . Therefore, for any $\lambda \leq 1.51$, $\dot{E}_{\text{PW}}/\dot{E}_{\text{rot}} \gtrsim 0.49$.

In case of the Crab nebula, over 90% of its spin-down luminosity is observed in a wide energy band ranging from radio wavelengths to high-energy γ -rays. Most of the energy is carried away from the pulsar by the pulsar wind and converted efficiently into high-energy emission. In case of the PSR B1259–63/SS 2883 system, although the pulsar wind carries most of the spin-down luminosity as in the Crab case, a much smaller fraction of the kinetic energy is converted into radiation than in the case of the Crab. This is easily understood when we remember that only a small fraction of the pulsar wind can collide with the Be stellar wind, while the Crab pulsar is surrounded in almost all the directions by the shocked materials. Indeed our estimation $\Omega \lesssim 3.1 \times 10^{-2}$ suggests that only a few percent of the kinetic energy can be released by colliding the pulsar's surroundings.

5.6.3 Momentum Flux of the Stellar Wind

An upper limit on the momentum flux of the stellar wind $\dot{M}v$ can be easily obtained from the discussion in §5.6.1. Because $\lambda \lesssim 0.8$ at apastron from the upper panel in Figure 5.8, $\dot{M}v \equiv \lambda^2 \cdot \dot{E}_{\text{PW}}/c \leq \lambda^2 \cdot \dot{E}_{\text{rot}}/c$. We then obtain, at apastron,

$$\left(\frac{\dot{M}}{10^{-8} \text{ M}_{\odot} \text{ yr}^{-1}} \right) \left(\frac{v}{1000 \text{ km s}^{-1}} \right) \lesssim 0.28.$$

For a lower limit on $\dot{M}v$, we need further a consideration on the conversion of the kinetic energy of the pulsar wind into radiation. In our model we can estimate an upper limit on the solid angle Ω of the shock region by

$$\begin{aligned} \Omega &\geq \frac{4\pi L_{\text{X}}}{\dot{E}_{\text{rot}}} \\ &= 1.5 \times 10^{-2} \end{aligned}$$

at apastron, because the kinetic energy of the pulsar wind cannot exceed the spin-down luminosity. This gives a lower limit on the size of the emission region d as $d/r_1 = \tan \theta \geq 6.9 \times 10^{-2}$, where r_1 is the distance of the shock region from the pulsar. On the other hand, because the inverse Compton cooling is inefficient at apastron, $d \leq \tau_c c/4$, then

$$\begin{aligned} \frac{d}{r_1} &= \frac{3\pi m_e c^3}{4f_{\text{KN}}\sigma_{\text{T}}\gamma L_{\text{Be}}} \left(\frac{\lambda}{1+\lambda} \right)^2 \frac{r^2}{r_1} \\ &= 5.6 \times 10^4 \frac{1}{f_{\text{KN}}\gamma} \frac{\lambda^2}{1+\lambda} \end{aligned}$$

at apastron. By combining two constraints on d/r_1 , we can obtain

$$\frac{\lambda^2}{1+\lambda} \geq 1.2 \times 10^{-6} f_{\text{KN}}\gamma$$

at apastron. By solving this for $\gamma \sim 10^6$, we obtain $\lambda \geq 0.45 \equiv \lambda_{\text{min}}$.

Let us convert this constraint into the mass loss rate and the stellar wind velocity. By definition, $\dot{M}vc/\dot{E}_{\text{PW}} = \lambda^2 \geq \lambda_{\text{min}}^2$. As is discussed in §5.6.2, $\dot{E}_{\text{PW}}/\dot{E}_{\text{rot}} \leq 0.5$ for λ smaller than 1.51. Then we now set a lower limit of $\dot{M}v$ as $\dot{M}v \geq \lambda_{\text{min}}^2 \cdot 0.5\dot{E}_{\text{rot}}/c$ or,

$$\left(\frac{\dot{M}}{10^{-8} \text{ M}_{\odot} \text{ yr}^{-1}} \right) \left(\frac{v}{1000 \text{ km s}^{-1}} \right) \gtrsim 0.05.$$

In summary, we obtained a constraint on the stellar wind momentum at apastron,

$$0.05 \lesssim \left(\frac{\dot{M}}{10^{-8} \text{ M}_{\odot} \text{ yr}^{-1}} \right) \left(\frac{v}{1000 \text{ km s}^{-1}} \right) \lesssim 0.28.$$

We note here, because $0.45 \lesssim \lambda \lesssim 0.8$ at apastron, the pulsar wind dominates the stellar wind in their momentum at apastron.

5.7 Future Studies of the System

Last, we show the possible and important studies on the PSR B1259–63/SS 2883 system. Eventually, we will discuss limitations on theoretical models of the shock acceleration obtained from the investigation described in this thesis, and the possibility of detection of the 511 keV annihilation line. At the end of this section, we stress the importance of observations of unpulsed emission from the system in the radio band and in the TeV γ -ray band.

5.7.1 Shock Acceleration Mechanism

As is seen in Figure 5.5, the inverse Compton cooling occurs for on the order of ~ 100 s for e^\pm pairs with $\gamma \gtrsim 10^6$, whose synchrotron emission dominates the observed X-rays. Since we observed X-rays from the system, the pairs with $\gamma \gtrsim 10^6$ should be produced by efficient acceleration just behind the shock front. Indeed, the *OSSE* detection revealed that the pairs should be accelerated by more than a factor of 10 (Grove et al. 1995).

The timescale of the acceleration is limited by the inverse Compton timescale τ_c . The shock acceleration for this system is required to be faster than $\tau_c \sim 100$ s. For example, shock heating through Coulomb collisions are too slow to overcome the fast cooling by the inverse Compton effect. Masai (1984) showed the collision timescale between electrons is

$$t_{e-e} = 4.8 \times 10^5 T_e^{3/2} (n_e \ln \Lambda)^{-1},$$

where T_e is temperature of the electrons in units of eV, and n_e is the number density of the electrons in units of cm^{-3} , and between protons and electrons

$$t_{e-p} = 3.1 \times 10^8 T_e^{3/2} (n_e \ln \Lambda)^{-1},$$

where $\ln \Lambda \approx 24.8 + \ln(T_e n_e^{-1/2})$. By assuming a plasma cloud consisting of the same number of electrons and protons and that all the spin-down luminosity is used to thermalize e^\pm pairs, we obtain $t_{e-e} \sim 10^{12}$ s and $t_{e-p} \sim 10^{15}$ s, much longer than $\tau_c \sim 100$ s. On the other hand, the magnetohydrodynamic collisionless shock proposed by Hoshino et al. (1992) accelerates e^\pm pairs in a much shorter time. The acceleration timescale τ_a is estimated as a timescale of the gyration of protons Ω_p behind the shock front,

$$\begin{aligned} \tau_a &\sim \Omega_p \\ &= \frac{\gamma m_p c}{eB} \\ &= \frac{\gamma m_p c}{Ce} \left(\frac{c}{2\sigma \dot{E}_{\text{PW}}} \right) \left(\frac{r}{1+\lambda} \right) \end{aligned}$$

$$= 1.7 \times 10^2 \left(\frac{C}{4}\right)^{-1} \left(\frac{1}{1+\lambda}\right) \left(\frac{\gamma}{10^6}\right) \left(\frac{\sigma}{0.005}\right)^{-1/2} \left(\frac{\dot{E}_{\text{PW}}}{\dot{E}_{\text{rot}}}\right)^{-1/2} \left(\frac{r}{50 \text{ L}_{\odot}}\right).$$

The timescale τ_a comparable to τ_c implies that shock acceleration in this scheme may be occurring in the system.

5.7.2 Possibility of the Detection of Annihilation Line Emission

Since the pulsar wind is believed to include a huge number of positrons, annihilation line emission is expected from the system. In order to evaluate the possibility of the detection of 511 keV line emission with conventional missions, we assume electrons and positrons in the pulsar wind carry a fraction r of the spin-down luminosity with the Lorentz factor γ_1 . The number of positrons N can be estimated by

$$2N \cdot \gamma m_e c^2 = r \dot{E}_{\text{PW}},$$

then flux of 511 keV γ -rays at the earth is

$$\begin{aligned} F &= \frac{2N}{4\pi d^2} \\ &= \frac{1}{4\pi d^2} \frac{r \dot{E}_{\text{PW}}}{\gamma m_e c^2} \\ &= 2.1 \times 10^{-9} \left(\frac{\gamma}{10^6}\right)^{-1} \left(\frac{d}{2 \text{ kpc}}\right)^{-2} \left(\frac{r}{1}\right) \left(\frac{\dot{E}_{\text{PW}}}{\dot{E}_{\text{rot}}}\right) \text{ s}^{-1} \text{ cm}^{-2}, \end{aligned}$$

where d is the distance to the system. Since conventional γ -ray detectors, such as *CGRO/OSSE* and *ASTRO-E/HXD* has the sensitivity between $10^{-4} \sim 10^{-5}$, it seems to be impossible to detect the annihilation line emission from the system.

5.7.3 Observations at Other Wavelengths

Observations of the shocked pulsar wind in the PSR B1259–63/SS 2883 system are reported in a few cases; the radio timing observations (Johnston et al. 1992b; Johnston et al. 1994; Manchester et al. 1995), *ROSAT* X-ray observations (Cominsky et al. 1994; Greiner et al. 1995), *OSSE* γ -ray observations (Grove et al. 1995), and the *ASCA* observations (Kaspi et al. 1995b; this thesis). From these publications the wide band spectrum is shown in Figure 5.9. The energy flux in the radio band is the pulsed component only. Unpulsed radio emission from the system has not yet been published. The spectra of the Crab pulsar and the Crab nebula are shown in Figure 5.10 for comparison. As is clear from the figure, the unpulsed radio spectrum of the PSR B1259–63/SS 2883 system is very important to compare the system with the Crab pulsar.

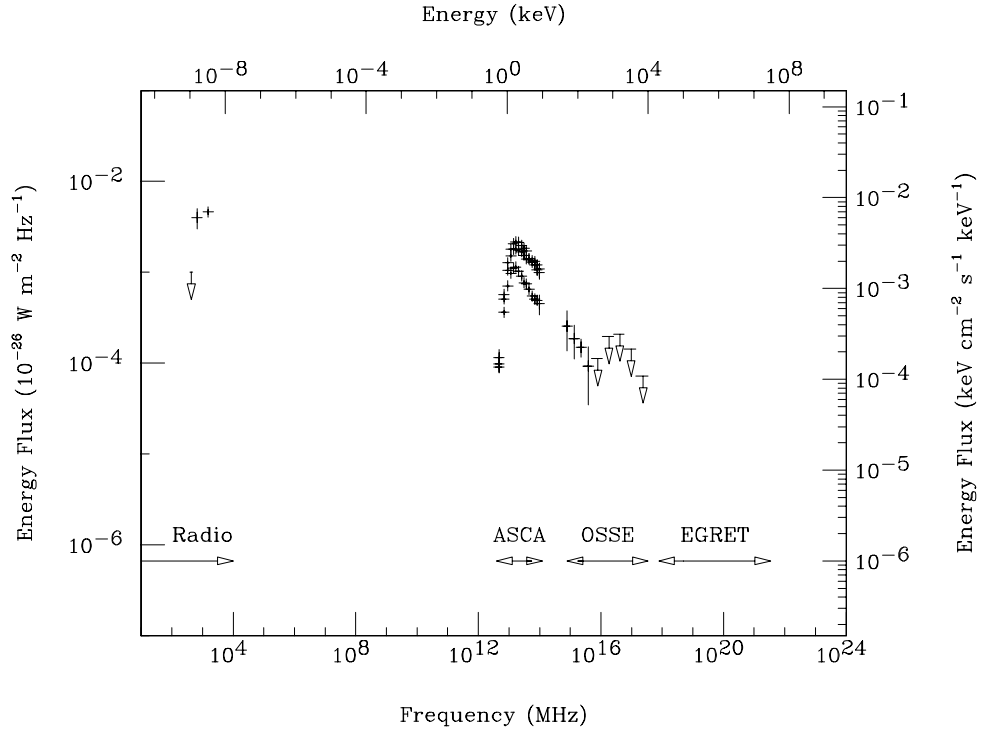


Figure 5.9: Wide band spectrum of the PSR B1259–63/SS 2883 system. The energy flux in the radio band is the pulsed component only. Unpulsed radio emission from the system has not yet been published. Energy bands corresponding to in-orbit detectors are also indicated as bars with the mission name.

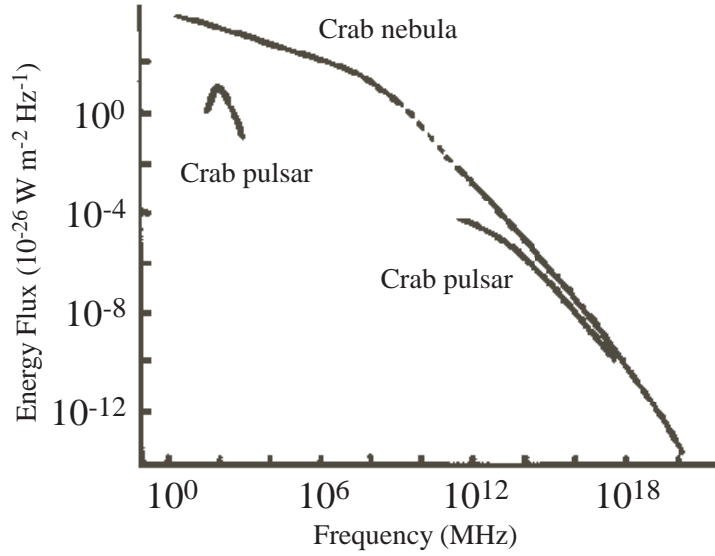


Figure 5.10: Wide band spectrum of the Crab pulsar and the Crab nebula (Makishima 1988).

Here we point out the importance of observations of TeV γ -rays by the air Cerenkov detector. From the lower panel of Figure 5.5 we can see e^\pm pairs with $\gamma \sim 10^6$, which produce the observed X-rays presented in this thesis, may emit inverse Compton γ -rays

with energy of a few TeV. Hence, a detection of TeV γ -rays undoubtedly requires the existence of e^\pm pairs with $\gamma \gtrsim 10^6$ and strongly supports the X-ray emission mechanism proposed in this thesis. Furthermore, the ratio of the TeV γ -ray flux to the X-ray flux is a direct measurement of the ratio of the emission timescales of the inverse Compton process and the synchrotron emission, and hence, the ratio of the photon density and magnetic energy density at the shock region. From the same points of view, the unpulsed radio flux is also important. The radio emission originates the e^\pm pairs whose inverse Compton photons are emitted in the *ASCA* band. Comparison of unpulsed fluxes in radio, X-ray, and TeV γ -ray bands will bring us important information on the shock-powered emission in astrophysical objects.

Chapter 6

Conclusion

We have studied X-ray emission from the binary system PSR B1259–63/SS 2883 with six X-ray observations using the *ASCA* satellite. At all six epochs, the source was observed to have moderate X-ray luminosity $L_X \sim (0.1\text{--}1) \times 10^{34}$ erg s^{−1} in the 1–10 keV band, and absorption $N_H \sim 6 \times 10^{21}$ cm^{−2}, consistent with that expected from the galactic contribution. No X-ray pulsations were detected at any of six observed epochs. The observed X-ray spectra were all consistent with a single power law model. The 1–10 keV luminosity was a factor of ~ 2 smaller at periastron than those at two weeks before and after periastron, while the luminosity when the pulsar was approaching apastron was smaller than that at periastron by one order of magnitude. There was some evidence for a softening of the spectrum at periastron. The absorption, by contrast, was constant for the six observations.

Based on the above observations, we examined possible models of X-ray emission from the system, namely, coronal emission from the Be star, rotation-powered emission from the pulsar, emission from accretion onto the neutron star surface, emission from accreted materials intercepted by the pulsar’s magnetosphere, and shock-powered emission. Among them we found the shock-powered emission model provided a natural way to account for all the observations with *ASCA*. On the other hand, other possible models could not explain all the observational facts, such as moderate X-ray luminosity, no absorption intrinsic to the source, no pulsations, no features in spectrum, no rapid variability in the X-ray luminosity, and radio pulsations visible near the same epochs as the X-ray observations. We therefore concluded that the shock-powered emission dominated the observed X-ray emission from the system.

On the basis of the shock-powered emission model, we concluded the observed X-rays were due to synchrotron emission from e^\pm pairs with $\gamma = 10^6 \sim 10^7$. The power law spectrum with the photon index $\alpha \sim 1.6$, observed when the pulsar was farther than

1000 lt-s from the Be star, required the shock acceleration mechanism to create e^\pm pairs with an energy spectrum $N(\gamma) \propto \gamma^{-2}$ just behind the shock front. Furthermore, from the estimation of radiative cooling timescales, the acceleration must occur within less than ~ 100 s. The apparent softening of the spectral index could be understood in terms of enhanced radiative cooling due to the inverse Compton interaction of e^\pm pairs with UV photons from the Be star. The decrease in X-ray flux near periastron provided additional evidence in favor of this explanation. Alternately, the decrease in the observed flux at apastron approach required the stellar wind distribution to be not spherically symmetric. The large decrease required the momentum flux of the stellar wind to differ between those flowing out in different directions by more than one order of magnitude. This conclusion strongly suggested a large inclination of the pulsar orbit with respect to the equatorial plane of the Be star. In addition, the amount of the decrease constrains the kinetic energy of the pulsar wind as $\dot{E}_{\text{PW}}/\dot{E}_{\text{PW}} \gtrsim 0.49$, and the stellar wind parameters at apastron as $0.05 \lesssim \dot{M}v/(10^{-8} \text{ M}_\odot \text{ yr}^{-1})(1000 \text{ km s}^{-1}) \lesssim 0.28$ for wide ranges of the wind parameters.

The results described in this thesis demonstrate that the study of high-energy emission from pulsar binaries provides a unique chance to investigate the characteristics of the pulsar wind and the stellar wind as well as the shock acceleration mechanism under predictably varying conditions imposed by the Keplerian orbit. Furthermore, our results show that pulsar-driven shock emission is an alternative to accretion for high-energy radiation in binary systems. The possibility that moderate-luminosity non-thermal X-ray binary systems in the Galaxy and in globular clusters might contain energetic radio pulsars powering nebular “calorimeters” has interesting implications.

References

- Arons, J. and Tavani, M.: 1993, *Astrophys. J.* **403**, 249
- Arons, J. and Tavani, M.: 1994, *Astrophys. J., Suppl. Ser.* **90**, 797
- Bell, J. F., Bailes, M., and Bessell, M. S.: 1993, *Nature* **364**, 603
- Bjorkman, J. E. and Cassinelli, J. P.: 1993, *Astrophys. J.* **409**, 429
- Bradt, H. V. D. and McClintock, J. E.: 1983, *Astron. Astrophys. Rev.* **21**, 13
- Buccheri, R., Bennett, K., Bignami, G. F., Caraveo, P. A., Bloemen, J. B. G. M., Hermsen, W., Boriakoff, V., Kanbach, G., Manchester, J. L., and Masnou, J. L.: 1983, *Astron. Astrophys.* **128**, 245
- Cassinelli, J. P., Cohen, D. H., Macfarlane, J. J., Sanders, W. T., and Welsh, B. Y.: 1994, *Astrophys. J.* **421**, 705
- Cominsky, L., Roberts, M., and Johnston, S.: 1994, *Astrophys. J.* **427**, 978
- Cordes, J. M., Romani, R. W., and Lundgren, S. C.: 1993, *Nature* **362**, 133
- Cordova, F. A., Middleditch, J., Hjellming, R. M., and Mason, K. O.: 1989, *Astrophys. J.* **345**, 451
- Cote, J. and Waters, L. B. F. M.: 1987, *Astron. Astrophys.* **176**, 93
- Dougherty, S. M., Waters, L. B. F. M., Burki, G., Cote, J., Cramer, N., Van Kerkwijk, M. H., and Taylor, A. R.: 1994, *Astron. Astrophys.* **290**, 609
- Eichler, D. and Usov, V.: 1993, *Astrophys. J.* **402**, 271
- Gallant, Y. A. and Arons, J.: 1994, *Astrophys. J.* **435**, 230
- Girard, T. and Willson, L. A.: 1987, *Astron. Astrophys.* **183**, 247
- Greiner, J., Tavani, M., and Belloni, T.: 1995, *Astrophys. J., Lett.* **441**, L43

- Grove, J. E., Tavani, M., Purcell, W. R., Johnson, W. N., Kurfess, J. D., Strickman, M. S., and Arons, J.: 1995, *Astrophys. J., Lett.* **447**, L113
- Halpern, J. P. and Ruderman, M.: 1993, *Astrophys. J.* **415**, 286
- Hoshino, M., Arons, J., Gallant, Y. A., and Langdon, A. B.: 1992, *Astrophys. J.* **390**, 454
- Johnston, S., Lyne, A. G., Manchester, R. N., Kniffen, D. A., D'Amico, N., Lim, J., and Ashworth, M.: 1992a, *Mon. Not. R. Astron. Soc.* **255**, 401
- Johnston, S., Manchester, R. N., Lyne, A. G., Bailes, M., Kaspi, V. M., Qiao, G., and D'Amico, N.: 1992b, *Astrophys. J., Lett.* **387**, L37
- Johnston, S., Manchester, R. N., Lyne, A. G., Nicastro, L., and Spyromilo, J.: 1994, *Mon. Not. R. Astron. Soc.* **268**, 430
- Kaspi, V. M., Johnston, S., Bell, J. F., Manchester, R. N., Bailes, M., Bessell, M., Lyne, A. G., and D'Amico, N.: 1994, *Astrophys. J., Lett.* **423**, L43
- Kaspi, V. M., Manchester, R. N., Bailes, M., and Bell, J. F.: 1995a, in J. van Paradijs, E. P. J. van den Heuvel, and E. Kuulkers (eds.), *Compact Stars in Binaries*, Proceedings of the IAU Symposium No. 165, Kluwer Academic Publishers, BV, Holland
- Kaspi, V. M., Tavani, M., Nagase, F., Hirayama, M., Hoshino, M., Aoki, T., Kawai, N., and Arons, J.: 1995b, *Astrophys. J.* **453**, 424+
- Kennel, C. F. and Coroniti, F. V.: 1984a, *Astrophys. J.* **283**, 694
- Kennel, C. F. and Coroniti, F. V.: 1984b, *Astrophys. J.* **283**, 710
- King, A. and Cominsky, L.: 1994, *Astrophys. J.* **435**, 411
- Kochanek, C. S.: 1993, *Astrophys. J.* **406**, 638
- Kulkarni, S. R. and Hester, J. J.: 1988, *Nature* **335**, 801
- Lai, D., Bildsten, L., and Kaspi, V. M.: 1995, *Astrophys. J.* **452**, 819+
- Leahy, D. A., Darbro, W., Elsner, R. F., Weisskopf, M. C., Kahn, S., Sutherland, P. G., and Grindlay, J. E.: 1983, *Astrophys. J.* **266**, 160
- Lucy, L. B.: 1982, *Astrophys. J.* **255**, 286

- Macfarlane, J. J. and Cassinelli, J. P.: 1989, *Astrophys. J.* **347**, 1090
- Makishima, K.: 1988, *Parity* **3(11)**, 2
- Manchester, R. N., Johnston, S., Lyne, A. G., D'Amico, N., Bailes, M., and Nicastro, L.: 1995, *Astrophys. J., Lett.* **445**, L137
- Masai, K.: 1984, *Astrophys. Space. Sci.* **98**, 367
- Melatos, A., Johnston, S., and Melrose, D. B.: 1995, *Mon. Not. R. Astron. Soc.* **275**, 381
- Melrose, D. B.: 1980, *Space Sci. Rev.* **26**, 3
- Melrose, D. B.: 1986, *Instabilities in Space and Laboratory Plasmas*, Cambridge Univ. Press
- Meurs, E. J. A., Pitters, A. J. M., Pols, O. R., Waters, L. B. F. M., Cote, J., Van Kerkwijk, M. H., Van Paradijs, J., Burki, G., Taylor, A. R., and De Martino, D.: 1992, *Astron. Astrophys.* **265**, L41
- Nagase, F.: 1989, *Publ. Astron. Soc. Jpn.* **41**, 1
- Pallavicini, R., Golub, L., Rosner, R., Vaiana, G. S., Ayres, T., and Linsky, J. L.: 1981, *Astrophys. J.* **248**, 279
- Rybicki, G. B. and Lightman, A. P.: 1979, *Radiative Processes in Astrophysics*, John Wiley & Sons, New York
- Sagdeev, R. Z. and Galeev, A. A.: 1969, *Nonlinear Plasma Theory*, Benjamin, New York
- Sekimoto, Y., Hirayama, M., Kamae, T., and Kawai, N.: 1995, *Astrophys. J.* **443**, 271
- Serlemitsos, P. J., Jalota, L., Soong, Y., Kunieda, H., Tawara, Y., Tsusaka, Y., Suzuki, H., Sakima, Y., Yamazaki, T., and Yoshioka, H.: 1995, *Publ. Astron. Soc. Jpn.* **47**, 105
- Seward, F. D. and Harnden, F. R., J.: 1982, *Astrophys. J., Lett.* **256**, L45
- Seward, F. D., Harnden, F. R., J., and Helfand, D. J.: 1984, *Astrophys. J., Lett.* **287**, L19
- Shapiro, S. L. and Teukolsky, S. A.: 1983, *Black Holes, White Dwarfs and Neutron Stars. The Physics of Compact Objects*, Wiley-Interscience, New York
- Shibata, S.: 1991, *Astrophys. J.* **378**, 239

- Skinner, G. K., Bedford, D. K., Elsner, R. F., Leahy, D., Weisskopf, M. C., and Grindlay, J.: 1982, *Nature* **297**, 568
- Snow, T. P., J.: 1982, *Astrophys. J., Lett.* **253**, L39
- Tanaka, Y., Inoue, H., and Holt, S. S.: 1994, *Publ. Astron. Soc. Jpn.* **46**, L37
- Tavani, M., Arons, J., and Kaspi, V. M.: 1994, *Astrophys. J., Lett.* **433**, L37
- Taylor, A. R., Dougherty, S. M., Waters, L. B. F. M., and Bjorkman, K. S.: 1990, *Astron. Astrophys.* **231**, 453
- Taylor, J. H. and Cordes, J. M.: 1993, *Astrophys. J.* **411**, 674
- Waters, L. B. F., Marlborough, J. M., Van Der Veen, W. E. C., Taylor, A. R., and Dougherty, S. M.: 1991, *Astron. Astrophys.* **244**, 120
- Waters, L. B. F. M.: 1986, *Astron. Astrophys.* **162**, 121
- Waters, L. B. F. M., Van Den Heuvel, E. P. J., Taylor, A. R., Habets, G. M. H. J., and Persi, P.: 1988, *Astron. Astrophys.* **198**, 200
- White, N. E., Swank, J. H., and Holt, S. S.: 1983, *Astrophys. J.* **270**, 711

Acknowledgment

The *ASCA* observatory was developed, launched, and operated successfully with great efforts by *ASCA* team members, including people at the Institute of Space and Astronautical Science (ISAS), the University of Tokyo, Tokyo Metropolitan University, the Institute of Physical and Chemical Research (Riken), Nagoya University, Osaka University, Kyoto University, Iwate University, and Miyazaki University. I am indebted to the staff of the *ASCA* Guest Observers Facility. This work was supported by fellowships of the Japan Society for the Promotion of Science for Japanese Junior Scientists.

I would like to thank Prof. T. Kamae and Dr. T. Takahashi for their guidance and advice throughout the five years as a doctoral candidate. I also thank Prof. F. Nagase, Dr. M. Tavani, Prof. N. Shibasaki, Prof. M. Hoshino, and Prof. K. Mitsuda for their contributions to discussions in this thesis. Their comments and discussions were always helpful and useful for me. I am grateful to Dr. V. M. Kaspi for a lot of helpful advice on English as well as useful comments on the discussions. I could not have finished the thesis without her help. I thank Dr. N. Kawai, Dr. T. Aoki, Dr. L. Cominsky, and Dr. J. Arons for their collaboration on the *ASCA* observations of the PSR B1259–63/SS 2883 system.

I am very much obliged to Prof. H. Inoue, Prof. Y. Tanaka, Prof. Y. Ogawara, Prof. F. Makino, Prof. T. Murakami, Prof. M. Itoh, Dr. T. Kii, Dr. T. Dotani, Dr. M. Ishida, and Mr. R. Fujimoto for inviting me as an *ASCA* team member at ISAS. Also, I wish to thank Ms. T. Morooka, Ms. C. Tohyama, Ms. H. Takeda, Ms. Y. Sasaki, Ms. M. Kondo, Ms. F. Iwata, Ms. I. Yamagishi, Ms. Y. Kawakami, Ms. K. Kohno, and Ms. A. Toyama for their great help on a lot of office routines in my university life. In addition, I am obliged to warm-hearted people at Kagoshima Space Center (KSC), where I spent for many weeks as a duty scientist, for their hospitality.

I thank Mr. M. Tanaka, Dr. A. Shirahashi, Dr. T. Takeda, Dr. S. Gunji, Dr. S. Miyazaki, Dr. T. Tamura, Dr. Y. Sekimoto, Ms. N. Y. Yamasaki, Mr. Y. Fukazawa, Mr. A. Nakao, Mr. K. Suzuki, Mr. H. Kubo, Mr. Y. Saito, Mr. H. Ezawa, Mr. K. Matsuzaki, Mr. N. Tsuchida, Mr. T. Ohtsuka, Mr. S. Nakamae, and Mr. K. Nagata for their great

support and useful suggestions. I was very glad to spend a lot of happy time at ISAS with Dr. T. Takeshima, Dr. K. Tamura, Dr. K. Yoshida, Dr. C. Otani, Dr. K. Asai, Mr. H. Honda, Dr. H. Negoro, Dr. Ogasaka, Dr. Y. Ueda, Mr. T. Kotani, Mr. S. Uno, Mr. T. Sonobe, Mr. Y. Takizawa, Ms. A. Yamashita, Ms. K. Okada, Mr. M. Sugizaki, Mr. K. Sasaki, Mr. Y. Segawa, Mr. J. Kataoka, Mr. H. Ozawa, Mr. R. Shibata, Mr. Y. Goto, Ms. K. Miya, Mr. H. Ezuka, and Ms. K. Takizawa. At Hongo Campus my research life was also helped by Dr. M. Tashiro, Dr. Y. Kohmura, Dr. Y. Ikebe, Dr. Y. Ishisaki, Mr. H. Kaneda, Ms. K. Matsushita, Mr. T. Tamura, Ms. N. Iyomoto, Ms. E. Idesawa, Mr. T. Mizuno, and Mr. H. Obayashi. Without these cheerful people, my daily life would have been boring.

Finally I thank my family for keeping a comfortable home for me to be relaxed and for supporting my graduate school life.